Light-Induced Microfluidic Transport Phenomena

TECHNISCHE
UNIVERSITÄT
DARMSTADT

FACHBEREICH
MASCHINENBAU

Center of
Smart Interfaces

Nano- and
Microfluidics

Vom Fachbereich Maschinenbau
an der Technischen Universität Darmstadt
zur Erlangung des akademischen Grades eines
Doktors der Naturwissenschaften (Dr. rer. nat.)
Genehmigte
Dissertation
vorgelegt von
MSc. Phys. Subramanyan Namboodiri Varanakkottu
geboren in Mandur, Indien

Berichterstatter : Prof. Dr. rer. nat. Steffen Hardt
(Technische Universität Darmstadt)

Mitberichterstatter : Prof. Dr. rer. nat. Andreas Dreizler
(Technische Universität Darmstadt)

Tag der Einreichung : 31.01.2013
Tag der mündlichen Prüfung: 28.05.2013

Darmstadt 2013
D17

Erklärung

Hiermit erkläre ich, dass ich die vorliegende Arbeit, abgesehen von den in ihr ausdrücklich genannten Hilfen, selbständig verfasst habe.

Darmstadt, 03-07-2013 Subramanyan Namboodiri Varanakkottu

To my family…

Contents

Acknowledgments

First I would like to express sincere gratitude to my supervising guide **Prof. Dr. Steffen Hardt** for steering me through the journey and for his valuable suggestions, ideas and discussions during my research. **Prof. Dr. Andreas Dreizler** is gratefully acknowledged for accepting to examine my Ph.D. dissertation. I thank **Prof. Dr. Markus Biesalsky**, **Mr. Helge Schenderlein** and **Mrs. Martina Ewald** for providing the chemicals and polymers used in this work.

I am very much grateful to **Dr. Sajan D George** for his support, discussions and motivational thoughts. His suggestions and criticism helped me improve in many ways. I would like to thank **Dr. Tobias Baier** and **Dr. Mathias Dietzel** for helping me with the fundamentals of fluid mechanics. I can never forget the discussions with **Dr. Wenjia Xiao**, **Dr. Ashok Sinha**, **Dr. Thomas Hahn** and **Dr. Natalya Pertaya Braun**. I thank **Mr. Aaron Dörr**, **Mr. Alexander Eifert**, **Mrs. Gabriele Goet**, **Mr. Ramin Hajian**, **Mr. Iman Nejati**, **Mrs. Clarissa Schönecke**, **Mr. Miklós Vécsei** and **Mr. Jörg Bültemann** for their co-operation, whole hearted support and creating a motivating environment. I express my gratitude to **Mrs. Angela Berger** and **Mrs. Marion Müller** for their help and co-operation. I am very much thankful to **Mr. Jose Pinson** for helping me in setting up experiments and LabVIEW programming. I thank **Mr. Dieter Meier** and **Mr. Axel Rodenhäuser** for their technical assistance.

I thank **Dr. Ditty Dixon**, **Mr. Deepu J Babu**, **Mr. Febin Kurian**, **Dr. Aiswarya**, **Mrs. Gisa**, **Mrs. Merin**, **Mrs. Linsy**, **Mrs. Tina**, **Mr. Jean**, **Mr. Jagan**, **Dr. Nitin**, **Mr. Ramdayal**, **Mr. Martin Still** and **Mr. Upendra** for their support and friendship.

I thank my CUSAT friends **Dr. Sreekumar. S**, **Dr. Sajeesh T. H**, **Dr. Vimal Kumar**, **Dr. Manu P John**, **Mr. Sreeroop**, **Mr. Subin Thomas**, **Mr. Rajesh C.S**, **Dr. Anita Warrier**, **Dr. Pramitha. V** and **Mr. Krishnaprasad P. S** for their whole hearted support and friendship. I am thankful to **Prof. Dr. Vijayakumar K. P** and **Prof. Sudha Kartha C** for motivating me. I remember all my teachers and all my friends for their constant support.

The prayers and encouragement of my parents and family has enabled me to overcome the difficulties encountered during the course. I cherish the time with my

brothers **Vishnu** and **Harikrishnan**, that being great treasure in my life. Its a great blessing to get such a loving and charming wife, **Sreya**.

Last and the most... my all goes to the almighty...

Darmstadt, 03-07-2013 Subramanyan Namboodiri Varanakkottu

Abstract

Optofluidics is an emerging field which combines microfluidics and optics, having widespread applications in fundamental sciences as well as engineering. Among the research in the areas of optofluidics, manipulation of small objects such as particles and droplets is of great interest. Precise control over the manipulation and confinement of such objects is a challenging task. Unification of microfluidics and optics opens a new way to achieve this goal with added advantages such as non-contact manipulation capability and tunability. This Ph.D. dissertation addresses optofluidic manipulation of particles and droplets based on some novel concepts.

The section on light-induced particle manipulation begins with optical trapping inside a microfluidic channel. Motivation of this study is to understand the influence of velocity profile on the trapped particle. An optical trapping experimental setup is constructed using a He-Cd laser (442 nm emission) as the trapping source. Optical trapping experiments are performed under two flow conditions. A particle trapped inside a microfluidic channel experiences a parabolic velocity profile. In the second method, particles are trapped inside a sample chamber where the trapped particle experiences a uniform velocity profile. Experiments are performed at different optical powers with particles having various diameters. Results showed that for particles having intermediate size the trapping force is higher in the case of particles trapped inside the microfluidic channel than that of a sample chamber. This is attributed to the contribution of Saffman lift force arising from the parabolic velocity gradient. Experimentally measured optical trapping stiffness is found to be in good agreement with the theoretical model.

Following that, a novel particle manipulation technique is presented. Here, microparticle adsorbed at the air-water interface is trapped and manipulated along the interface. The method relies on photoresponsive surfactants adsorbed to a gas-liquid interface that can be reversibly switched between two isomeric states (a *trans* state and a *cis* state) using light beams. The principle is based on local changes of the surface tension, giving rise to Marangoni stresses. Depending on the type of surfactant isomer in the region around the laser spot, a flow either radially inward or outward is created. For the trapping of microparticles, a 325 nm beam from a He-Cd laser is

focused at the interface, which results in an inward flow directing towards the focal spot. This inward flow is utilized for trapping and manipulation of particles. Interfacial flow velocity is characterized using particle streak velocimetry. It is experimentally demonstrated that this trapping mechanism is capable of manipulating the trapped particle at lower intensity than conventional optical tweezers.

Finally, studies on light-induced droplet manipulation were conducted, utilizing the phase transition of temperature sensitive PNIPAM (Poly(N-isopropylacrylamide)) polymer films. PNIPAM films are prepared on UV absorbing glass plates. Absorption of the UV light by the glass raises its temperature resulting in the phase transition of PNIPAM film from a swollen (hydrophilic) to a deswollen (hydrophobic) phase. Experiments show that PNIPAM films undergo a phase transition from a hydrophilic to a hydrophobic state at around $26^o C$. At the hydrophobic state, water drop placed on the substrate exhibits a contact angle of about 78^o while it reduces to 53^o at the hydrophilic state. Experiments are performed to drive the water drop by creating a wettability gradient over the surface by locally cooling one side of the drop. Though the drop spreads towards the colder region, due to the large hysteresis in contact angle, the receding edge of the drop is pinned at the surface.

Zusammenfassung

Die Optofluidik ist ein aufstrebendes Forschungsgebiet, welches die Mikrofluidik mit der Optik vereint. Als solches weist sie einen weiten Einflussbereich sowohl in der Grundlagenforschung wie auch im Ingenieurwesen auf. Von großem Interesse in der optofluidischen Forschung ist die Manipulation von kleinen Objekten wie Partikeln oder Tröpfchen. Die präzise Lokalisierung und kontrollierte Bewegung solcher Objekte erweist sich als eine anspruchsvolle Aufgabe. Die Vereinigung von Mikrofluidik und Optik eröffnet dabei einen neuen Weg, dieses Ziel zu erreichen und bietet dabei zusätzliche Vorteile wie berührungslose Manipulation und genaue Abstimmbarkeit. Diese Dissertation befasst sich mit der optofluidischen Manipulation von Partikeln und Tröpfchen mittels verschiedener neuer Konzepte.

Der Abschnitt über lichtinduzierte Partikelmanipulation beginnt mit optischen Pinzetten in einem mikrofluidischen Kanal. Die Motivation dieser Studie ist es, den Einfluss des Geschwindigkeitsprofils auf das eingefangene Partikel zu verstehen. Ein Versuchsaufbau mit optischer Falle wird unter Verwendung eines He-Cd-Lasers (Emission bei 442 nm) als Lichtquelle aufgebaut. Experimente zur optischen Falle werden unter zwei Strömungsbedingungen durchgeführt. Im ersten wird ein eingefangenes Teilchen in einem durchströmten mikrofluidischen Kanal einem parabolischen Geschwindigkeitsprofil ausgesetzt. Im zweiten Aufbau werden Partikel innerhalb einer Probenkammer gefangen, so dass bei Bewegung der Kammer relativ zur optischen Falle ein gleichmäßiges Geschwindigkeitsprofil auf das Teilchen wirkt. Es wurden Versuche mit verschiedenen optischen Leistungen sowie mit Teilchen unterschiedlichen Durchmessers durchgeführt. Die Ergebnisse zeigen, dass für Teilchen mittlerer Größe die Fallenkraft innerhalb des mikrofluidischen Kanals höher ist als im Fall von Teilchen, die einer Probenkammer gefangen sind. Dies kann auf den Beitrag der Saffmanschen Auftriebskraft aufgrund des Geschwindigkeitsgradienten im parabolischen Profil zurückgeführt werden. Experimentell gemessene Steifigkeiten der optischen Falle zeigen eine gute Übereinstimmung mit dem theoretischen Modell.

Darauf folgend präsentieren wir eine neuartige Methode der Partikelmanipulation. Hierbei wird das an der Luft-Wasser-Grenzfläche adsorbierte Mikropartikel eingefangen und entlang der Grenzfläche bewegt. Die Methode beruht auf an der Gas-

Flüssigkeits-Grenzfläche adsorbierten lichtempfindlichen Tensiden, die mittels Licht reversibel zwischen zwei isomeren Zuständen (einem trans- und einem cis-Zustand) hin und her geschaltet werden können. Das Prinzip basiert auf der lokalen Änderungen der Oberflächenspannung, welches zu Marangoni-Spannungen führt. Abhängig von der Art des Isomers in der Nähe des Laserspots wird eine Strömung entweder radial nach innen oder nach außen erzeugt. Zum Festhalten von Mikropartikeln wird der Strahl eines 325 nm He-Cd-Lasers auf die Grenzfläche fokussiert, was zu einer in Richtung Brennpunkt gerichteten Strömung führt. Diese nach innen gerichtete Strömung wird zum Einfangen und Bewegen von Partikeln verwendet. Die Strömungsgeschwindigkeit an der Grenzfläche wird mittels Particle-Streak-Velocimetry bestimmt. Es wird experimentell gezeigt, dass dieser Fallenmechanismus eine Manipulation der gefangenen Teilchen bei geringerer Intensität ermöglicht als bei einer herkömmlichen optischen Pinzette.

Schließlich wurden Studien zur lichtinduzierten Manipulation von Tröpfchen auf mit temperaturempfindlichem PNIPAM (Poly (N-isopropylacrylamid)) beschichteten Oberflächen durchgeführt. Dabei wurde eine Schicht PNIPAM auf UV-absorbierenden Glasplatten abgeschieden. Die Absorption von UV-Licht im Glas erhöht dessen Temperatur, was zum Phasenübergang des PNIPAM Films von einer gequollenen (hydrophilen) zu einer kontrahierten (hydrophoben) Phase führt. Experimente zeigen, dass bei PNIPAM-Filmen der Phasenübergang vom hydrophilen zum hydrophoben Zustand bei etwa 26°C erfolgt. Im hydrophoben Zustand weist ein auf dem Substrat platzierter Wassertropfen einen Kontaktwinkel von etwa 78° auf, während dieser sich im hydrophilen Zustand auf 53° reduziert. Es wurde experimentell versucht, einen Wassertropfen dadurch anzutreiben, dass mittels lokaler Kühlung einer Seite des Tropfens ein Benetzbarkeitsgradient induziert wird. Obwohl der Tropfen sich in Richtung des kälteren Bereichs ausdehnt, bleibt er doch aufgrund der großen Kontaktwinkel-Hysterese an der zurückweichenden Kante des Tropfens an der Oberfläche haften.

Symbols and Abbreviations

Symbol		**SI Unit**
F_s	Scattering force	[N]
F_g	Gradient force	[N]
λ	Wavelength of light	[m]
I_o	Incident laser intensity	[W/m^2]
R	Particle radius	[m]
c	Velocity of light in vacuum	[m/s^2]
n_m	Refractive index of the medium	[-]
n_p	Refractive index of the particle	[-]
m	Ratio of refractive index between the particle and the medium	[-]
E	Electric field	[V/m]
$I(s)$	Intensity at a depth s	[W/m^2]
F_{DEP}	Dielectrophoretic force	[N]
K^*	Clausius-Mossotti factor	[-]
E_{rms}	Root mean square value of the electric field	[V/m]
ϵ_p	Permittivity of the particle	[F/m]
ϵ_m	Permittivity of the medium	[F/m]
σ_m	Conductivity of the medium	[S/m]
σ_p	Conductivity of the particle	[S/m]
ω	Frequency of the electric field	[Hz]
V_A	Applied voltage	[V]
θ_0	Initial contact angle of the liquid drop	[radian]
$\theta(V_A)$	Contact angle of the liquid drop at the applied voltage	[radian]
σ_{LV}	Liquid-vapor interfacial tension	[N/m]
d_l	Thickness of the film	[m]
F_c	Capillary force	[N]

θ_a	Contact angle of the drop at the advancing edge	[radian]
θ_r	Contact angle of the drop at the receding edge	[radian]
L_d	Base diameter of the drop	[m]
P_{Photon}	Momentum of the photon	[N.s]
h	Plank constant	[J.s]
E_{Photon}	Energy of the photon	[J]
F_p	Restoring force	[N]
Q_t	Trapping efficiency	[-]
P	Laser power	[W]
θ_i	Angle of incidence	[radian]
θ_r	Angle of refraction	[radian]
$R_{Fresnel}$	Fresnel coefficient for reflection	[-]
$T_{Fresnel}$	Fresnel coefficient for transmission	[-]
W	Interaction energy	[J]
$\boldsymbol{\mu}$	Dipole moment	[C.m]
V_p	Particle volume	[m^3]
α	Polarizability of the particle	[C.m^2/V]
u_x	Fluid velocity along x axis	[m/s^2]
Δp	Pressure drop across the microchannel	[N/m^2]
L	Length of the channel	[m]
μ	Fluid viscosity	[N.s/m^2]
A	Cross sectional area of the channel	[m^2]
Q	Flow rate	[m^3/s]
I_p^*	Specific polar moment of inertia	[m^2]
I_p	Polar moment of inertia	[m^4]
R_e	Reynolds number	[-]
d	Depth of the channel	[m]
w	Width of the channel	[m]
V	Average velocity	[m/s]
D_h	Hydrolic diameter of the channel	[m]
F_h	Hydrodynamic drag force	[N]

v_p	Velocity of the particle	[m/s]
a_{trap}	Displacement of the particle from the trap center	[m]
k	Trap stiffness	[N/m]
$F_{saffman}$	Saffman lift force	[N]
F_{axial}	Axial trapping force	[N]
g	Acceleration due to gravity	[m/s^2]
ρ_p	Density of the particle	[kg/m^3]
ρ_m	Density of the medium	[kg/m^3]
K_b	Boltzmann constant	[J/K]
T	Temperature	[K]
$F_{lateral}$	Lateral trapping force	[N]
k_x	Trap stiffness along x direction	[N/m]
x_{trap}	Particle displacement along x direction	[m]
F_{escape}	Escape force	[N]
d_{beam}	Beam diameter	[m]
M^2	M^2 number	[-]
θ_d	Full angle divergence of the beam	[radian]
$I(r,z)$	Intensity at the position *(r,z)*	[W/m^2]
ω_A	Radius of the Airy's spot	[m]
ϵ	Eccentricity of the focal volume	[-]
n_g	Refractive index of the glass	[-]
θ_{cr}	Critical angle	[radian]
l'	Trapping depth	[m]
Δz	Axial focal shift	[m]
$U(x)$	Potential energy	[J]
k_r	Transverse trapping stiffness	[N/m]
Q_a	Axial trapping efficiency	[-]
u	Fluid velocity	[m/s]
ρ	Density of the liquid	[kg/m^3]
p	Pressure	[N/m^2]

$\overleftrightarrow{T}_l$	Stress tensor	[Pa]
$\overleftrightarrow{E}$	Deviatoric stress tensor	[Pa]
∇_s	Surface gradient operator	[-]
Γ	Surface excess concentration	[mol/m^2]
γ_T	Thermal expansion coefficient	[N/m.K]
γ_Γ	Solutal expansion coefficient	[1/mol%]
Ma_Γ	Solutal Marangoni number	[-]
D_s	Molecular diffusivity	[m^2/s]
μ_i	Chemical potential of the surfactant molecule	[J]
Γ_{trans}	Surface excess concentration of the *trans* molecule	[mol/m^2]
Γ_{cis}	Surface excess concentration of the *cis* molecule	[mol/m^2]
ϵ_{trans}	Molar extinction coefficient of the *trans* molecule	[m^2/mol]
ϵ_{cis}	Molar extinction coefficient of the *cis* molecule	[m^2/mol]
ϕ_{tran}	Quantum efficiency for *trans-cis* conversion	[-]
ϕ_{cis}	Quantum efficiency for *cis-trans* conversion	[-]
$\Gamma(t)$	Dimensionless concentration	[-]
c_{sub}	Surfactant concentration in the sub phase	[mol]
k_{ads}^{trans}	Adsorption constant for the *trans* molecule	[m^3/mol]
k_{des}^{trans}	Desorption constant for the *trans* molecule	[m^3/mol]
k_{ads}^{cis}	Adsorption constant for the *cis* molecule	[m^3/mol]
k_{des}^{cis}	Desorption constant for the *cis* molecule	[m^3/mol]
ω_{trans}	Surface area per molecule for the *trans* molecule	[m^2]
ω_{cis}	Surface area per molecule for the *cis* molecule	[m^2]
d_{spot}	Spot size at the laser focus	[m]
f_{lens}	Focal length of the plano-convex lens	[m]
T_λ	Transmittance at a wavelength λ	[-]
P_T	Transmitted power	[W]
P_I	Incident power	[W]
t_i	Time constant	[s]
σ_{LV}	Liquid-Vapor surface tension	[N/m]

σ_{SV}	Solid-Vapor surface tension	[N/m]
σ_{SL}	Solid-Liquid surface tension	[N/m]
θ_Y	Equilibrium contact angle	[radian]
θ_A	Advancing contact angle	[radian]
θ_R	Receding contact angle	[radian]
$\Delta\theta$	Hysteresis contact angle	[radian]
$\Delta\theta_{drop}$	Difference in contact angle of the either side of the drop	[radian]
C_p	Specific heat capacity of glass	[J/Kg.K]
α_{abs}	Absorbance of the glass plate	[-]
ϕ	Schwarzschild coefficient	[-]

Abbreviations

NA	Numerical Aperture
OT	Optical Tweezers
IR	Infra Red
TIR	Total Internal Reflection
DEP	Dielectrophoresis
OET	Optoelectronic Tweezer
DNA	Deoxyribonucleic acid
UV	Ultraviolet
3D	Three Dimensional
2D	Two Dimensional
GLMT	Generalized Lorentz-Mie theory
CMC	Critical Micellar Concentration
$C_4AzoOC_4E_2$	Diethyleneglycol mono(4’,4-butyloxy,butyl-azobenzene)
LDV	Laser Doppler Velocimetry
PSV	Particle Streak Velocimetry
PIV	Particle Image Velocimetry
LCST	Lower critical solution temperature
NIPAM	N-isopropylacrylamide
AIBN	Azoisobutyronitrile
MABP	Methacryloxybenzophenone
PNIPAM	Poly(N-isopropylacrylamide)

1 Introduction

1.1 Motivation

Control over matter using light is a fascinating subject. Light is a powerful tool for the manipulation of micro and nanoscale objects. Since the invention of lasers, the branch of Photonics is growing fast for the last five decades. The unique properties of lasers such as monochromaticity, directionality and coherence have been utilized in almost all the fields of science and technology ranging from medical applications to fiber optic communications. Over the last 40 years, there has been considerable interest in optical manipulation of individual particles, which enables the study of biological motors to the interaction between colloidal particles [1]. Though several methods have been proposed for the manipulation of small objects, most of them require either complex experimental setup or very high electrical or optical gradient. To mention a few, optical tweezers, a commonly employed particle manipulation technique have some fundamental limitations such as diffraction limited optics and the gradient nature of the trapping force [2]. The gradient force scales to the third power of the diameter of the particle, as a result, the trapping force rapidly diminishes with decreasing particle diameter. On the other hand, dielectrophoresis, an electrical analogy of optical tweezers also rely on gradient forces, which imposes a restriction on manipulation of nanoscale objects [3]. To overcome these restrictions, near-field and combination of optical forces with other manipulation techniques have been proposed [4, 5]. An important development in this area is optoelectronic tweezers, which is a combination of optics and dielectrophoresis [5]. Though they succeed the requirement of high optical power for particle manipulation, complex experimental designing or optical patterning is required for achieving the particle or droplet manipulation.

Another emerging field is optofluidics, where properties of optics and microfluidics are combined. Both microfluidics and optics have emerged as two key fields for the transportation and control over small objects such as particles or liquid droplets. Their combination offers unique advantages such as non-contact manipulation capability and tunability which finds a wide range of applications such as tunable optical elements, optofluidic sensors, optofluidic lasers and particle transport [6, 7]. Such an integrated approach is implemented for the trapping and transport of particles and droplets inside the microfluidic channel or on an open surface. An important development in this field, which utilizes light-induced microfluidic flow for the transport of nanoparticles is light-actuated electro-osmosis [8]. The hydrodynamic force scales with the diameter of the particle, instead of the volume of the particle as in the case of gradient forces. This property can be advantageous while handling nanoparticles. Recently, some interesting works based on light-induced wettability gradient have been reported for the precise manipulation of droplets [9]. These methods are capable of remote manipulation of droplets on photosensitive surfaces. Most recently, manipulation of oil drops on light-sensitive surfaces based on light-induced hydrodynamic flow have been proposed [10]. These methods overcome the requirement of high intensity and complex experimental designing imposed by conventional methods. In this context, new steps towards precise control over small objects are appreciable. This thesis presents the research on optofluidic manipulation of small particles and droplets. The experiments on optical trapping examines the influence of flow velocity profile and lower trapping wavelength on the trapped particle. Following that, a novel method for the trapping and precise manipulation of microparticles based on light-induced hydrodynamic flow is presented. This method offers several advantages such as low power requirement, simple optical setup, parallel manipulation capability, tunability (wavelength and intensity) and more favorable force law over conventional optical techniques. This thesis also examines optofluidic transport of water droplets over temperature-sensitive polymer film, where the temperature of the film is remotely controlled by the absorption of light. The motivation behind this method is to create a smart surface which can transport small water drops with more flexibility than the existing techniques.

1.2 Objective of the thesis

The purpose of this Ph.D. research is to use light for the trapping and manipulation of particles and droplets in microfluidic environment. This thesis can be broadly divided in two main parts:

1. Studies on light-induced particle manipulation
2. Studies on light-induced droplet manipulation

1. Studies on light-induced particle manipulation

Light-induced particle manipulation is achieved via two mechanisms:

i. Particle trapping using optical tweezers

Optical tweezers rely on momentum transfer between the light photons and the dielectric particle [2]. Optical tweezers are widely implemented in microfluidic environment [11, 12]. The section on optical trapping examines the optical trapping of microparticles inside a microfluidic channel. An optical tweezer setup is constructed using a He-Cd laser (442 nm emission). A detailed investigation has been carried out to understand the effect of the parabolic flow profile and the particle size on the trapping parameters such as trapping force and trapping stiffness. The results are compared with that obtained from trapping inside a sample chamber where the trapped particle experiences a uniform velocity profile. The comparison shows that lift force arising from the parabolic flow profile inside a microfluidic channel have significant influence on the trapping force and the maximum displacement of the particle inside the trap. It is shown that a value close to the theoretically predicted displacement has been achieved by trapping inside microfluidic channel with appropriate choice of the trapping wavelength.

ii. Particle trapping using light-induced Marangoni tweezers

Here, the particle trapping is achieved by the light-induced Marangoni flow. A photoswitchable interface is created using photosurfactant incorporated with azobenzene molecule. The molecule has two distinct isomeric states, a *trans* and a *cis* state. Light of 325 nm switches the molecule from the *trans* state to the *cis* state and the light of 442 nm does the reverse. When adsorbed at the interfaces, the *cis* rich surface exhibits relatively higher surface tension than that of the *trans* rich surface. Light of 325 nm focused at the interface to increase the surface tension locally, resulted in a Marangoni flow towards the laser spot. This inward Marangoni flow generated by the gradient in surface tension is utilized to trap polystyrene particles adsorbed at the interface. Furthermore, the position of the trapped particle can be manipulated along the interface by moving the laser spot. Additionally, the direction of the flow can be reversed by switching the laser beam to 442 nm. A detailed experimental analysis has been done to understand the factors influencing the flow field such as laser exposure time, incident intensity and surfactant concentration. The results show that the adsorbed particles can be manipulated with about 10^3 times less light intensity than conventional optical tweezers. Also, this method does not require any complex optical setup or high numerical aperture objective lens. Additionally, the linear dependence of the hydrodynamic force can be a powerful tool for the manipulation of the nanoparticles.

2. Studies on light-induced droplet manipulation

Open surface digital microfluidics is an emerging field with potential applications in medicine and biological analysis. Several methods such as electrowetting [13], thermocapillarity [14], dielectrophoresis [3], magnetic force [15] and thermo-chemical effect [16] have been demonstrated to achieve this goal. Another promising way to achieve droplet manipulation is by the use of environmental sensitive materials. Capability of light-induced droplet motion using photosensitive materials have already been demonstrated [9, 10]. Another possibility is to use temperature sensitive materials to achieve this goal. Poly(N-isopropylacrylamide) (PNIPAM) is a widely used temperature sensitive material. PNIPAM exhibits a Lower Critical Solution Temperature (LCST) in water. PNIPAM is in swollen state (hydrophilic) below LCST and deswollen state (hydrophobic) above LCST. Recently, light-induced wettability change has been demonstrated on PNIPAM film prepared on surface coated with nanoaprticles [17]. This thesis demonstrates a simpler technique, where PNIPAM is spin coated on a UV absorbing glass substrate. Absorption of UV photons controls the temperature of the film, thus the wettability. PNIPAM films exhibit a phase transition at a temperature of about 26 ^{o}C. The contact angle difference of more than 25^{o} is observed. To drive the droplet over the surface, experiments are performed by locally cooling one edge of the droplet, but high hysteresis contact angle made the receding edge of the drop pin at the three phase line and not allowing the drop to move.

1.3 Organization of the thesis

This thesis is devoted to the studies on light-induced particle and droplet manipulation. *Chapter 2* provides the basics and recent advances in light-induced manipulation techniques. This chapter describes both the conventional optical techniques and the light-induced wettability gradient or interfacial flow that is utilized for the manipulation of small particles and droplets. *Chapter 3* and *Chapter 4* report the studies on optical trapping where the effect of flow profile on the trapped particle is discussed. *Chapter 5* provides the fundamentals of the interfacial transport phenomena with an emphasis on solutal Marangoni effect. Later part of this chapter discusses the properties of the photoswitchable surfactants used in this work. In *chapter 6*, a novel particle trapping mechanism based on light-induced Marangoni flow is presented. The principle relies on the photoswitching of photosurfactants adsorbed to the air-water interface. Inward flow generated at the interface is utilized to trap and manipulate micrometer sized polymer particle adsorbed to the interface. *Chapter 7* describes the light-induced wettability modification of temperature sensitive polymer thin films. Polymer film is coated on a light absorbing substrate. Light-induced wettability change and the experiments performed to move the droplet along the polymer surface are presented in this chapter. The thesis ends with *chapter 8*, where the main outcome of the study with future directions is outlined.

2 Light-induced particle and droplet manipulation techniques

2.1 Introduction

The ability to trap and transport particles, atoms, biological cells and droplets have widespread applications in fundamental science and technology. Manipulation of such objects can be actualized by a variety of methods based on optical, electric, magnetic, acoustic and hydrodynamic forces. Among such methods, optical methods have certain unparalleled advantages such as non-contact manipulation, high spatial and temporal resolution and tunability (wavelength and power). Light-induced manipulation methods involve the use of light to induce forces on particles or fluids either by momentum or energy energy transfer. Optically-induced manipulation methods can be split into two categories: direct and indirect methods. Direct methods such as optical tweezers directly interact with the matter of interest and indirect methods rely on the modification of material property by the energy transfer. Such methods involve the manipulation of small objects by modifying interfacial tension, surface energy or photoconductivity using light energy.

This chapter provides a brief review on the current methods and recent advances in the field of light-induced particle and droplet manipulation. This chapter begins with the conventional optical tweezers and extends to recent advances in near-field optical techniques. The possibility of light to combine with other prominent manipulation methods like dielectrophoresis and electro-osmosis is also discussed. The final section focuses on microfluidic actuation based on the light-induced surface energy modification.

2.2 Light-induced particle manipulation techniques

Interaction between light and matter is a fundamental process. Influence of light on the matter was first predicted by astronomer Johannes Kepler in seventeenth century while he studied the tails of comets. Radiation pressure from the sun is the reason behind the tails of comet when they pass near the sun. In 1876, James Clerk Maxwell theoretically predicted that light waves are associated with linear momentum. Optical micro-manipulation requires extremely high intensity gradients that are only possible with focused laser beam. In 1970, Arthur Ashkin of Bell Labs demonstrated that the microparticles can be propelled with a moderately focused light beam [18]. This method was further extended to trap particles known as optical levitation traps. In the case of optical levitation trap, gravitational force on the particle is balanced by the optical scattering force. Later, dual beam optical traps were introduced where particles gets trapped between two counter-propagating moderately focused laser beams. In 1986, Arthur Ashkin and his colleagues reported for the first time that transparent spherical particles can be trapped in three dimensions using the gradient force generated from a single laser source, called single beam optical trap [2]. Since then, optical tweezers found enormous applications, both in fundamental science and technology. Steve Chu implemented this method in the field of atomic cooling and trapping for which he was awarded the Nobel Prize in 1997.

2.2.1 Optical tweezers

Trapping and remote control over micrometer and nanometer sized particles has a significant impact in biology and physics [1, 19, 20]. The most popular tool for optical manipulation of small objects is optical tweezers [2, 18]. Optical tweezers are widely used for diverse applications ranging from molecular motors in biology to the transport of Bose-Einstein condensates in physics [21, 22]. Optical tweezers rely on the momentum transfer between the photons and the dielectric particle [2]. This momentum transfer exerts significant amount of forces on micrometer sized particles (typically in the range from 0.01 to 100 pN) with some mW of laser power. A stable three dimensional (3D) optical trap can be accomplished by focusing a Gaussian laser beam using a high numerical aperture (NA) objective lens [23]. Optical tweezers can handle particles ranging in size from several micrometers to several nanometers, which include spherical transparent particles to biological cells. The trapping force occurs only at the focal point that makes them a suitable tool for single particle manipulation [24].

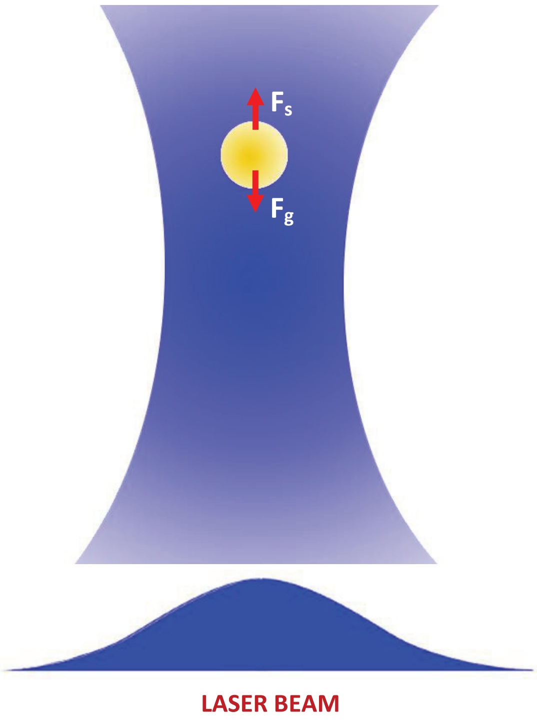

Fig. 2.1: Schematic representation of optical trapping.

The basic principle behind optical trapping is the momentum transfer associated with the refraction or reflection of light at a dielectric interface [25–27]. Fig. 2.1 schematically illustrates the optical trapping mechanism. Suppose light undergoes a momentum transfer of ΔP_{photon}, then according to the conservation of momentum, the particle undergoes an equal and opposite momentum change. This momentum change exerts a force on the particle which is given by rate of change of momentum of the particle. Two types of forces arise at the interface due to the light-matter interaction. First one is the scattering force (F_s) which acts along the direction of propagation of light, and the second one is the gradient force (F_g) which pulls the particle towards the higher intensity region [2]. Stable 3D trapping is achieved when the gradient force exceeds the scattering force. This condition can be achieved by employing high numerical aperture (NA) objective for trapping, preferably higher than one [28]. The optical forces acting on the trapped particles are explained on the basis of different models depending upon the size of the particle (R) and the excitation wavelength (λ) [29]. A detailed description of the trapping mechanism is provided in chapter 3. For a dielectric particle whose radius is much smaller than the wavelength ($R \ll \lambda$), the particle can be considered as an oscillating dipole that is polarized by the slowly varying electric field [2, 30, 31].

The scattering force acting on such a particle is given by [2]:

$$F_s = \frac{I_0}{c}\frac{128\pi^5 R^6}{3\lambda^4} n_m (\frac{m^2-1}{m^2+2})^2 \tag{2.1}$$

and gradient force is given by:

$$F_g = -\frac{1}{2} n_m^3 R^3 (\frac{m^2-1}{m^2+2}) \nabla E_{field}^2 \tag{2.2}$$

where $m = n_p/n_m$ and I_0 is the laser intensity. n_m and n_p represent the refractive index of the medium and that of the particle, respectively. The scattering force is directly proportional to the incident laser intensity and gradient force is directly proportional to the gradient of the intensity. Depending on the value of m, the direction of gradient force can be towards (when $m > 1$) or away (when $m < 1$) from the higher intensity region.

Optical tweezers are a suitable tool for studying the dynamics of molecular motors such as kinesin and myosin [32], also for studying viscoelastic properties of biopolymers (e.g. DNA), cell membranes and composite structures such as chromosomes [33]. Combination of optical tweezers with precise position detection techniques enables to study the interaction between the trapped particle and their surrounding [34]. In many of the biological experiments, trapped particles are used as handles for the measurement. Optical tweezers are used to trap and manipulate nano-structures such as carbon nanotubes and metallic nanoparticles [35]. It is also possible to manipulate defects in nematic liquid crystals [36]. Additionally, optical tweezers can rotate the trapped particles by different methods based on transfer of spin or orbital angular momentum [12] or rotating light patterns [37]. Holographic optical tweezers are employed for parallel manipulation of microparticles and cells [38, 39]. For the particles with refractive index smaller than that of the surrounding medium, methods like optical vortex trap [40] and trapping using Laguerre Gaussian modes [41] are employed.

Two major limitations are the comparatively high light intensities required for optical trapping (about $10^6\ W/cm^2$) and the unfavorable scaling of the optical forces with the size of the trapped object ($F_g \propto R^3$) [2]. In the Rayleigh regime, the optical gradient force diminishes rapidly as the particle radius decreases. So the manipulation of nanoparticles is a challenge. Moreover, for nanoparticles, Brownian motion is significant. The thermal effects due to the high intensity irradiation on the trapped particle is not desirable, especially while handling biological samples [42,43]. Also, the selection of the trapping source is crucial. For the manipulation of biological samples, near-infrared lasers are used as trapping sources in order to minimize opticution [42]. Another critical requirement for optical tweezers is the requirement of a high NA objective lens. Still, the minimum spot size that can be achieved is limited by the wavelength. Theoretical limit of minimum lateral spot size is $0.61\lambda/NA$ [44]. Usually, this value is around 500 nm. As a result, both the manipulation and imaging of objects smaller than diffraction limited spot size is a challenge. Also, the small field of view of high NA lens (typically less than 100 μm x 100 μm) limits the effective manipulation area for parallel manipulation. Furthermore, when distributing the light intensity over an optical "landscape" as in the case of holographic optical tweezers [38,39], each of the individual traps of a tweezer array only shares a fraction of the photon flux of the laser beam. Therefore, since a specific threshold intensity is required to manipulate small objects, there is only a limited flexibility in creating different optical landscapes with a laser of given power.

To overcome the fundamental limitations of optical tweezers, near-field optical techniques have been proposed and found several applications [45]. The functionality of optical trapping mechanism is further expanded to complex optical manipulation of particles using diverse techniques such as evanescent trapping [46], surface plasmon enhanced trapping [47,48] and light-induced electrokinetic trapping [5]. Near-field techniques succeed the requirement of diffraction limited focal spot imposed by conventional optical tweezers. Moreover, they offer intrinsic in-plane confinement of the particles [49]. The following section gives a brief review on the basic theory behind such methods, advantages and limitations.

2.2.2 Near-field techniques

Near-field optics describes the electromagnetic field that exist only in the vicinity of interfaces or sub-wavelength sized structures [44,50]. Near-field optical manipulation of microparticles using evanescent wave was first proposed by Kawata and Sagiura in 1992 [4]. Evanescent waves are generated in the near-field of high refractive index structures (such as prism or waveguide) under the condition of total internal reflection (TIR) [44,51]. TIR occurs when light travels from higher refractive index region (n_1) to lower refractive index region (n_2), at an angle greater than or equal to the critical angle. When a dielectric particle is placed in the evanescent field, the optical gradient polarizes the particle resulting in a strong gradient force direct towards the higher intensity region. This force is analogous to the Lorentz force explained for optical tweezers. Here, a large contrast in refractive index between two media generates a sharp decay of evanescent waves [45]. Exponential decay in intensity of the evanescent waves at a distance s from an interface can be written as [51, 52]:

$$I(s) = I_0 exp(-\beta s) \tag{2.3}$$

where

$$\beta = \frac{4\pi}{\lambda}\sqrt{(n_1 sin(\theta_i))^2 - {n_2}^2} \tag{2.4}$$

The gradient force pulls the particle towards the vicinity of the interface while the scattering force due to the evanescent wave guides the particle along the propagation direction. S-polarized light is commonly employed for creating evanescent waves since it produces stronger near-field than those associated with p-polarized light [53]. Important applications of evanescent wave trapping include sorting and transportation of microparticles and biological cells [51]. Evanescent wave generated along a channel waveguide can be used to move microparticles along the waveguide [54]. Additionally, it is also possible to manipulate metallic micro- and nanoparticles in the evanescent field [54].

The strength of an evanescent wave decays rapidly with the distance from the interface which may result in a significantly reduced trapping depth [45, 55]. So a counter propagating beam is required to achieve three dimensional trapping [44, 56]. Such a counter-propagating geometry is employed for the confinement of particles above the waveguide or creating a particle array at the interface [57]. The disadvantage is that usually this method is limited to polarizable objects only. Furthermore, the gradient force vanishes as the particle size reduces down to nanoscale.

Another important development in the near-field techniques is the surface plasmon trap [47]. Surface plasmons are collective oscillations of free electrons on metal surfaces [48, 53]. Surface plasmon resonance can occur in the visible or near-infrared region of the electromagnetic spectrum in metals such as gold, silver, copper and aluminum [48]. Depending on the structure of the metal surface, the excitation can be divided in to two: surface resonance plasmons for flat metal surfaces and localized plasmons resonance for metal nano-structures [53, 58]. The field distribution on the metal surface can be tuned by patterning the metal with nano-structures. This allows the confinement of particles in a small trapping volume governed by the dimension of the metal nano-structures [53]. The resonance occurs when the frequency of the incident light wave matches well with the natural frequency of the oscillating electrons. At the resonance condition, plasmons generate large local enhancements of the electric field strength. This strong electromagnetic gradient formed near the metal structures enable the trapping of nanoparticles. It is reported that the trapping force can be enhanced about 40 times at a given intensity compared to conventional optical tweezers [49].

The above mentioned optical methods (free space and near-field techniques) require either complex optics or patterned metal surfaces to achieve stable trapping. To realize more flexibility on trapping and transport, methods which combines optics with other particle manipulation techniques have been explored [5, 59]. Combination of light with electrokinetic particle manipulation techniques like dielectrophoresis and electroosmosis have been reported recently and found numerous applications [5, 8].

2.3 Light-induced electrokinetic transport

Electrokinetic phenomena like dielectrophoresis and electro-osmosis are widely used for the manipulation of micro- and nanoparticles [60–62]. Their combination with light has opened a new era in the field of optofluidic particle and droplet manipulation. These methods overcome the requirement of high light intensity and complex optics imposed by the conventional optical methods.

Optoelectronic tweezers (OET) rely on the light-induced dielectrophoretic force which is utilized to trap and manipulate microparticles, nanoparticles and droplets [5, 59, 63, 64]. Dielectrophoresis (DEP) is a phenomenon in which the force is exerted on a dielectric particle when it is subjected to a non-uniform electric field [53]. Dielectrophoresis was first reported by H. A. Pohl in 1951 [65]. A dielectric particle placed in such a non-uniform electric field gets polarized and charge dipoles are established in the particle. The orientation and the magnitude of the induced dipole depends on several parameters such as dielectric properties of the particle and the suspending medium, intensity and the frequency of the applied electric field.

The time averaged DEP force acting on a particle of radius R can be expressed as [53]:

$$F_{DEP} = 2\pi R^3 \epsilon_m Re\left[K^*(\omega)\right] \nabla(E_{rms}^2) \tag{2.5}$$

where E_{rms} is the root mean square value of the electric field at the particle, $K^*(\omega)$ is the Clausius-Mossotti factor. $K^*(\omega)$ is given by [53]:

$$K^*(\omega) = \frac{\epsilon_p^* - \epsilon_m^*}{\epsilon_p^* + 2\epsilon_m^*} \tag{2.6}$$

where $\epsilon_p^* = \epsilon_p - j\frac{\sigma_p}{\omega}$ and $\epsilon_m^* = \epsilon_m - j\frac{\sigma_m}{\omega}$ are the complex permittivity of the particle and the medium respectively. σ_m and σ_p denote the conductivities of the media and the particle respectively and ω is the frequency of the AC potential. Depending on the value of $K^*(\omega)$, the dielectrophorectic force can be either positive or negative [59].

Typically, an OET setup consist of a conductive glass substrate, a particle solution and a photoconductive material. An AC voltage is applied between the conductive substrate and the photoconductive material. Irradiation with light increases the conductivity of the photoconductor, resulting in the creation of large electric field gradients. A dielectric particle placed in such a field experiences a strong DEP force. Chiou et al. demonstrated the manipulation of 4.5 μm polystyrene particles and biological cells using OET [63]. The particle suspension is sandwiched between a photoconductive surface and a conductive glass substrate, which is connected to an AC signal. Amorphous silicon is a commonly employed photoconductor for OET, because they exhibits high resistance in the absence of light and high conductivity in the presence of light. Illumination with light turns the photoconductive material from an insulating state to a conducting state that create a non-uniform electric gradient that enables the particle manipulation. Here, optical energy is not directly utilized for trapping. So very low intensity ($< 1\ W/cm^2$) is sufficient for particle manipulation [5]. The lower requirement of light intensity allows the manipulation of living cells without photo-damage.

Nanoparticle manipulation with OET is a challenging task since the dielectrophoretic force scales to the third power of the particle diameter. However, trapping of nanostructures such as nanowires and carbon nanotubes are possible because their length comes in micrometer order. Jamshidi et al. employed OET for the trapping and manipulation of silver nanowires having a diameter of 100 nm and length of 5 μm [66].

Moreover, they could differentiate silver and silicon nanowires based on their DEP mobility. OET have also been utilized to trap quantum dots and single carbon nanotubes [67]. Furthermore, OET creates real time dynamic OET virtual electrodes which makes them a promising candidate for individual particle manipulation for a large area. Massive parallel manipulation is achieved by creating light patterns using spatial light modulators [5].

A promising way to achieve nanoparticle trapping and manipulation is the use of hydrodynamic force instead of optical or electrical forces. Hydrodynamic force scales linearly to the particle dimension. Recently, light-actuated electro-osmosis has been demonstrated to be capable of manipulating nanoparticles [8]. Incorporating a photoconductive layer on a microfluidic substrate, several authors demonstrated the control and generation of fluidic flow using light-induced electro-osmosis [68–70]. The following section is dedicated to the recent advances in light-induced microfluidic flow with an emphasis on droplet and particle manipulation.

2.4 Microfluidic actuation by light-induced modulation of surface stresses

Microfluidic devices offer potential applications in biological science, chemical science and medicine due to their small volume requirement, high sensitivity and high throughput analysis [53]. Since the development of micro-scale devices known as lab-on-a-chip devices, microfluidic technology found numerous applications, ranging from biological analytics to small scale energy production [71, 72]. To mention a few are drug screening, tunable fiber optic waveguide, DNA microarrays, optofluidic sensors, optofluidic lasers and clinical analysis [7,73]. Furthermore, the small scale devices have additional advantages like minimized usage of chemical reagents, increased automation, reduced manufacturing cost and better accuracy compared to the large scale devices [74]. The characteristic geometry of a microfluidic channel offers a large surface area to volume ratio, which makes the surface forces dominant over inertial forces. Microfluidic flows are characterized by their laminar flow [75]. The Reynolds number associated with the microfluic flow is typically less than one. Fluid transport at the microscale is described by the continuity equation (conservation of mass) and the Navier-Stokes equations (conservation of momentum). The Navier-Stokes equations is discussed in chapter 5.

Control over microfluidic flow and transport of small droplets and particles is a crucial challenge in microfluidics. Usually, these processes include complex techniques and geometry. Handling of a small amount of medicine and hazardous chemicals require a high amount of accuracy and flexibility. Controlled manipulation of small objects at fluid-fluid or fluid-solid interface has been demonstrated using different techniques such as electrowetting [13], thermocapillary [14], dielectrophoresis [3], magnetic force [15], thermo-chemical effect [16] and optical forces [76–81].

Manipulating surface tension or interfacial tension provides a natural tool for the regulation of microfluidic flows because surface forces dominate over inertial forces when the surface to volume ratio is large [75]. Gradient in surface tension develops a hydrodynamic flow along the interface from the lower surface tension region to the higher surface tension region, known as Marangoni flow [82]. When considering particle manipulation by hydrodynamic forces, the hydrodynamic drag force given by Stokes equation comes into play [75]. The detailed description on the interfacial transport phenomena is given in chapter 5. This hydrodynamic flow can be utilized to induce microfluidic flow and manipulation of small objects. The basic principle behind these methods is the surface energy modification either by variation in temperature, concentration or electrical potential. The hydrodynamic nature of the trapping mechanism implies a force scaling with the particle diameter instead of its third power as in the case of conventional methods like optical tweezers and dielectrophoresis [2].

An important development in the field of microfluidics is the marriage of light with fluids, known as Optofluidics [7]. Optofluidics aims at manipulating fluid properties using light at the micro- and nanoscale. Unification of optics with microfluidics has enormous applications in the field of biophotonics, information processing, sensors and tunable optical elements [6, 83, 84]. The ability of light-induced techniques to produce non-contact, tunable and compact devices make optofluidics device a unique tool for creating lab-on-a-chip devices.

Light-induced droplet manipulation techniques rely on direct optical forces [76–81], opto-thermal effect [85–88], opto-electronic effect [8, 89], light-induced surface energy modification [9, 90] and chromocapillary effect [10, 91]. Direct optical force techniques based on scattering force (optical levitation) [76, 77] or gradient force (optical tweezers) [78, 79] for the trapping, transportation and fusion of fL - pL droplets. Optical vortex trap also utilized for the manipulation of small droplets [40]. Since optical forces are of the order of pN only, manipulation of fast flowing droplets using light is a challenging task [58, 80]. The following section focuses on particle and droplet manipulation based on light-induced surface energy modification.

2.4.1 Light-induced manipulation using opto-electrowetting

Electrowetting is an effective mechanism for the transport and mixing of droplets at the micro-scale [13, 92]. The wettability can be increased on applying an electric field at the three phase contact line that pulls the contact line outward. In a typical electrowetting system, a polarizable droplet is placed on a dielectric substrate and the electric field is applied between the droplet and the electrode. The equivalent circuit of the electrowetting setup consist of a series combination of the dielectric capacitance and the double layer capacitance. The droplet acts like a conductor with a resistance R_d. On applying the electric field, surface energy at the solid-liquid interface is modulated, which results in change in contact angle of the liquid drop [13]. Voltage dependence of contact angle is given by:

$$cos\left[\theta(V_A)\right] = cos\theta_0 + \frac{1}{2}\frac{\epsilon}{d_l\sigma_{LV}}V_A^2 \tag{2.7}$$

where V_A, d_l, ϵ and γ_{LV} are the applied voltage, thickness of the insulating layer, dielectric constant of the insulating material and the liquid-vapor interfacial tension, respectively [92]. The rapid change in contact angle induced by electrowetting found potential applications for the fabrication of tunable optical elements [93,94]. However, for the transport of droplets using electrowetting require complex array of electrodes that presents a challenge for the microfluidic chip fabrication [89, 95]

To achieve opto-electrowetting, a photoconductive layer is integrated below the electrodes of the usual electrowetting setup [89, 96]. Usually, the circuit comprises of a liquid, an insulator layer and a photoconductor layer. Contact angle change depends on the voltage drop across the insulator [53]. The frequency of the AC voltage is adjusted in such a way that, in the absence of light, the impedance of the photoconductor dominates over other components in the circuit. Using a voltage divider, most of the voltage drops across the photoconductor and very little voltage drop across the insulating layer. So the contact angle remains at its equilibrium value. Upon illumination with light, the conductivity of the photoconductive layer increases due to the electron-pair generation which results in the reduction of the impedance of the photoconductive layer (smaller than that of the insulating layer). As a result, most of the voltage drop occurs across the insulating layer, resulting in a change in contact angle. Chiou et al. demonstrated the transport of droplet using opto-electrowetting [89].

2.4.2 Light-induced manipulation using opto-thermocapillarity

It is well known that thermocapillarity is capable of generating microfluidic flow. An increase in temperature reduces the surface tension of the liquid which results in a hydrodynamic flow from the lower surface tension region to the higher surface tension region. This hydrodynamic flow is known as Marangoni flow [82]. At small scale, a small gradient in temperature can induce substantial liquid flow [97]. Young et al. reported the motion of an air bubble immersed in silicon oil by thermocapillary effect [98]. The thermocapillary effect has been utilized for trapping and manipulating tiny quantities of liquid either inside the microchannel or on an absorbing substrate [85]. The temperature difference is achieved either by directly heating the substrate using microfabricated electrical resistors or by laser heating [81]. Optically-induced thermocapillary force has several advantages such as non-contact manipulation, flexible manipulation capability and parallel manipulation of droplets. Besides the above mentioned advantages, the use of light has an additional advantage, as it allows localized heating at moderate laser power. Thus, it allows for generating very high temperature gradient for a localized region.

Light-induced thermocapillary flow is used to generate microfluidic flow [85, 99–101], transport of small droplets along the interface [102, 103] and manipulation of microparticles in the bulk liquid [104]. Garnier et al. demonstrated light-induced movement of a liquid film on a heated surface [99]. Movement of a solid object at the liquid surface was demonstrated by Okawa et al. [105]. They achieved flow velocity up to the order of cm/s. Kotz et al. demonstrated that discrete water droplets can be transported over hydrophobic surfaces using light [102]. They placed water droplets with absorbing dye in an organic phase of 1-decanol taken in a polystyrene petridish. Locally illuminating one edge of the droplet generates a temperature gradient along the droplet resulted the droplet to move towards the colder region. Several other groups also reported the movement of immersed bubbles by light irradiation [100, 106]. When $\frac{\partial \sigma}{\partial T} < 0$, the droplet is attracted towards the hot region (illumination region) and repelled away if $\frac{\partial \sigma}{\partial T} > 0$ [81].

Holographic technology has been used for multi-droplet patterning and droplet merging [86]. Recently, Kurup et al. reported an 'optofluidic tweezer' for the trapping, merging and transport of oil droplets immersed in a water bath using light-induced thermocapillary [107]. However, handling of biological samples using thermal methods could lead to the damage of the sample while transportation. Additionally, on open surfaces, thermal methods can cause problems with the evaporation of the liquid.

Application of light-induced thermal Marangoni flow is further extended for the manipulation of microparticles suspended in a liquid [104]. It is reported that, microparticles dispersed in bulk medium can be transported by locally heating the interface by a laser beam that generates a liquid flow directs away from the hot region. The counter flow developed inside the bulk liquid is used to transport microparticles dispersed in the liquid [104].

2.4.3 Light-induced manipulation using photoswitchable materials

Alteration of chemical composition of a surface changes its surface free energy that controls the wettability properties [90, 108, 109]. Gradient in interfacial energy can be utilized to transport small droplets and particles along the interface. A promising way to fabricate wetting pattern is to use light sensitive materials. Azobenzene is the widely used photochromic material for such applications because they are capable of undergoing reversible isomerization in solutions, liquid crystals, monolayers and solids [110]. Moreover, they can be easily incorporated into various types of surfactant systems [111]. Azobenzene undergoes *trans*-*cis* photoisomerization on UV irradiation and the reverse on blue irradiation [112]. A detailed description on azobenzene photochemistry is provided in chapter 5. The first incorporation of azobenzene in a solid surface composition to provide photo-induced wettability change was reported by Siewierski et al. [108] who observed a decrease in water contact angle of up to 9^o upon illumination on a silicon wafer coated by a self-assembled monolayer containing azobenzene. Several other groups also reported light-induced wettability change on monolayer containing azobenzene [113–115]. But the difference in the water contact angle on the *trans* and the *cis* surfaces usually does not exceed 10^o [108, 115, 116].

Some authors explored this method for driving small liquid drops along photosensitive solid surface [9, 90, 117]. Ichimura et al. reported a novel method for the transport of millimeter size droplets over azobenzene immobilized surface [9, 90]. The method relies on the photoisomerization of surface-immobilized azobenzene molecules upon UV - Visible irradiation. A monolayer of azobenzene-terminated calix(4)rescorcinarenes is prepared on fused silica substrate. A gradient in surface energy is created by illuminating the surface with UV - Visible irradiation. Upon illumination with the UV light, the molecule transforms from a polar *trans* state, which exposes the hydrophobic backbone, to a twisted *cis* state. In the *cis* state, the polar azo group is exposed. An olive oil droplet placed on the azobenzene modified surface exhibits a higher contact angle in the *trans* rich state than in the *cis* rich state. Initially, the surface is illuminated with the UV light so that the contact angle of the droplet decreases. This increase in wettability is attributed to the higher dipole moment of the *cis* monomers. Assymmetric irradiation of this *cis* rich surface creates a gradient in wettability over the surface. The wettability gradient enabled the droplet to move along the surface.

A small droplet placed on a flat solid surface has a finite contact angle. Let the equilibrium contact angle be θ_Y. If the droplet is placed on photoresponsive monolayer, illumination on the surface influence the surface energy of the substrate. In this situation, the contact angle θ differs from its equilibrium value. This leads to an imbalance in the horizontal capillary force that results in a pulling force given by [90]:

$$F_c = \sigma(cos\theta_a - cos\theta_r)L_d \tag{2.8}$$

where θ_a and θ_r gives the contact angle at the advancing and receding edge of the drop and L_d represents the base diameter of the drop. This capillary force is responsible for spreading or retraction of the droplet on the substrate. The light intensity and the steepness of the gradient determines the velocity of the droplet motion. A typical velocity of about 35 $\mu m/s$ is achieved with μl droplets. The direction of flow can be reversed by changing the illumination wavelength from blue to UV. However, a specific chemical protocol has to be followed to achieve light-driven droplet motion. Some authors followed this method but the manipulation of water droplets has never been achieved because of the large hysteresis of contact angles [117]. As a result, this method is limited to specific types of liquid [91]. Though several authors reported the light-induced wettability change on hydrophobic surfaces to reduce hysteresis, movement of water droplets over such surfaces is yet to be realized [118–120].

Recently, Diguet et al. proposed a novel technique for the transport of millimeter sized oil droplets over a photosensitive liquid surface [10]. The method relies on optically-induced Marangoni flow [10,91]. The light sensitive surface contains photoswitchable azobenzene molecules. If the surfactant is adsorbed at an interface, *trans*-*cis* photoisomerization results in an increase in surface tension. Subsequent illumination with blue light switches the *cis* molecule back to its *trans* form resulting in a decrease in surface tension. So the surface tension can be locally manipulated by light illumination. Local change in surface tension generates Marangoni flow from the lower surface tension region to the higher surface tension region. The hydrodynamic flow generated at the water-oil interface is utilized to move the oil droplet. The interfacial tension between the floating oil droplet and the solution is modulated by changing the laser wavelength. The change in interfacial tension induces a circulatory motion inside the droplet that is confirmed by monitoring the motion of microparticles added to the oil droplet. Partial illumination with UV light induces a droplet motion directed away from the illuminated region and illumination with 442 nm results in droplet motion direct towards the illuminated region. A typical droplet movement velocity of about 300 - 400 $\mu m/s$ is reported. A two-color illumination allows to trap and manipulate droplets with high precision using chromocapillary effect. Since low light intensity is sufficient to trigger photoswitching, local heating due to laser irradiation can be avoided [91]. However, the proposed mechanism behind the droplet movement (interfacial flow at the liquid-liquid interface) is not applicable in the case of solid particles. So manipulation of small particles cannot be achieved by this method.

Application of photosensitive materials has been extended for the manipulation of colloidal particles in liquid crystals incorporated with a photoswitchable azobenzene group [121–123]. Angel et al. demonstrated that microparticles can be rotated and transported on light sensitive liquid crystals with 10^3 to 10^4 times less light intensity than conventional optical tweezers [123]. Another advantage of this method is the centimeter-scale, massively parallel manipulation of particles and colloidal structures. An alternate way for the manipulation of nanoparticle is proposed by Abid et al. using polystyrene nanoparticles with an azobenzene group attached [124]. Photoswitching of these molecules induced the translational motion of the particles.

A recent work by Chevallier et al. proposed a new mechanism to induce hydrodynamic flow based on light-induced Marangoni effect using photosurfactant containing azobenzene [125]. On illumination with light (either UV or blue) on blue adapted photosurfactant solution increases the surface tension of the illuminated area due to the fast desorption of the *cis* molecules from the interface to the bulk. They observed the accumulation of talcum powder near the illumination region upon irradiation with UV or blue illumination. However, details on intensity or concentration dependence of the particle accumulation is not discussed by the authors.

In this context, this thesis demonstrates a novel method for the trapping and manipulation of microparticles adsorbed to the air-water interface. The method relies on the photoswitching of photosurfactant incorporated with azobenzene. Upon focused illumination with 325 nm laser beam, molecules switch from a *trans* state to a *cis* state resulting in an increased surface tension in the illuminated area. This localized increase in surface tension drives liquid flow towards the laser focus. This inward flow is utilized to trap the particles. Detailed mechanism and the results are presented in the chapter 5 and 6 of this thesis. Rigorous analysis on the dependence of flow velocity on laser intensity, laser exposure time and surfactant concentration is performed. Moreover, it is demonstrated that the direction of the flow can be reversed on switching the wavelength from 325 nm to 442 nm. Furthermore, optically-induced Marangoni flow is used for trapping and manipulation of a single particle along the liquid surface.

3 Optical trapping in a microfluidic channel

3.1 Introduction

This chapter consists of three parts. The first part details the theoretical description while microparticles trapped inside a microfluidic channel. This section explains the nature of the flow profile inside a microfluidic channel. Part two discusses the experimental techniques adopted in this work. This section includes the protocol followed for the microfluidic channel fabrication and features of the each component employed in optical tweezer setup. The trapping optics include the design considerations of the optical tweezers such as laser beam parameters, beam steering optics, inverted microscope and the imaging system used. The same experimental setup is utilized for the experiments discussed in this chapter and the next chapter. The results and discussion part explain dependence of laser power and particle radius on maximum lateral escape force, maximum lateral displacement of the trapped particle and the lateral trapping stiffness.

3.2 Physics of optical trapping

The basic principle behind optical trapping is the momentum transfer associated with the refraction or reflection of light at a dielectric interface [25–27]. Light carries momentum in the direction of propagation which is given by:

$$P_{photon} = h/\lambda \tag{3.1}$$

where h is the Plank constant and λ is the wavelength of the light. The associated energy of the photon can be calculated by:

$$E_{photon} = P_{photon}c = hc/\lambda \tag{3.2}$$

where c is the velocity of light in vacuum. At the dielectric interface, light undergoes both the reflection and refraction resulting in momentum transfer between the photons and the dielectric particle. Suppose light undergoes a momentum transfer of ΔP_{photon}, then according to the conservation of momentum, the particle undergoes an equal and opposite momentum change. This momentum change exerts a force on the particle which is given by rate of change of momentum of the particle.

The restoring force acting on a particle trapped by optical forces can be expressed as [25]:

$$F_p = Q_t \frac{n_m P}{c} \tag{3.3}$$

Where Q_t is the dimensionless trapping efficiency which depends on the particle size and the refractive index difference between the media, and the particle and P is the laser power.

Two types of forces arise at the interface due to the light-matter interaction. First one is the scattering force (F_s) which acts along the direction of propagation of light and the second one is the gradient force (F_g) which pulls the particle towards the higher intensity region [2]. Scattering force pushes the particle along the direction of propagation of light. Scattering force is proportional to the laser intensity while gradient force is proportional to the intensity gradient. So there should be a force balance condition to achieve stable trapping. Stable 3D trapping is achieved only when gradient force exceeds the scattering force ($F_g > F_s$). This condition can be achieved using high numerical aperture (NA) objective lens for trapping, preferably higher than one [28].

Based on the trapping wavelength (λ) and the particle radius (R), optical trapping can be described mainly in three regimes [29]. First one is the ray optics regime ($R \gg \lambda$) and the second one is the Rayleigh regime ($R \ll \lambda$) [25, 126]. However, the transition region, requires complicated theoretical approaches such as generalized Lorentz-Mie theory (GLMT) to explain the optical force acting on the particle [127, 128]. Fig. 3.1 schematically represents the classification based on particle size and laser wavelength. In all three regimes, the net push or pull acting on the dielectric particle from the focal region of the incident laser beam depends upon the relative refractive index between the particle and the surrounding medium.

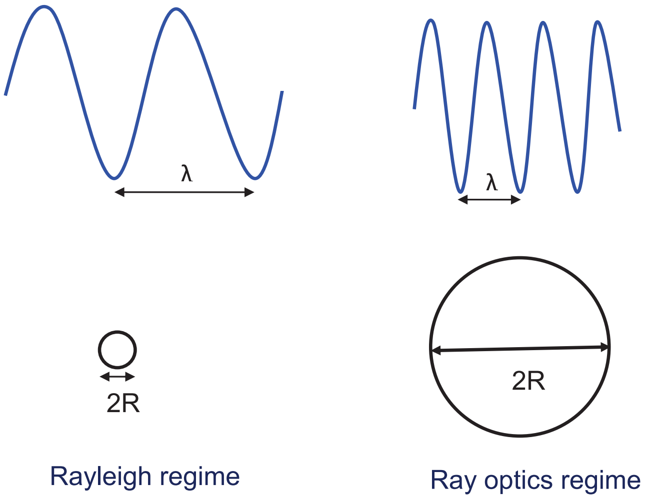

Fig. 3.1: Schematic representation of Rayleigh and Ray optics regime based on the laser wavelength and the particle diameter.

Ray optics regime

If the particle is much larger than the wavelength (R » λ), ray optics or geometrical optics model explains the trapping mechanism [2]. In ray optics model, light beam is composed of individual rays and each light ray hits the dielectric interface and undergoes multiple reflection and refraction. As a result, both the scattering and gradient force exerted on the particle. The scattering force is generated by the momentum change of the particle due to reflection of the light rays at the dielectric interface and the gradient force is generated due to the refraction of the light rays. Fig. 3.2 schematically represents the optical trapping mechanism for a particle comes under ray optics regime. Two identical rays (marked as ray A) are incident on a dielectric particle having radius R at an incident angle θ_i and get refracted at an angle θ_r. Refractive index of the particle is n_p and that of the medium is n_m. The direction of the gradient force exerted on the particle by each ray is marked as F_A. The net force exerted on the particle is the vector sum of gradient and scattering force acted on the particle by each ray.

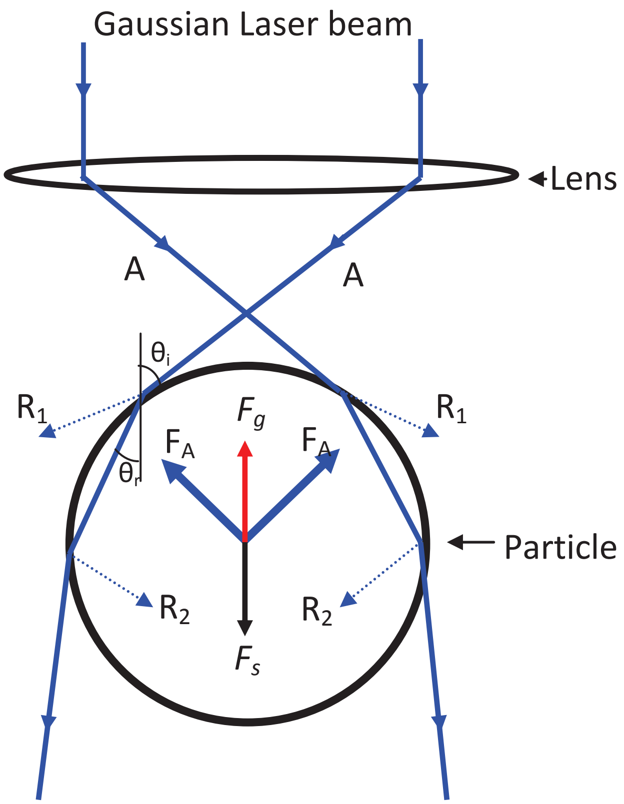

Fig. 3.2: Schematic representation of the optical trapping mechanism in Ray optics regime.

The scattering force can be written as:

$$F_s = \left\{ 1 + R_{Fresnel} cos(2\theta_i) - \frac{T^2_{Fresnel}[cos(2\theta_i - 2\theta_r) + R_{Fresnel} cos(2\theta_i)]}{1 + R^2_{Fresnel} + R_{Fresnel} cos(2\theta_r)} \right\} \frac{n_m P}{c} \tag{3.4}$$

and in the case of gradient force:

$$F_g = \left\{ R_{Fresnel} sin(2\theta_i) - \frac{T^2_{Fresnel}[cos(2\theta_i - 2\theta_r) + R_{Fresnel} cos(2\theta_i)]}{1 + R^2_{Fresnel} + R_{Fresnel} cos(2\theta_r)} \right\} \frac{n_m P}{c} \tag{3.5}$$

where θ_i is the angle of incidence, θ_r is the angle of refraction and $R_{Fresnel}$, $T_{Fresnel}$ are the Fresnel coefficients for refraction and reflection respectively.

Rayleigh regime

For a dielectric particle whose diameter is much smaller than the wavelength ($d \ll \lambda$), the particle can be considered as on oscillating dipole that are polarized by slowly varying electric field [2, 30, 31]. Such particles comes under Rayleigh regime and the Lorentz force is used to calculate the trapping force. For a dipolar particle placed in an arbitrary monochromatic wave with angular frequency ω, the electric field can be expressed as [44]:

$$\mathbf{E}(r,t) = Re\left\{\underline{\mathbf{E}}(r)e^{-i\omega t}\right\} \tag{3.6}$$

where $\underline{\mathbf{E}}(r)$ represents the complex amplitude of the field. Considering the linear relation between dipole and the field, we can write dipole moment as:

$$\boldsymbol{\mu}(t) = Re\left\{\underline{\boldsymbol{\mu}}(r)e^{-i\omega t}\right\} \tag{3.7}$$

Assuming that the partice has no net dipole moment, then the induced dipole moment is propotional to the applied field:

$$\underline{\boldsymbol{\mu}}(r) = \alpha(\omega)\underline{\mathbf{E}}(r) \tag{3.8}$$

where $\alpha(\omega)$ is the polarizability of the particle. Now, considering the complex amplitude of the electric field in terms of real amplitude E_0 and phase ϕ as:

$$\underline{\mathbf{E}}(r) = \mathbf{E}_0(r)e^{i\phi(r)}\hat{\mathbf{n}}_E \tag{3.9}$$

where $\hat{\mathbf{n}}_E$ is the unit vector in the direction of polarization. The time averaged force on the particle is expressed as:

$$< \mathbf{F} >= \frac{\alpha^I}{4}\nabla {E_0}^2 + \frac{\alpha^{II}}{2}{E_0}^2\nabla\phi \tag{3.10}$$

where

$$\alpha = \alpha^{I} + i\alpha^{II} \tag{3.11}$$

The first term corresponds the dipole force (gradient force) and the second terms gives the scattering force. Depending on the value of α, the resultant force can be directed towards the higher intensity region or directed away from the higher intensity region. When $\alpha > 1$, the refractive index of the particle is higher than that of the surrounding medium, the particle is attracted towards the maximum intensity region (towards the laser focus). When $\alpha < 1$, the particle repels away from the focus [126]. For a particle of radius R, the scattering force acting on the particle can be written as [2]:

$$F_s = \frac{I_0}{c}\frac{128\pi^5 R^6}{3\lambda^4} n_m (\frac{m^2-1}{m^2+2})^2 \tag{3.12}$$

and gradient force is given by:

$$F_g = -\frac{1}{2} n_m^3 R^3 (\frac{m^2-1}{m^2+2}) \nabla E_{field}^2 \tag{3.13}$$

where $m = n_p/n_m$ and I_0 is the laser intensity. The scattering force is directly proportional to the incident laser intensity and gradient force is directly proportional to the gradient of the intensity. Thus the intensity gradient can be increased by increasing both the laser power and the convergence angle.

3.3 Optical tweezers in microfluidic environment

In recent years, there has been a considerable interest in integrating optical tweezers along with microfluidics [129–131]. Such an integrated approach is used to study optical sorting, manipulation of single cells, polymer adsorption onto a microsphere and the control of microfluidic flow [11, 132, 133]. The most significant advantage of optical tweezer over other particle manipulation methods is their ability to work on living cells and inside microfluidic channels in a non-destructive and non-contact way. Moreover, optical trapping in a flowing medium reduces the rise in temperature at the focal point which is a prerequisite for biological applications. Several attempts have been made to control or generate fluid motion inside a microchannel driven by optical tweezers [11, 134–136]. Higurashi et al. demonstrated the possibility to generate liquid flow by rotating a trapped particle having anisotropic shape and a rotational symmetry [11]. The net optical torque on the particle because of the momentum transfer from the light rotates the microparticle at a speed of 100 rpm with moderate laser power. An alternate method for this technique is demonstrated by Friese et al. by trapping birefringent particle (calcite particle having 1 μm size) by transfer of spin angular momentum [134]. It is also reported that micro gear shaped structures can be trapped and rotated [12]. These systems can be applied to develop light driven micropumps and microstirrers. Terray et al. reported the fluid motion in a microchannel driven by optical tweezer. They used a time shared optical trap for activating the motion of the trapped particles working as a two-lobe gear pump. They achieved a maximum flow rate of 17 pL/min in 6 μm x 3 μm microchannel [135]. This setup can be used to develop an optical valve that controls the fluid motion. Optical trapping force is of the order of some pN only, so this system can be used at very low flow rate only. Leach et al. developed a micropump in a microfluidic channel by trapping two counter rotating birefringent particles using a polarized laser beam to achieve a maximum flow velocity of 8 $\mu m/s$ between the rotating particles in the channel [136]. Wu et al. demonstrated a shear stress mapping sensor based on microparticles trapped in a microchannel which can be extended to the case of biological cells trapped inside a channel [137]. Recently, Landenberger et al. reported an optical cell sorter system based on steerable optical tweezers incorporated in a microchannel [138]. This system can be used to transport fluorescently labeled cells from the analysis region to the collection region [58, 139]. E. Eriksson reported the observation of changes in the cell volume when they moved the trapped yeast cell between 2 media in 0.2 s time frame [130]. They used a Y shaped microchannel and passing two different fluids through the inlets. This method allows to get the information about the behavior of the cell at different environmental conditions.

In spite of the emerging importance of integration between microfluidics and optical tweezers, there is no report on the particle size dependent behavior of an optical trap in a microfluidic channel. This work reports the size dependent response of silica particles in an optical trap at 442 nm under a pressure-driven flow in a microchannel and compare the results with trapping of corresponding particles in a conventional sample chamber.

3.4 Velocity profile in microfluidic channel

The pressure-driven flow through the microchannel has a parabolic velocity profile with a close-to parabolic shape (Poiseuille profile). The parabolic nature of the velocity profile in microfluidic channel is shown in fig. 3.3.

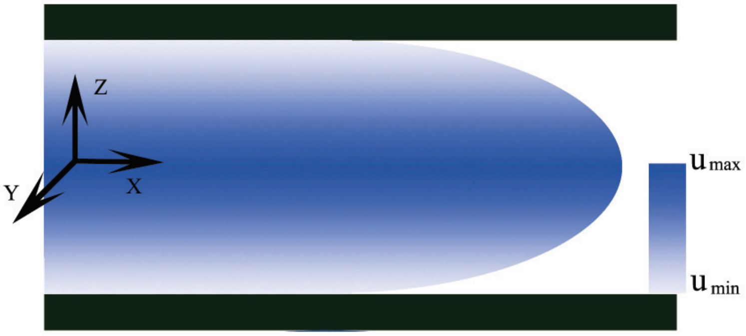

Fig. 3.3: Parabolic velocity profile in a microfluidic channel.

In the case of incompressible flow through a rectangular channel oriented along the X-axis, obeying the no-slip boundary condition (zero velocity at the channel walls), the flow velocity at the position *(y, z)* is given by [137]:

$$u_x(y,z) = \frac{-16\Delta p}{\pi^4 \mu L} \sum_{n=1,3,..}^{\infty} \sum_{m=1,3,..}^{\infty} \frac{1}{nm(\frac{n^2}{w^2}+\frac{m^2}{h^2})} \sin(n\frac{\pi}{w}y)\sin(m\frac{\pi}{h}z) \tag{3.14}$$

where ΔP is the pressure drop in the channel and L is the length of the channel. For a rectangular channel, the pressure drop is given by [140]:

$$\Delta p = 16\pi^2 \mu Q I_p^* \frac{L}{A^2} \tag{3.15}$$

Here μ is the viscosity of the medium, Q is the flow rate through the channel, I_p^* is specific polar moment of inertia of the microchannel having a cross sectional area A and is given by [141]:

$$I_p^* = \frac{I_p}{A^2} \tag{3.16}$$

For a microchannel having rectangular in cross section, the moment of inertia I_p is given by:

$$I_p = \frac{hw}{12}(d^2 + w^2) \tag{3.17}$$

where d is the depth of the channel and w its width. For the flow rates used in the present studies, the Reynolds number R_e is less than 0.5. R_e is calculated using the equation:

$$R_e = \rho_m V D_h / \mu \tag{3.18}$$

where ρ_m is the density of the fluid, V is the average velocity and D_h is the characteristic length or hydraulic diameter of the channel. Hydraulic diameter of a rectangular channel is given by:

$$D_h = \frac{2dw}{d + w} \tag{3.19}$$

3.5 Force balance condition in an optical trap

At the low Reynolds numbers (in the present case it is less than 0.5), laminar flow prevails. So Stokes law describes the drag force onto a particle caused by a uniform flow very accurately. In the case of a particle moving with a speed ν_p in a fluid flow of velocity u, the hydrodynamic drag force exerted on the particle by the fluid is given by [53]:

$$F_h = 6\pi\mu R(u - \nu_p) \tag{3.20}$$

where R is the particle radius and μ is the fluid viscosity. In the case where particle is stably trapped by the laser trap, the particle velocity ν_p is zero. Then the equation for drag force reduces to:

$$F_h = 6\pi\mu R u \tag{3.21}$$

In the case of Poiseuille flow, one has to consider an additional term to drag force according to Faxens' theorem (due to parabolic velocity profile) [142]. This contribution includes the Laplacian of the velocity field and hence the drag force in X-direction on a stationary particle becomes:

$$F_h = 6\pi\mu R[u_x(y,z) + \frac{R^2}{6}\nabla^2 u_x(y,z)] \tag{3.22}$$

By neglecting the thermal fluctuations, the net force acting on an optically trapped particle is given by:

$$F_{total} = F_h + F_p \tag{3.23}$$

Optical trapping using a Gaussian beam creates a harmonic potential, the restoring force F_p is given by:

$$F_p = -ka_{trap} \tag{3.24}$$

Where k is the trap stiffness and a_{trap} is the displacement of the particle from the trap center. The parabolic velocity profile influences the axial equilibrium position of the particle. A particle trapped in a parabolic flow profile experiences a velocity gradient that produces a force (Saffman lift force) perpendicular to the flow direction. The Saffman lift force which opposes the gravitational force and is given by [143]:

$$\mathbf{F}_{saffman} = 6.46\sqrt{\rho_m\mu}(u_x - v)R^2\sqrt{\frac{du_x}{dZ}}\hat{\mathbf{e}}_z \tag{3.25}$$

Incorporating the additional contribution due to Saffman lift force, we can write the axial force balance condition as:

$$F_{axial} > [\frac{4}{3}\pi R^3(\rho_p - \rho_m)g + \frac{k_b T}{R} - F_{saffman}] \tag{3.26}$$

where the first term on the right hand side represents the buoyancy force and the second term represents the thermal force. For a particle trapped near the bottom wall, the direction of the Saffman force is opposite to that of the gravitational force as shown in fig 3.4.

Usually, the optical trapping experiments are preformed in a sample chamber and the escape force is determined by moving the sample cell as a whole. Here, the trapped

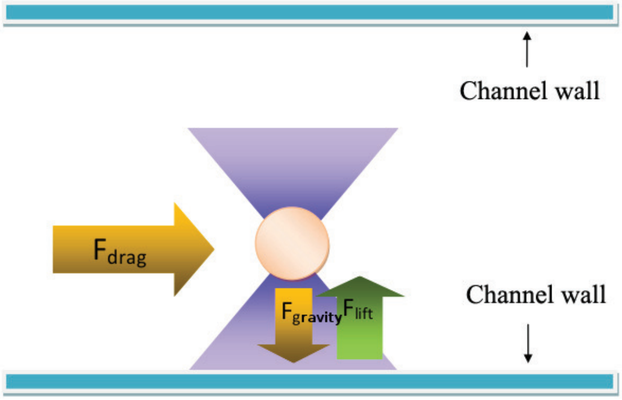

Fig. 3.4: Schematic representation of a particle trapped in a microchannel. Optical gradient force keeps the particle near the focal spot, gravitational force acts downwards and the lift force opposes the gravitational force.

particle experience a uniform velocity profile. Correspondingly, axial force balance condition can be expressed as:

$$F_{axial} > [\frac{4}{3}\pi R^3(\rho_p - \rho_m)g + \frac{k_b T}{R}] \tag{3.27}$$

Similarly, the force balance condition along the lateral direction can be written as:

$$F_{lateral} > [F_h + \frac{k_b T}{R}] \tag{3.28}$$

By neglecting the thermal forces, the force balance condition at the equilibrium position of the trapped particle can be written as:

$$k_x x_{trap} = 6\pi\mu R[u_x(y,z) + \frac{R^2}{6}\nabla^2 u_x(y,z)] \tag{3.29}$$

In the case of particle trapped in a sample chamber, equation for lateral escape force reduces to eq. 3.21. The value of the velocity in the plane of trapping and its Laplacian given in eq: 3.14 was evaluated in MATLAB 7.6 (The Mathworks Inc. U.S.A).

By increasing the flow rate, an optically trapped particle can be displaced from its equilibrium position and eventually move out of the optical trap. By measuring the maximum displacement of the particle in X-direction (measured from the images recorded using a CCD camera), trapping stiffness can be calculated by:

$$k_x = F_{escape}/x_{escape} \tag{3.30}$$

In this study the rotational motion of the particle in a Poiseuille flow is not considered.

3.6 Microfluidic chip fabrication

The microfluidic channel was fabricated using standard soft lithography approach. The master structure was formed on a silicon wafer using UV lithography on a SU-8 photoresist. Fig. 3.5 summarizes the microfluidic channel fabrication procedure.
A curing agent and Polydimethylsiloxane (PDMS) prepolymer (SYLGARD 184 Silicone Elastomer Kit, Dow Corning, Germany) were thoroughly mixed in a 1:10 weight ratio. The mixture was stirred well for 10 minutes so that a homogeneous dispersion was formed. Then the dispersion was placed in a desiccator with a mechanical vacuum pump for 45 minutes to remove any air bubbles. The resulting PDMS mixture was gradually poured over the master structure to a height well above the desired microchannel depth (approximately 4 mm in the present case). The PDMS slab was then cured at 70^oC on the SU-8 mold. The slab was allowed to cool for 180 minutes and then peeled off from the master structure. Due to its hydrophobic nature, a surface modification of PDMS was needed to fabricate closed microchannels with microscope cover slips (Menzel-Gläser, Thermo Fisher Scientific, Germany) of a thickness of approximately 175 μm. The surface modification was done using oxygen plasma treatment by which $-CH_3$ groups of the PDMS surface gets oxidized to form $-OH$ groups. Such a surface modification also facilitates the wetting of aqueous solutions inside the micro channel. The oxygen plasma treatment was performed using a commercial oxygen plasma system (Diener Electronic, Plasma surface technology, Germany). The cover slip was cleaned using methanol and dried before placing it along with the PDMS slab inside the plasma chamber. Following the oxygen plasma treatment for 40 s, the cover slip was bonded to PDMS by pressing the plasma-exposed surfaces on to each other. The height and width of the fabricated channel was then measured to be 100 μm x 85 μm. The length of the microchannel (L) was 5 cm.

In order to enable the pressure-driven flow through the channel, one end of the microchannel was connected to a syringe pump (KD scientific, Germany) through Teflon

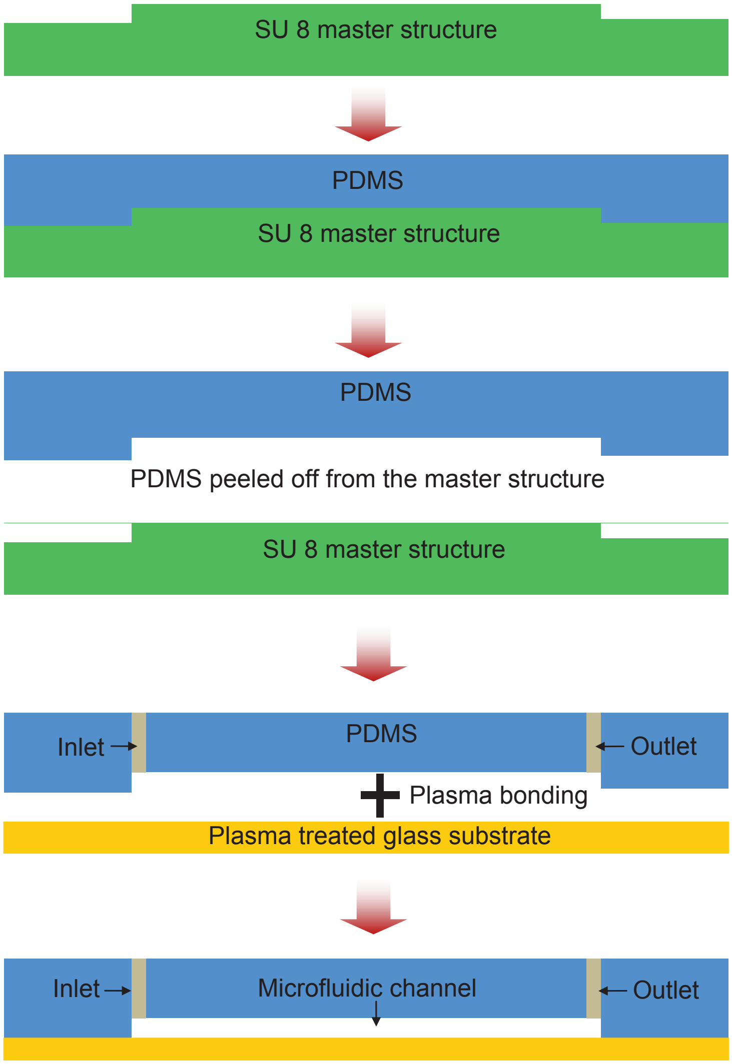

Fig. 3.5: Microfluidic chip fabrication process.

tubing (of inner diameter 600 μm), while the other end was connected to a sink through Teflon tubes of the same diameter as shown in fig. 3.6. The flow rate was controlled using the syringe pump.

3.7 Trapping optics design

Fig. 3.7 shows the schematic diagram of the experimental setup used for particle trapping. The experimental setup and the parameters are explained in detail in this section.

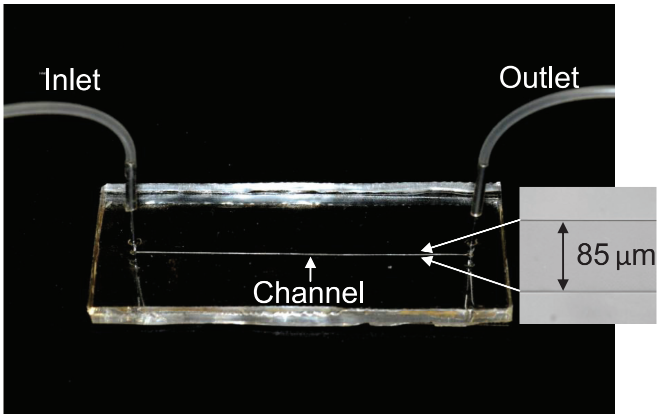

Fig. 3.6: Microfluidic chip fabricated using PDMS. Inlet shows the microscopy image of the channel.

3.7.1 Trapping source

Infra Red (IR) lasers are commonly employed for optical trapping experiments due to the lower absorption of biological cells at this wavelength. Focal volume can be made smaller by employing lower wavelength laser sources for trapping that increases the optical gradient [144]. The present work adopts 442 nm wavelength for optical trapping experiments. Assuming the focal volume is ellipsoidal in shape, IR laser generates a trapping volume of about 1.9 x $10^{-18}m^3$, which is about 15 times higher than that generated by 442 nm laser (trapping volume is about 1.3 x $10^{-19}m^3$). The smaller volume of the 442 nm laser trap enables a higher degree of localization of the trapped particle. Though we can reduce the focal volume, intense irradiation with lower wavelength sources cause undesirable thermal effects for biological and polymer particles. In order to overcome this, particle to be trapped and the surrounding medium has to be chosen in such a way that they exhibit no absorption at the trapping wavelength.

A lower wavelength optical trap was constructed using the 442 nm emission from a He-Cd continuous wave laser (Model IK5651RG, Kimmon Koha Co.Ltd, Japan). Linearly polarized output beam had a Gaussian intensity profile with a beam diameter (D) of 1.2 mm. Laser delivers a maximum power of 80 mW at 442 nm wavelength. Laser takes about 20 minutes for power stabilization and the fluctuation in output power is about ±2% for a continuous operation of 4 h.

An important parameter which ensures the quality of the laser beam is its M^2 number. When the value of the M^2 is unity, the laser has a perfect Gaussian profile. A laser

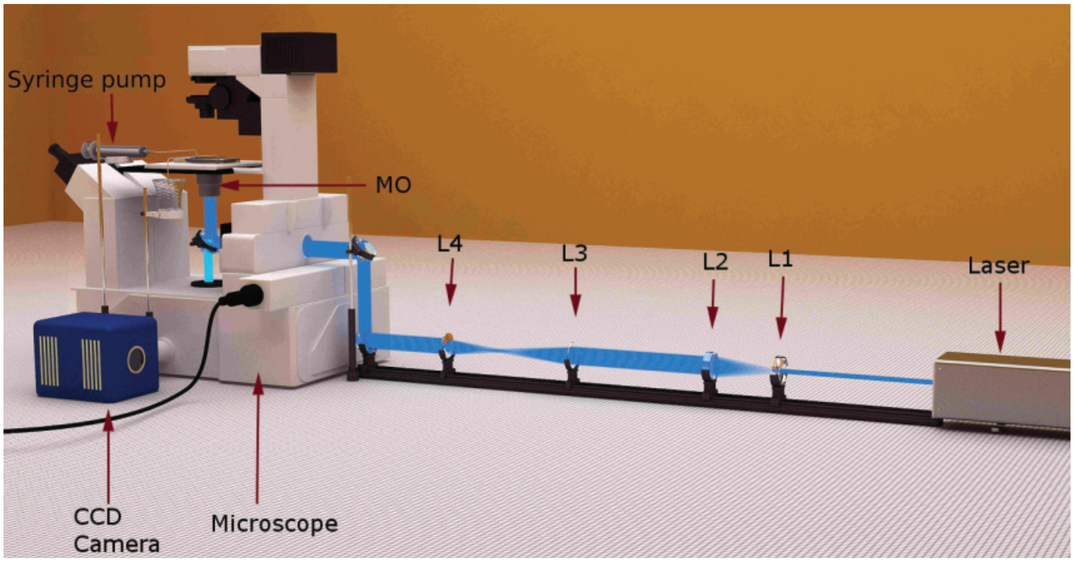

Fig. 3.7: Schematic representation of the experimental setup used for optical trapping at 442 nm.

beam with $M^2 < 1.1$ when focused with an aberration free high NA microscope objective permits to achieve a high quality optical trap [28]. M^2 number of the laser used here is 1.06 which is close to the ideal value.

3.7.2 Beam expander setup

Beam expander is an essential element in an optical tweezer setup. Usually, for trapping experiments, the laser beam has to be expanded to overfill the back aperture of the microscope objective lens. Purpose of this is to achieve maximum possible convergence angle. Two types of beam expanders are commonly employed: Keplerian and Galilean beam expanders. Both the setups consist of two lenses. Keplerian expander consists of two positive focal length lenses separated by a distance equal to the sum of their focal length, while Galelian beam expander consists of one negative and one positive focal length lens. Such a combination requires less optical path than Keplerian expanders. In addition, choice of positive and negative lens cancels the effect of aberrations. Because of these advantages, the present work adopts Galilean beam expander setup. Fig. 3.8 shows the schematic of the Galilean beam expander setup used in this work. The input (lensconcave lens, L1) generates a virtual beam focus for the output lens (convex lens, L2). Present study requires a 9 X beam expander. This because, back aperture size of the microscope objective used for trapping was 7.6 mm. To get the $1/e^2$ intensity of the laser beam at the back aperture of the objective, the beam had to be expanded 9 times. For this purpose, a 1 : 9 beam expander purchased from Bernhard Halle Nachfolger GmbH, Germany was used for the tweezer setup.

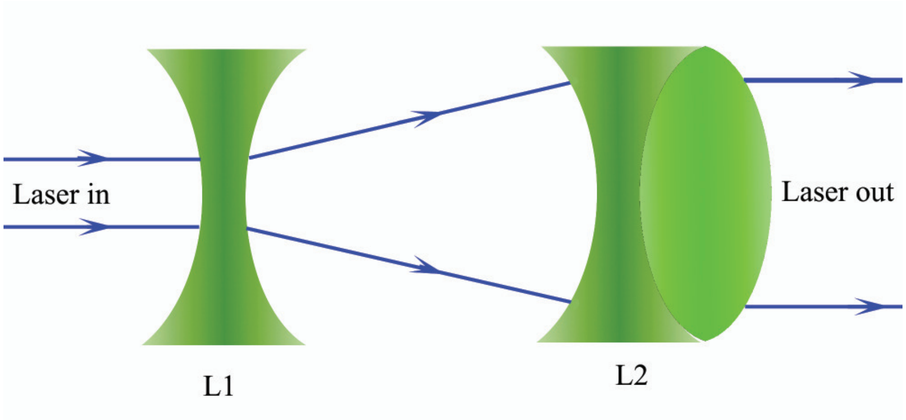

Fig. 3.8: Galilean beam expander.

3.7.3 Keplerian beam steering optics

A Keplerian telescopic arrangement consists of two identical plano-convex lenses (focal length = 25 cm) was used in the setup. Such a system can be used to change the diameter of the laser output beam. If the lenses are kept at a distance equal to the sum of their focal lengths, the setup acts as a beam expander/collimator with a magnification ratio equals to the second focal length by the first. In the present setup, lenses were kept at a distance equal to the sum of their focal lengths. Since the focal lengths of the lenses are same, this system acts as a 1:1 beam expander. This setup can be used to control the beam divergence by changing the spacing between the lenses, i.e, a collimated beam can be made to convergent or divergent, and the reverse (fig. 3.9). This can be used to control the filling factor of the microscope objective lens. Additionally, changing the optical axis of any of these lenses can be used to vary the lateral trapping position.

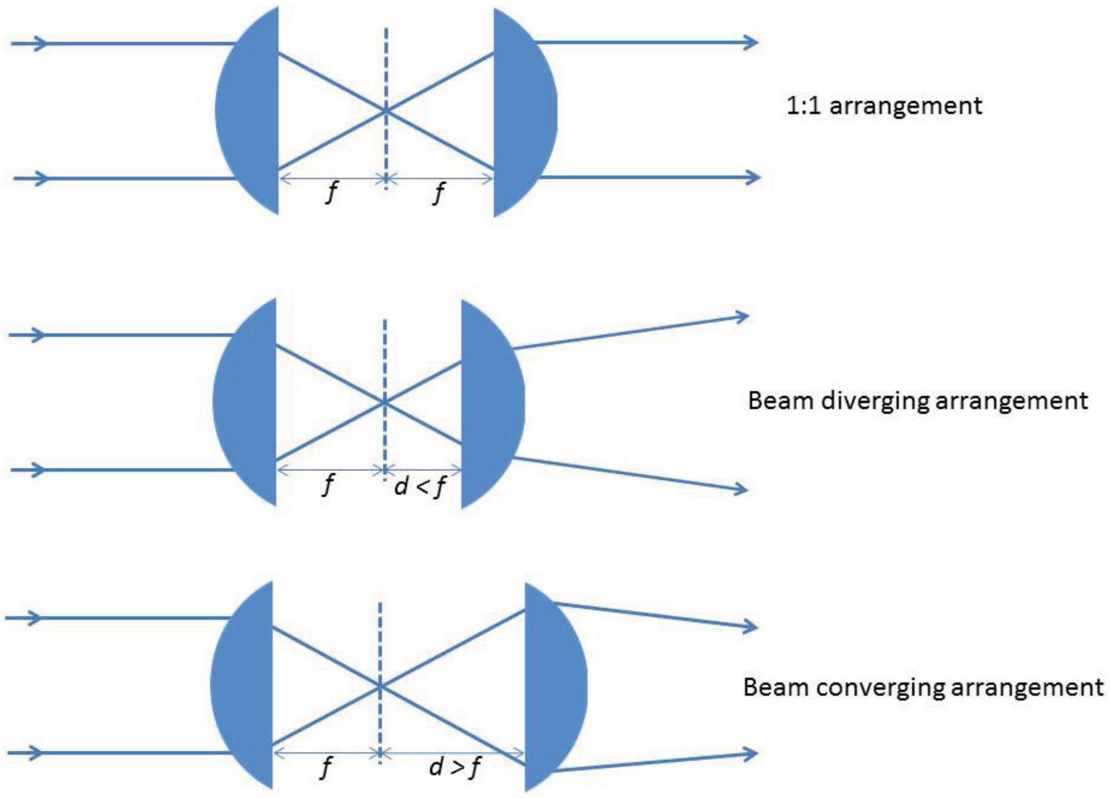

Fig. 3.9: Keplerian beam steering optics

3.7.4 Microscope and imaging system

The microscope used in the present work was Nikon Eclipse, Ti-U model, purchased from Nikon. This microscope was inverted type equipped with the epifluorescence setup. An inverted microscope comprises the bright light source on the top and the objective lenses connected at the bottom pointing up. Nikon microscope was equipped with a CCD camera (ANDOR iXon UV-VIS camera, Model DU-897D-CSO-UVB) for imaging. The images were captured using Andor software. The image analysis were performed using Nikon NIS elements software.

Selection of the objective lens is crucial for optical trapping experiments. Ideally, an aberration free high NA objective lens is preferred (preferably NA > 1). It is reported that, if the NA aperture of the objective is less than 0.8, the intensity gradient generated by the lens is not sufficient to create a 3D trap and results in a 2D trap [145]. Moreover, the size of the focal spot is determined by the NA of the objective lens. In typical optical tweezers setup, objective lens performs two functions at a time: optical trapping and imaging. A Nikon Apo TIRF oil immersion objective (MO) with a NA of 1.49 and 100 X magnification was used for trapping experiments. The NA of an objective lens can be calculated using the formula:

$$NA = nsin(\theta) \tag{3.31}$$

where θ is the maximum converging angle and n is the refractive index of the medium in which the light travels. The immersion oil used for the present study was Nikon 50, Type A oil, MXA 20234 having a refractive index of 1.515. A laser power meter (Newport, Model1918-C) was used to measure the laser power entering at the objective. The transmittance of the objective at 442 nm was 62 % (obtained from the manufaturer). In addition to the trapping laser beam, the focal region was illuminated using an incoherent beam from the Nikon microscope for bright light imaging.

To perform the particle size and displacement measurements, the pixel value of the frame was calibrated. For this, a standard ruler was used. A 25 μm line from the ruler was captured using the Nikon apo TIRF 100X objective and this frame was used as the reference frame. The calibrated pixel value for Nikon Apo TIRF 100X objective was 0.149 $\mu m/pixel$. Nikon NIS software allows the position measurement with an accuracy of 10 nm.

Table. 3.1 shows the calibration results for the different objectives used in this thesis.

Microscope Objective	Frame area $(pixelxpixel)$	Pixel value $(\mu m/pixel)$
100X oil	512 x 512	0.149
50X	512 x 512	0.299
20X	512 x 512	0.751
4X	512 x 512	3.741

Table 3.1: Pixel calibration for different microscope objectives

3.7.5 Focal spot size calculation

An ideal Gaussian beam profile can be focused to form an aberration free diffraction limited spot size. The localized electromagnetic field near the focal point is given by a three dimensional Gaussian beam of axial symmetry having an intensity profile,

$$I(r,z) = I_0 exp(-\frac{r^2}{2\omega_A^2} - \frac{z^2}{2\omega_A^2\epsilon^2}) \tag{3.32}$$

Here ω_A and $\omega_A\epsilon$ are the beam waist radii in the transverse and axial direction. I_0 is the intensity at the focal point $(r = z = 0)$. The focal volume is having an ellipsoidal shape with an eccentricity ϵ. The eccentricity is defined as the ratio between the optical resolution along axial dimension to the optical resolution along the lateral direction. The diffraction limited Airy's spot radius at the laser focus along the lateral direction is given by [28, 44]:

$$\omega_A = \frac{0.61\lambda}{NA} \tag{3.33}$$

Similarly, the axial extend of the trapping volume is given by [44]:

$$\omega_A\epsilon = \frac{2n_m\lambda}{NA^2} \tag{3.34}$$

From eq. 3.33 and eq 3.34, it is clear that both the lateral and axial dimension of the laser focus depends on laser wavelength (directly proportional) and the numerical aperture of the objective lens (inversely proportional). So the combination of lower wavelength and the higher NA objective can produce smaller trapping volume.

3.7.6 Materials

The selection of the trapping wavelength and the particle to be trapped plays a significant role in the performance of the optical trapping system. To avoid the undesirable thermal effects, one has to choose the particles having no absorption band at the trapping wavelength. Commonly employed particles for trapping experiments are dispersed polystyrene micro-spheres. It is reported that the polymer particles are not stable under high intensity visible irradiation [146]. To determine the stability, investigated the photo-degradation of polystyrene particles at 442 nm wavelength and it is found that, these particles undergoes photo-degradation at 442 nm, starts fluorescing and eventually escapes out of the trap [Appendix A]. Therefore, plane silica particles which exhibits no absorption at 442 nm were used. The surrounding medium was Milli Q water which also exhibits minimum absorption at this wavelength. The trapped particle undergoes no photochemical changes even after prolonged irradiation (4 hours). The particles used in this study were dispersed spherical silica beads with diameters ranging from 0.5 - 2.59 μm (Micro particles GmbH and Micromod GmbH, Germany). The refractive index of the particles was 1.42 and their density was 2.2 g/cm^3. The dispersed silica particles were surfactant free and charge stabilized.

3.7.7 Effect of aberration at the glass-water interface

The Nikon TIRF microscope objective employed for trapping obeys Abbe's sine condition (curved lens at the exit) and is free from any inherent spherical aberration. The difference in refractive index between the glass (n_g) and the trapping medium (n_m) result in an increased focal spot at the interface. Although a NA of 1.49 creates an angle of 79.17^o while focusing in the glass, the total internal reflection due to refractive index mismatch at the interface reduces the range of incident angles to values below the critical angle θ_{cr}. The critical angle is given by [147]:

$$\theta_{cr} = arcsin\frac{n_m}{n_g} \tag{3.35}$$

considering $n_m \approx 1.33$ and $n_g \approx 1.55$, then the value of converging angle θ_{cr} becomes 61.25^o. This changes the NA of the objective to an effective NA_{eff} to 1.33. Substituting this effective numerical aperture value in eq. 3.33, the lateral spot size at 442 nm obtained as 0.405 μm. The focal spot size was experimentally determined by recording the Airy's spot created at the glass-air interface and was found to be 0.415 μm. Fig. 3.10 displays the Airy's pattern formed at the glass-water interface.

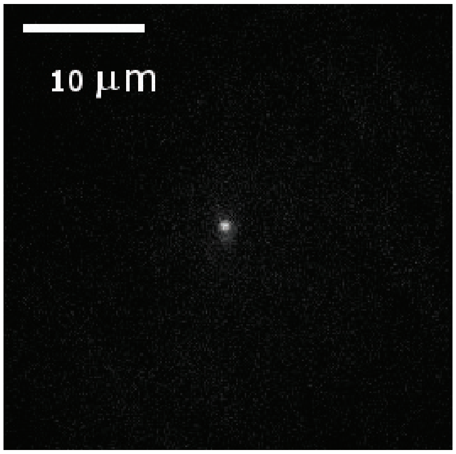

Fig. 3.10: Airys's spot at the glass-air interface formed by Nikon TIRF 1.49 objective at 442 nm.

Calculating the spot size along the axial direction corresponds to 442 nm gives $\omega\epsilon$=1.4 μm, which gives the value of ϵ approximately equal to 4, that matches well with the reported values [148]. Moreover, optical trapping at a depth $l^{'}$ away from the interface causes a shift in the focal plane due to spherical aberration caused by the refractive index mismatch at the glass-water interface as shown in fig. 3.11. The shift in focal

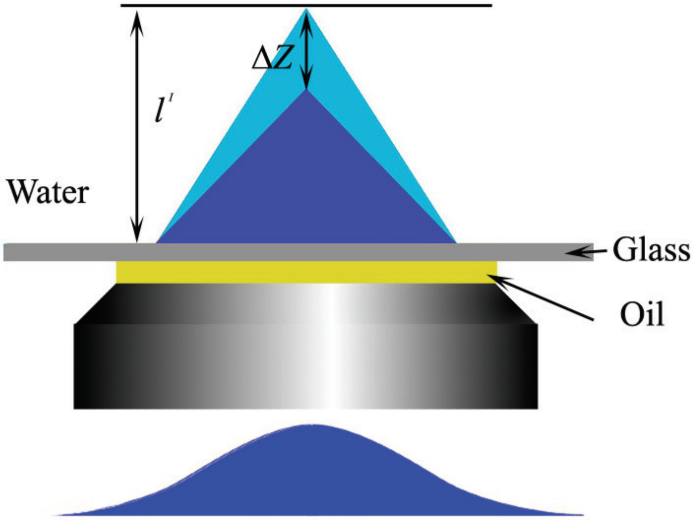

Fig. 3.11: Focal shift due to the refractive index mismatch at the glass-water interface.

spot can be calculated by [149]:

$$\Delta z = [1 - \frac{n_m}{n_g}]l' \tag{3.36}$$

Additionally, the short working distance of the high NA objective limits the trapping of particles at larger depths inside the sample chamber. Hence, in a single beam optical traps, the particles are commonly trapped near to the bottom wall. In the present case, particles were trapped 5 μm away from the coverslip to avoid the interaction between the particle and the coverslip. At this trapping height, the effect of evanescent waves can be neglected. The corresponding shift in the focal spot was 0.6 μm (calculated using eq: 3.36), which results in a trapping at a height of 4.4 μm from the coverslip.

3.8 Escape force method

Escape force is defined as the external force required to remove the trapped particle from the optical trapping potential [126]. Escape force depends on several factors such as laser power, NA of the objective, particle size, ratio of the refractive index of the particle to that of surrounding medium, absorption of the particle etc [23,42]. Any aberration induced by the microscope objective also results in a weaker trap [150].

The commonly employed escape force method which make use of fluid motion around the particle was used here to liberate the particle from the optical trap [151]. Initially the microchannel was placed on the microscope stage and fixed well to prevent it from any vibrations. The position of the laser focus was determined by monitoring the Airy's spot formed at the glass-water interface. Thereafter the laser focus was shifted to the desired trapping height of 5 μm using the focus knob of the microscope. For escape force measurements, diluted silica particles dispersed in water were taken in a 1 ml syringe which was connected to a syringe pump. The outlet of the syringe was connected to the microchannel, and the flow velocity was controlled by the syringe pump. A silica particle was trapped at the laser focus at zero flow velocity. To verify whether the trapped was trapped in three dimensions, the laser spot was moved slightly, and it was verified that the particle follows the beam. To study the effect of laser power and the size of the particle on trapping parameters, experiments were performed at different incident power levels and for different particle sizes. The following sections explain the procedures followed in detail and discusses the results.

3.8.1 Dependence of of laser power on escape force

To study the effect of laser power on the escape force, a set of experiments were performed at four different power levels with silica particles having 3 different sizes, 0.5, 0.85 and 1.5 μm respectively. Fig. 3.12 shows the escape force for four laser power levels (20, 30, 40 and 50 mW). The laser power was measured at the back aperture of the microscope objective using Newport power meter. Initially the particle was trapped at zero applied velocity. The corresponding trapping position was recorded using Andor camera. Then the flow velocity was gradually increased and the corresponding particle displacement inside the trap was recorded. This process was continued until the particle escape from the trap. Average value obtained from 5 measurements is shown in fig. 3.12. Standard deviation of these 5 measurements is shown as error bars. It was found that the escape force of all the particles shows a linear dependence on the laser power. This is because, as the laser power increases more photons interacts with the particle resulting in an increased gradient force [30]. The relationship between trapping force and laser power can be expressed as:

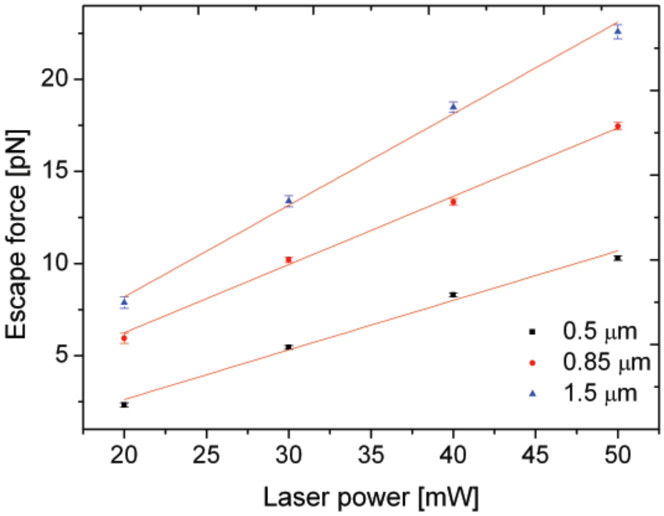

Fig. 3.12: Graph showing the escape force vs laser power for 3 different particle sizes. Escape force increases linearly with the laser power.

$$F_p = \frac{n_m Q_t P}{c} \tag{3.37}$$

where Q_t is the trapping efficiency, c is the velocity of light in vacuum and P is the laser power. The reported values from the literature also shows the similar behavior [27,30].

3.8.2 Dependence of particle size on escape force

To study the dependence of particle size on the trapping force, particle size ranging from 0.5 - 2.59 μm were used. It was possible to efficiently trap bigger particles (5 μm and 8 μm) inside the sample chamber by employing the commonly used methodology for bigger particles (trapping near to the cover slip and then moving the trap to the desired height). However, bigger particles in a microfluidic channel undergo settling at the entrance of the channel due to the influence of the gravitational force. When the particle size is smaller than the focal spot size, particles inside the focus cannot be located.

Experimental method followed to determine the escape force is explained in sec: 3.8.1. The process was repeated for 5 particles, and the standard deviation is calculated and is plotted with error bars. The experiment was performed using three different laser powers 20, 30 and 50 mW respectively. Fig. 3.13 shows that the escape force increases as the particle radius increases. The similar behavior was observed at 3 different power levels. This observation can be explained on the basis of particle size and the trapping wavelength. It is reported that for Rayleigh scattering the maximum

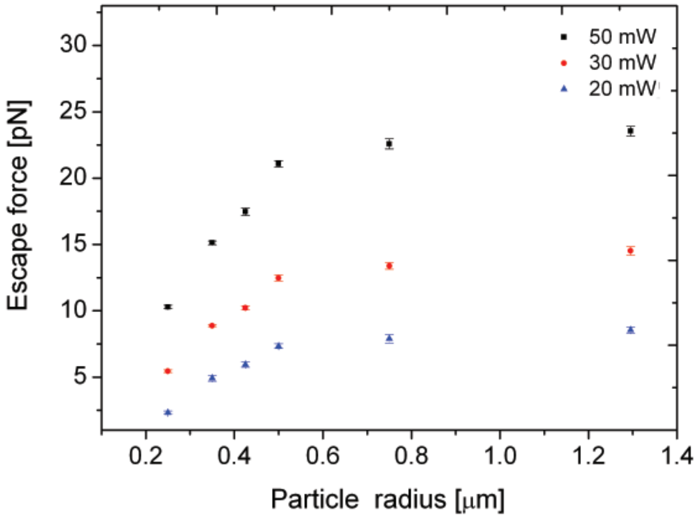

Fig. 3.13: Graph showing the maximum lateral escape force as a function of particle radius at 3 different laser powers.

trapping force exhibits a R^3 dependence, whereas it is independent of size for very large particle (Mie scattering) [152]. However, for the intermediate particle size range as in the present case, the maximum lateral force exhibits a nonlinear dependence on the particle radius, a crossover from the dependence to an asymptotic plateau [148] similar to the behavior observed here.

3.8.3 Particle displacement inside the trap

Methods for the calibration of the optical trapping potential rely on the position detection of the probe particle. Particle displacement from its equilibrium position is a measure of the stiffness of the trap. Mainly two methods have been established for position detection in optical tweezers. First one is the use of quadrant photo diodes, which collect the scattered light from the trapped particle. Accurate calibration of the photo diodes allows to measure the position with accuracy of some nanometers [28, 153]. This method can be used for detecting both the axial and lateral movement of the trapped particle. The second method is based on the image analysis of the trapped particles. This method also allows nanometer resolution by the use of image analysis softwares [126, 154]. Additionally, this position detection method is more flexible and it can be easily extended for the analysis of multiple traps.

The commonly implemented position measurement technique based on image analysis was used here [126, 154, 155]. The pixel calibration of the recorded frame was performed as explained in sec:3.7.4. The particle position at zero velocity was taken as the reference frame. The center of the trapped particle was monitored using Nikon NIS software. The displacement from the equilibrium position was measured from the recorded images captured at each applied velocity. Fig.3.14(Top) shows the image of 2.59 μm silica particle trapped at 30 mW at the equilibrium position. Fig.3.14(Bottom) shows the image of the same particle recorded just before escape from the optical trap (at 560 μm/s).

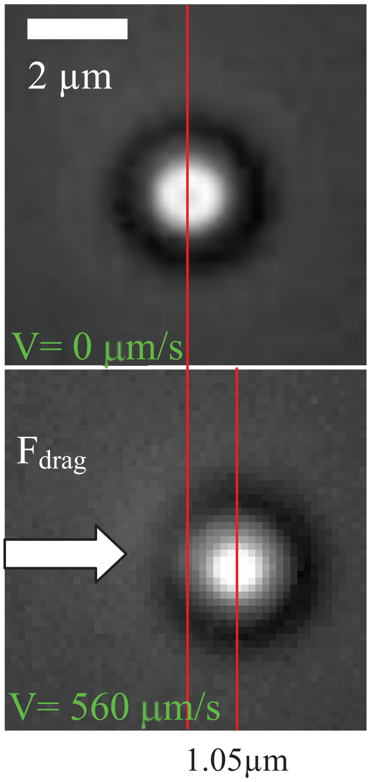

Fig. 3.14: Images showing the displacement of 2.59 μm particle trapped at 30 mW. (Top) Image shows the trapped position at zero velocity and (Bottom) shows the trapped position at 560 $\mu m/s$.

Fig. 3.15 shows the maximum lateral displacement of all the particles. An average value obtained from five measurements at all power levels is shown with the standard deviation. Value of maximum displacement exhibits an asymptotic increase with the particle size. The larger particles showed approximately 0.81 R displacement inside the trap, which is much more than any reported value. Previous investigations on lateral escape position using single beam optical trap showed that a particle escapes out of the optical trap when the lateral displacement exceeds 0.5-0.61 R [156]. Researchers attributed this to the axial movement of the particles while a lateral force is applied. In order to increase the axial efficiency, the refractive index of immersion oil is tuned to compensate for the spherical aberration and thereby enhance the axial stability. Although extent of the lateral particle movement is increased to 0.74 R, the corresponding potential is observed to be non-harmonic [157]. In the present case, it is observed that for the larger particles, the maximum lateral movement can be in the range of 0.81 R, which is much closer to the theoretically predicted maximum lateral

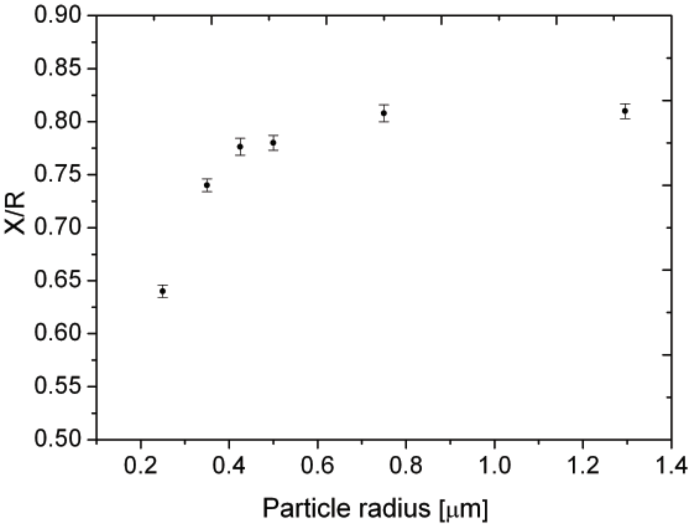

Fig. 3.15: Graph showing the particle displacement inside the trap as a function of the particle radius. Y axis represents the ratio of the actual displacement to the particle diameter.

displacement (0.9 R) of the particle in an optical trap. This observation can be explained on the basis of the nature of the optical potential created by the optical trap.

The nature of the potential well of the optical trap was determined by measuring the lateral displacement of the particle at each applied velocity [126]. The fluid velocity was varied step by step and the corresponding particle position was recorded using Andor camera. The displacement from the equilibrium position is measured as discussed in the sec: 3.8.3. Fig. 3.16 (Left) shows there is a linear relation between the applied velocity and the particle displacement. From this results, it is attributed that the potential well created by the optical trap is harmonic in nature for all the particles examined.

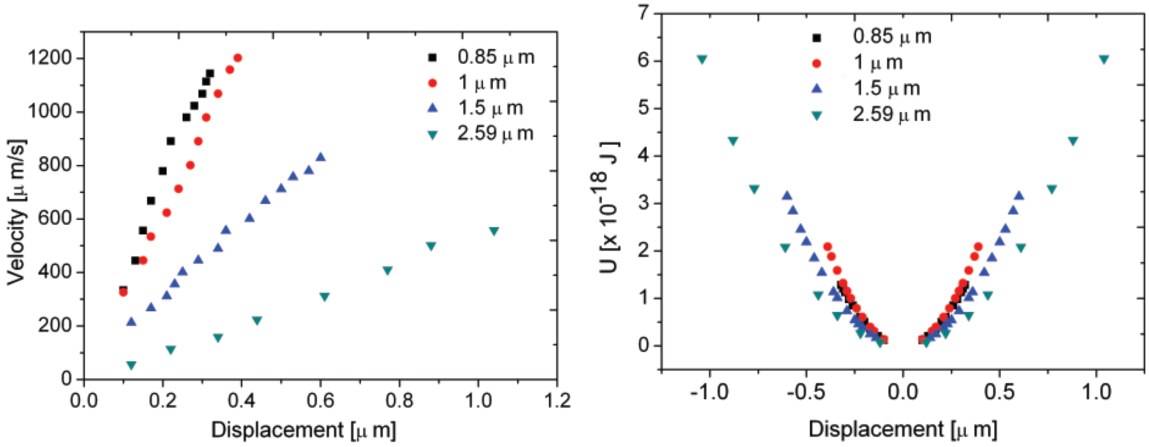

Fig. 3.16: (Left) Graph showing the particle displacement and (Right) the corresponding potential energy of the particles at 30 mW.

By knowing the escape force and the corresponding particle position, we can compute the potential energy of a harmonic potential using the equation:

$$U(x) = \frac{1}{2}kx^2 \tag{3.38}$$

Fig. 3.16 (Right) shows the potential well for the particles trapped at 30 mW. It is obvious that the potential well created by the optical trap is parabolic in nature as reported [126]. The similar behavior was observed at different power levels too. The increased lateral displacement of the particle in harmonic potential can be understood in terms of high degree of localization of the trapping volume with the employment of shorter wavelength. The escape trajectory studied under a transverse fluid flow predicted that by confining the particle in the focal plane, the lateral displacement can be extended up to 0.97 R [156]. Additionally, the high degree of localization restricts the range of axial extent to which the particle can be moved while remaining inside the trap [144]. A recent theoretical simulation on the trapping focal volume and particle size showed that when the particle overfills the axial dimensions of the trapping volume, the movement of the particle along that direction is limited and result in a more symmetrical trap [145]. In such a situation, under an external transverse flow the particle is subjected to mainly lateral movement only. In the present case, the axial extent of the focal trapping volume is about 1.4 μm (calculated using eq. 3.34). As a result, the larger particles move predominantly in the lateral direction and maximum lateral displacement approaches a value close to theoretically predicted maximum value.

The behavior of the smaller particles in the range from 0.5 to 1 μm diameter are analyzed in the next chapter, where we compare the results obtained here to that of trapped in a conventional sample chamber.

3.8.4 Effect of particle size on trapping stiffness

From the values of the escape force and the corresponding lateral displacement, we can compute the stiffness of the trap in that direction. Optical trapping stiffness is given by the ratio of escape force to the corresponding displacement. Additionally, stiffness can be calculated by taking the slope of force versus displacement graph. Fig. 3.17 shows the dependence of optical trapping stiffness as a function of particle radius measured for various incident power. An average value of five measurements is shown with the standard deviation as error bar. From the graph, it is clear that, at all power levels the particles in the range from 0.7 to 1 μm showed higher trapping stiffness than the other particles.

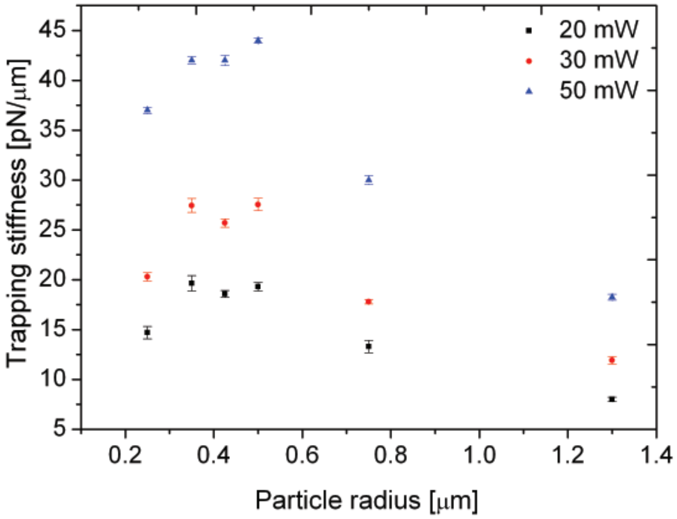

Fig. 3.17: Graph showing the trapping stiffness as a function of particle radius at three different laser powers.

To understand the physical mechanism behind this observation, we compared the experimental results with the theoretical model predicted by Tlusty et al. [148]. It is reported that particles of intermediate size with a small refractive index as used here, the phase difference across the focal plane created by a highly localized beam can be neglected [27, 148]. Hence, the contribution of interference effect is not considered.

The localized electromagnetic field near the focal point is given by a three dimensional Gaussian beam of axial symmetry having an intensity profile:

$$I(r,z)=I_0 exp(-\frac{r^2}{2\omega_A^2}-\frac{z^2}{2\omega_A^2\epsilon^2}) \tag{3.39}$$

Here ω_A and $\omega_A\epsilon$ are the beam waist radii in the transverse and the axial direction respectively, where ϵ is the eccentricity. I_0 is the intensity at the focal point ($r=z=0$). The corresponding expression for transverse stiffness is given by:

$$k_r=\alpha I_0\omega\frac{2\pi\epsilon^3}{\xi^3}[\sqrt{\pi/2}((\frac{\xi a}{\epsilon})^2-1)e^{-\frac{a^2}{2}}erf(\frac{\xi a}{\sqrt{2}\epsilon})+(\frac{\xi a}{\epsilon})e^{-\frac{a^2}{2\epsilon^2}}] \tag{3.40}$$

while the axial stiffness is:

$$k_z=\alpha I_0\omega\frac{4\pi\epsilon}{\xi^3}[\sqrt{\pi/2}e^{-\frac{a^2}{2}}erf(\frac{\xi a}{\sqrt{2}\epsilon})-(\frac{\xi a}{\epsilon})e^{-\frac{a^2}{2\epsilon^2}}] \tag{3.41}$$

where $\xi=\sqrt{1-\epsilon^2}$, a=R/ω_A and α=$\frac{n_p^2}{n_m^2}-1$.
Fig. 3.18 shows the theoretical k_r (solid line) along with the experimentally measured stiffness at 30 mW (symbols) for all the particles. The theoretical curve was plotted for an eccentricity, $\epsilon=4$.

It is seen that the optical trap stiffness agrees well with the experimental values except for the larger particle. The disagreement of larger particle is explained on the basis of the gravitational force acting on the trapped particle [148]. From the fig. 3.18, it is observed that the maximum value of the trap stiffness occurs at $a\approx 2$, i.e., when the particle diameter nearly equals twice the lateral beam waist. These results are consistent with the earlier reported studies showing that for intermediate particle size range, the optical trap stiffness exhibit a nonlinear dependence [158]. It is observed that the particles having a volume of the order of the trapping volume, exhibit maximum value for the optical trap stiffness. In comparison to the commonly employed IR lasers, optical trapping using 442 nm laser results in a smaller trapping volume. This small trapping volume causes high degree of localization of the trapped particle and high gradient force.

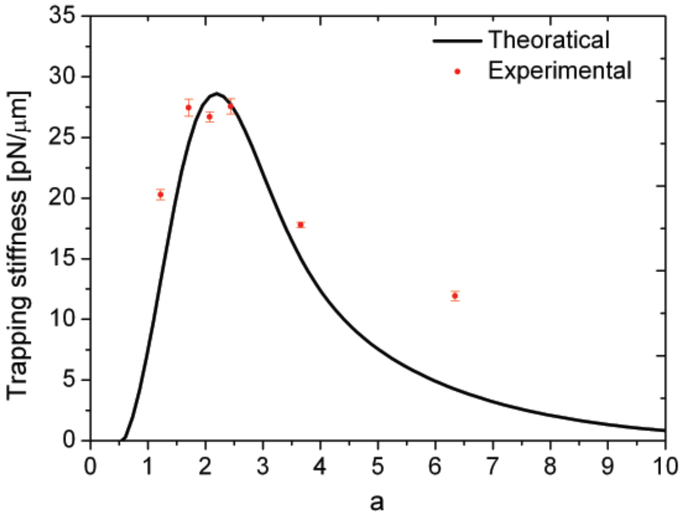

Fig. 3.18: Graph showing the comparison between experimental stiffness with the theoretical fitted value.

In the present case, the focal trapping volume is approximately 1.3 x 10^{-19} m^3 which fall into the range of particle volumes for 0.7, 0.85, and 1 μm particles (1.8 x 10^{-19} m^3, 3.2 x 10^{-19} m^3, and 5.2 x 10^{-19} m^3, respectively). When the particle volume (6 x 10^{-20} m^3 , for 0.5 μm) is smaller than the trapping volume, the particle can move within the trap which results in a less stiff trap. Moreover, Brownian motion of the smaller particles results in a weaker trap. In the case of large particles, the spot size is smaller than the particle diameter resulting in almost same optical trapping force. However, the maximum lateral movement of the particle in a trap depends upon the particle radius. As a consequence, with the increase in particle size the optical trap stiffness decreases considerably ($1/R$ dependence in Ray optics regime). In the present case, the predicted dependence for particles in the geometric optics regime is not observed, as the particles employed here are still in the intermediate size range.

3.9 Summary

This chapter explains both the theoretical and experimental methods followed on optical trapping inside a microfluidic channel. Dependence of laser power and particle size on optical trapping parameters such as lateral escape force, maximum lateral displacement of the particles inside the trap and trapping stiffness has been performed in detail. The maximum lateral displacement can be achieved close to the theoretically predicted value. Moreover, velocity versus displacement graph shows the constructed optical trap is harmonic in nature. A theoretical analysis of the experimental stiffness shows that the experimental result matches well with the theoretical predictions. To understand the effect of flow profile on trapping parameters, it is necessary to perform optical trapping in a sample chamber where the trapped particle experience uniform velocity profile. Moreover, this chapter considered only the lateral forces acting on the particle. Next chapter describes the dependence of the flow profile and the axial forces acting on the trapped particle.

4 Comparison of trapping force in microfluidic channel with trapping force in sample chamber

4.1 Introduction

Chapter 3 investigated the trapping parameters (escape force, particle displacement and trapping stiffness) under Poiseuille flow where particle experiences a velocity gradient in the axial direction. To understand the influence of flow profile on the trapped particle, optical trapping experiments were performed under the condition where particle experience uniform velocity profile. This chapter reports the trapping of silica particles trapped in a sample chamber and compare the result obtained from trapping under Poiseuille flow.

Fig. 4.1 displays the photograph of the experimental setup employed for trapping experiment. For the details of the trapping optics, reader is referred to sec: 3.7 of this thesis.

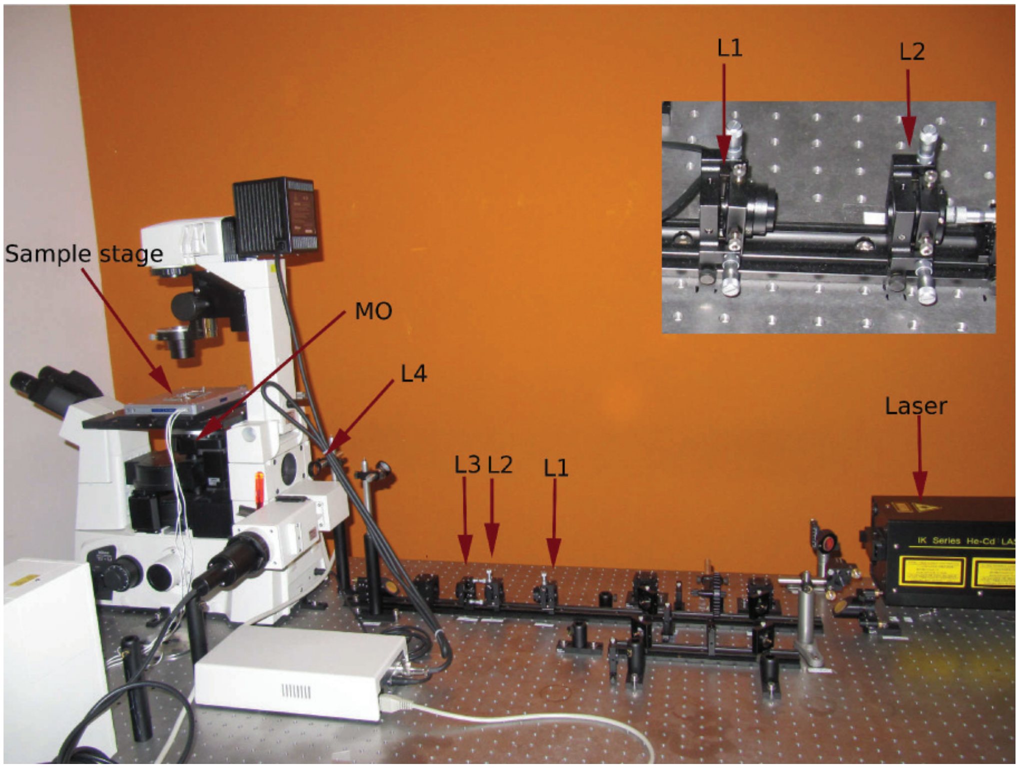

Fig. 4.1: Experimental setup used for optical trapping at 442 nm.

Fabrication of sample chamber

The sample chamber consists of two 175 μm thick cover slips (Menzel-Gläser, Thermo Fisher Scientific, Germany) separated by a 200 μm thick spacer. It contains a rectangular chamber of dimension 1 *cm* x 1 *cm* as shown in fig. 4.2. This well was filled with the particle suspension before fixing the second cover slip on the top. Special care has been taken not to include any air bubbles inside the sample cell.

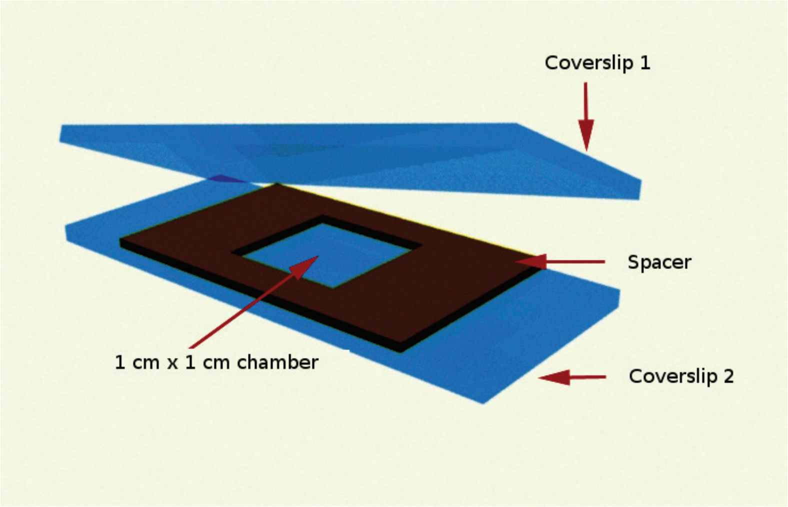

Fig. 4.2: Schematic diagram of the sample chamber used for trapping experiments.

Piezo stage

Piezo stage used for the present study was a capacitive piezo-driven XYZ nanostage (Model Nano-LPQ, Optophase, France). Technical details of the stage is given in table 4.1. Piezo stage was fixed on the Nikon Eclipse microscope (Nikon TE 2000 inverted microscope). Motion of the stage was controlled by Nano-Drive 85 controller using a LabVIEW program.

Axis	Range of motion μm	Resolution nm	Stiffness N/μm
X	75	0.2	1
Y	75	0.2	1
Z	50	0.1	1

Table 4.1: Technical specifications of Nano-LPQ translational stage.

4.3 Escape force- Comparison between 2 methods

Here, the relative motion between the trapped particle and the laser focus is achieved by translating the piezo stage at a fixed velocity. The escape force is determined from the critical velocity at which the particle escape out of the trap [28]. Thus, by knowing the velocity of the stage at which the particle escapes from the trap (ν_p), the maximum trapping force can be calculated using the eq. 3.21. Additionally, trapping of the particle near the wall results in a hydrodynamic coupling between the trapped particle and the chamber wall and consequently influences the drag force experienced by the particle [152]. After incorporating the hydrodynamic coupling effect, equation for the drag force can be written as:

$$F_{escape} = \frac{6\pi\mu R\nu_p}{1 - \frac{9}{16}\frac{R}{l} + \frac{1}{8}(\frac{R}{l})^3 - \frac{45}{256}(\frac{R}{l})^4 - \frac{9}{16}(\frac{R}{l})^5} \tag{4.1}$$

where l is the distance from the bottom wall to the trapping position.

Experimental procedure to determine the escape velocity is as follows. The laser focus at the interface was determined by monitoring the Airy's pattern at the glass-water interface. Then the laser focus was shifted to the desired trapping position (5 μm from the coverslip). A single silica particle was trapped at the laser focus at zero applied velocity, i.e, keeping the piezo stage at rest. Then a linear ramp was applied to the stage, simultaneously the corresponding displacement of the optically trapped particle from the equilibrium position was recorded. By increasing the stage velocity in the X - direction, the particle eventually escapes from the optical trap. This critical velocity was considered for the escape force calculation.

To compare with the previous results (Poiseuille flow method), trapping experiments were performed for particles, ranging in size from 0.5 μm to 2.59 μm at three different power levels (20, 30 and 50 mW). Fig. 4.3 shows the combined result of all the particles examined at three different power levels. An average value obtained from five measurements is shown here and the standard deviation obtained from these measurements are plotted as error bars.

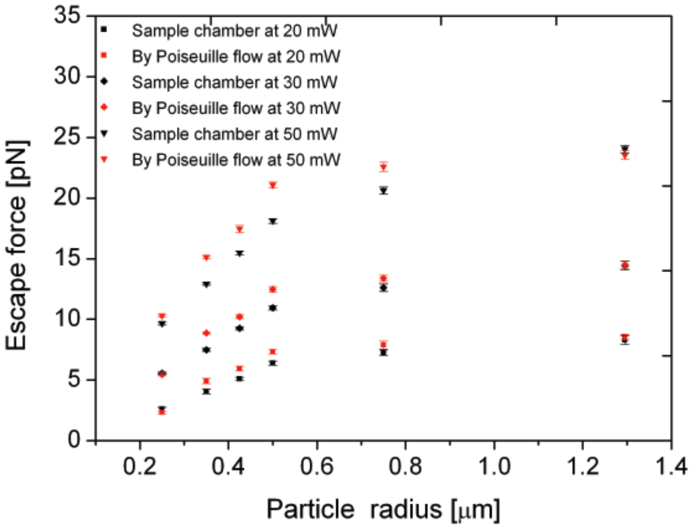

Fig. 4.3: Graph showing the escape force at different power levels for Poiseuille flow (Red symbols) and for sample chamber (Black symbols).

Fig. 4.3 shows a nonlinear increase in the escape force with the particle radius. Earlier studies report that, for Rayleigh regime the maximum trapping force exhibits a R^3 dependence, whereas force is independent of particle size for large particles (Ray optics regime) [152]. However, for the particles of intermediate particle as in the present case, the maximum lateral force exhibits a nonlinear dependence on the particle radius, a crossover from the R^3 dependence to an asymptotic plateau [148]. The linear dependence of optical trap to the input power was ensured by measuring the escape force at different intermediate power levels between 20 and 50 mW. The data plotted in fig. 4.3 also shows that the escape force is higher in the case of Poiseuille flow, for the particles in the range of 0.7 to 1.5 μm. It is reported that, axial motion of the trapped particle influences the their axial stability inside the trap [156]. As a result, the axial equilibrium of the particle in an optical trap is broken before it reaches the maximum lateral displacement. The minimum optical force required for holding a particle axially in an optical trap against gravity and the thermal motion is given by [159]:

$$F_{min} = \frac{n_m P_{min} Q_a}{c} = \frac{4}{3}\pi R^3(\rho_p - \rho_m)g + \frac{k_b T}{R} \tag{4.2}$$

where P_{min} is the minimum power required, Q_a is the axial trapping efficiency, g is acceleration due to gravity, k_b is the Boltzmann constant and T is the temperature. When F_{min} is smaller than the combined effect of gravity and the thermal force, the axial equilibrium of the particle is broken and the particle escapes from the trap. To evaluate the axial stability of the trapped particle, it is necessary to consider the axial forces in both the flow conditions.

4.3.1 Effect of gravitational force

The equilibrium position of a trapped particle depends on the axial forces acting on it. In the present case, axial forces acting on the particle are gravitational force, Saffman lift force and the optical forces. To understand the influence of gravity, it is important to determine the equilibrium position of the trapped particle. This section provides the experimental method to determine the trapping position.

Silica particles having diameter 1 μm was fixed on the bottom surface of a sample chamber containing water, then scanned below and above the focus using a piezo stage with a step size of 40 nm. The objective used for imaging was Nikon TIRF 100X objective. The corresponding images were recorded, and the intensity profile was plotted along the center of the particle (green line on the images) using Nikon NIS elements software. Images and the corresponding intensity profile are shown in fig. 4.4. The scanned images were compared with the image of the particle trapped at 30 mW under similar illumination conditions. From fig. 4.4, it is evident that the image and intensity profile of the trapped particle matches well with the image recorded at 120 nm below the focus.

From fig. 4.4, it is attributed that the trapped particle stays below the focus at zero applied velocity. This situation can be explained as follows. The gradient part of the optical force depends upon Δn, where Δn is the difference between the refractive index of the trapped particle and the surrounding medium, whereas the scattering part depends upon Δn^2 [151]. Normally, the scattering force shifts the trapping position slightly beyond the focal point. A relatively small difference in refractive index (Δn=0.09) in the present case results in a negligible scattering force, and consequently trapping of the silica particles occurs close to the focal point for vanishing flow. Furthermore, the higher density of the silica particle ($\rho_p = 2.2\ g/cm^3$) makes the effect of gravity significant and shifts the trapping position below the focal plane. Additionally, a particle trapped in a parabolic flow profile experiences a velocity gradient that produces a force (Saffman lift force) perpendicular to the flow direction.

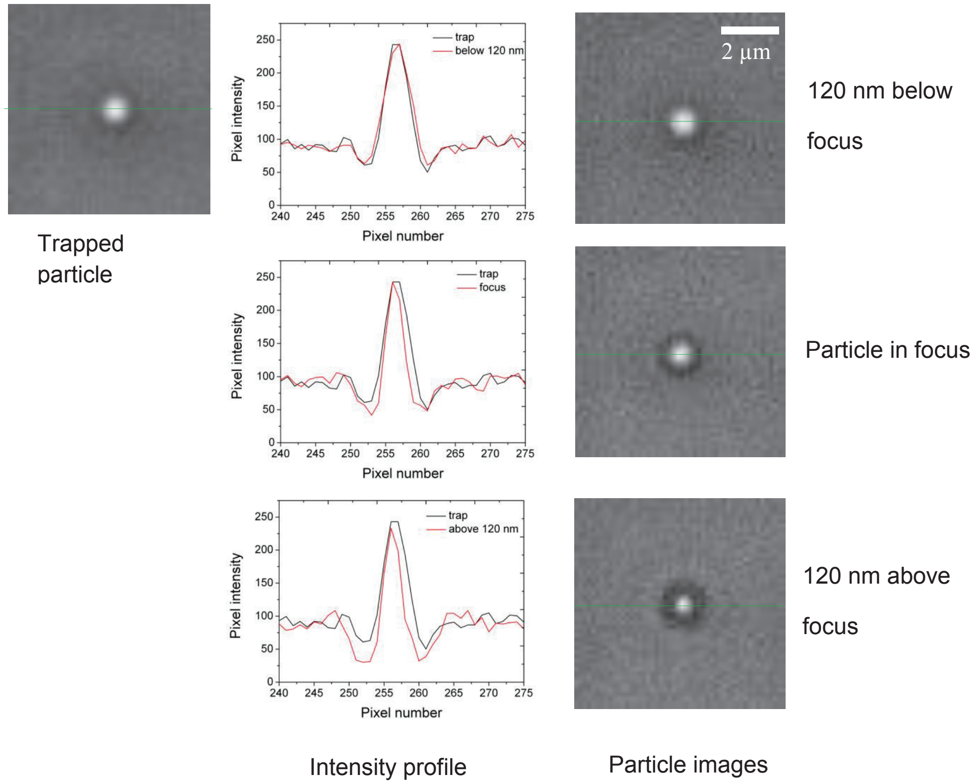

Fig. 4.4: Image analysis showing the particle images and the corresponding intensity profile. Comparing the scanned images and the intensity profile with the trapped image, it shows that the particle is trapped 120 nm below the focal plane.

4.3.2 Effect of lift force

As mentioned in the previous chapter, a particle trapped in a parabolic flow profile experiences a velocity gradient that produces a force (Saffman lift force) perpendicular to the flow direction. The Saffman lift force which opposes the gravitational force and is given by [143]:

$$\mathbf{F}_{saffman} = 6.46\sqrt{\rho_m \mu}(u_x - v)R^2\sqrt{\frac{du_x}{dZ}}\,\hat{\mathbf{e}}_z \tag{4.3}$$

For the particles employed here, the magnitude of the Saffman lift force (evaluated at the flow velocity where the particle escapes from the trap at 30 mW) and the gravitational force are shown in fig.4.5.

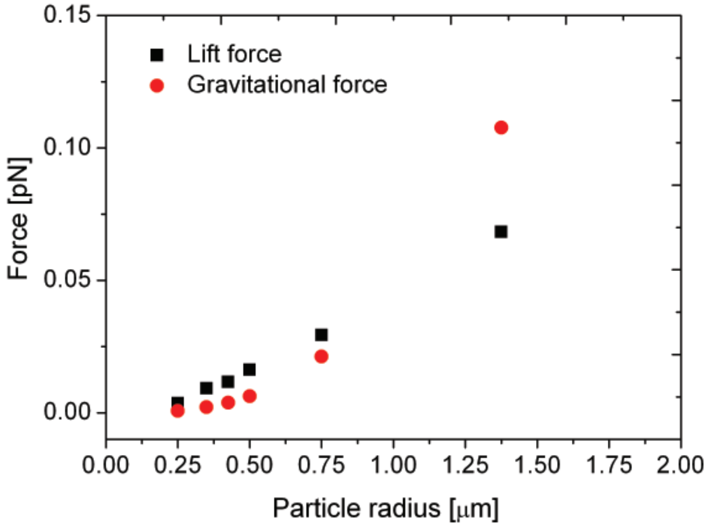

Fig. 4.5: Graph showing the gravitational force acting on the silica particles and the lift force (evaluated at the flow velocity where the particle escapes from the trap at 30 mW).

Fig. 4.5 shows that, except for the largest particle, the Saffman lift force is higher or comparable in magnitude with the gravitational force. As the trapped particle moves away from the equilibrium position, the lateral gradient force decreases that results in an increased axial motion of the particle. In the case of particles trapped below the focus as in the present case, the gravitational force can destabilize the trap before the particle reaches its theoretically predicted maximum displacement. So in effect, this can lead to reduced lateral escape force. Now considering the situation where particle is trapped under Poiseuille flow, the effect of gravitational force is compensated by the lift force. In order to liberate an optically trapped particle along the axial direction in a Poiseuille flow, at the escape position the combined effect of the gravitational force and the thermal force has to be greater than that of the optical trapping force and the Saffman lift force. So an additional contribution of the lift force against gravity keeps the particle close to the higher intensity region which leads to the higher trapping force in the case of Poiseuille flow. Moreover, the reduction in localized temperature at the focal point in a flowing medium decreases the Brownian fluctuations of the particle and thus increases the stability of the optical trap. But in the situation where the particles trapped inside the sample chamber, particles experiences a uniform velocity profile, i.e, there is no lift force present to overcome the effect of gravitational force. So the trapped particles escape at lower applied force. However, for the particles with size 2.59 μm, the escape force and the maximum displacement is similar. This behavior can be explained as follows. A recent study on the trapping focal volume and particle size showed that when the particle overfills the axial dimensions of the trapping volume, the movement of the particle along that direction is limited and result in a more symmetrical trap and increased axial stability [145]. Hence, it is attributed that the axial movement of the 2.59 μm is limited because it exceeds the axial dimension of the trapping volume. Under such an axially stable trapped position, behavior of the particle inside the trap is not influenced by the external axial forces.

4.3.3 Displacement of the particle inside the trap

Influence of flow profile on the trapped particle was further confirmed by studying the displacement of the particle inside the trap in both the flow conditions. For this, the trapping position of the particle at each applied velocity was recorded using CCD camera. Displacement measurements were performed using Nikon NIS software. Initially the particle was trapped at zero applied velocity and the center of the particle was determined using the NIS software. This position was taken as the reference frame for the displacement measurements. An average value of 5 measurements at each laser power as a function of particle radius is shown in fig. 4.6 and the standard deviation was plotted as error bars. Harmonic nature of the optical potential was confirmed by plotting velocity versus particle displacement as shown in fig. 4.7. It was found from fig. 4.6 that, for particles having sizes 0.7 , 0.85 , and 1 μm, the lateral displacement was higher in the case of Poiseuille flow. As mentioned in the earlier section, the maximum lateral displacement in both configurations is limited by breaking of axial equilibrium of the particle. For an optically trapped particle, the maximum optical trapping force is experienced at the vicinity of the focal plane and it decreases away from the focal plane. Thus in the case of a particle trapped in a sample chamber, the particle breaks the axial equilibrium position when

$$F_{min} < [\frac{4}{3}\pi R^3(\rho_p - \rho_m)g + \frac{k_b T}{R}] \tag{4.4}$$

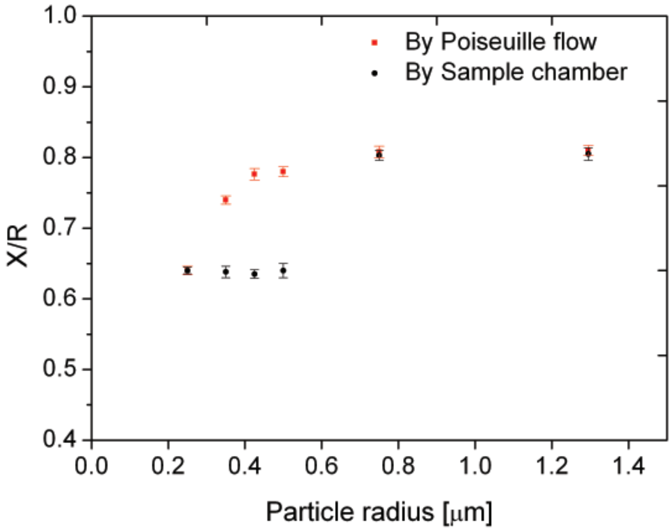

Fig. 4.6: Graph showing the particle displacement inside the trap in both the flow conditions, by Poiseuille flow (Red symbols) and by piezo stage (Black symbols).

However, the force required to retain an optically trapped particle along the axial direction in a Poiseuille flow is less by an amount equal to the Saffman lift force is:

$$F_{min} < [\frac{4}{3}\pi R^3(\rho_p - \rho_m)g + \frac{k_b T}{R} - F_{saffman}] \tag{4.5}$$

In the case of larger particle, the Saffman lift force is negligible in comparison with the gravitational force, so the particle shows similar displacement in both the cases.

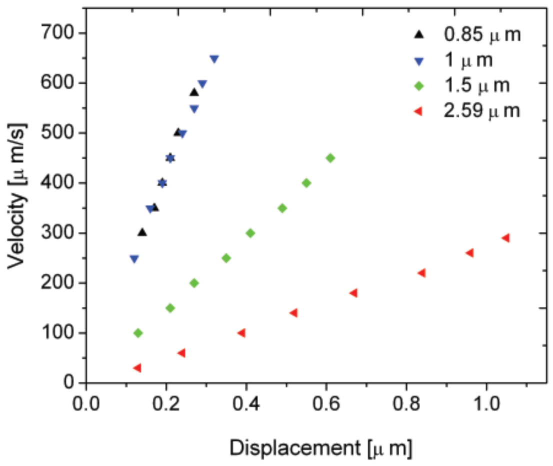

Fig. 4.7: velocity versus displacement graph at 20 mW.

4.3.4 Comparison of trapping stiffness

Fig. 4.8 shows the trapping stiffness of all the particles at three different power levels. The lateral stiffness of the optical trap is found to follow similar behavior in both flow configurations. In both the flow conditions, particles with size in the range 0.7 - 1 μm showed higher trapping stiffness than other particles. This behavior is theoretically explained in sec: 3.8.4 of this thesis.

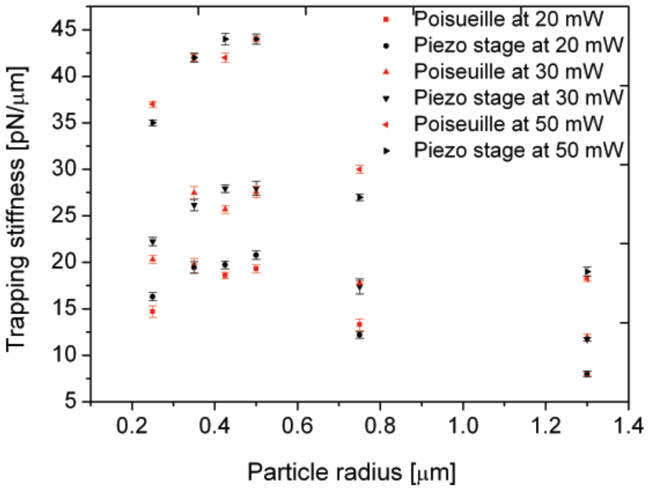

Fig. 4.8: Stiffness of the trapped particle in both the flow conditions, by Poiseuille flow (Red symbols) and by piezo stage(Black symbols).

4.4 Summary

This work compares the size dependent behavior of the optically trapped silica particles in a microfluidic channel under a pressure driven flow to the corresponding particles trapped in a sample chamber. It was found that the Saffman lift force generated due to parabolic velocity profile in the case of Poiseuille flow influences the axial stability of smaller particles and increases the maximum lateral escape force. The lateral stiffness of the optical trap is found to follow similar behavior in both flow configurations. The maximum lateral displacement of the particle inside an optical trap approaches the theoretically predicted maximum value when the particle was confined in a small volume with the employment of lower wavelength for trapping. From the present study, it is concluded that,

(1) The flow profile has to be taken into account especially when the particle size is smaller than axial extent of the trapping laser beam
(2) The theoretically predicted maximum lateral displacement can be experimentally observed using escape force method by confining particles to smaller volume with the usage of appropriate wavelength.

5 Transport processes at fluid-fluid interface

5.1 Introduction

This chapter is divided into two parts: Part I provides an introduction to the basic theory behind the novel particle manipulation technique presented in this work. This section covers the basics of interfaces and interfacial flows generated by the surface tension gradient (Marangoni flow). Part II of this chapter gives a brief introduction to photoswitchable surfactants with an emphasis on the properties of the surfactant used in this work.

5.2 Interfaces and interfacial transport phenomena

Two immiscible fluids are separated by a boundary, so-called interface or surface. Interfacial phenomena such as adsorption, transport processes across the interface and wetting are relevant in day to day life to industrial applications. An interface is not an infinitesimal sharp boundary in the direction of its normal, but it has a certain thickness [160]. Depending on the nature of the phases, the interface can be fluid-fluid or solid-fluid. Fluid-fluid interface can be further divided into two: liquid-gas interface or liquid-liquid interface. An interface is commonly called as surface when one of the phases is vacuum or gas. The most relevant parameter that determines the property of an interface is its interfacial energy or interfacial tension.

5.2.1 Surface tension

Surface tension is the property of liquids arising from the unbalanced molecular cohesive forces near the free surface [161]. Surface tension is a measure of the energy shortfall per unit surface area. If the cohesion energy per molecule is denoted by U and $\boldsymbol{a}$ denotes the molecular dimension, then the surface tension is of the order of $\sigma \approx U/2\mathbf{a}^2$ [161]. This relation shows that surface tension is dominant for liquids with large cohesive energy and small molecular area. This is why mercury has a large surface tension compared to that of organic liquids. Surface tension is the reason why small liquid drops tend to minimize the surface area by forming spherical shape.

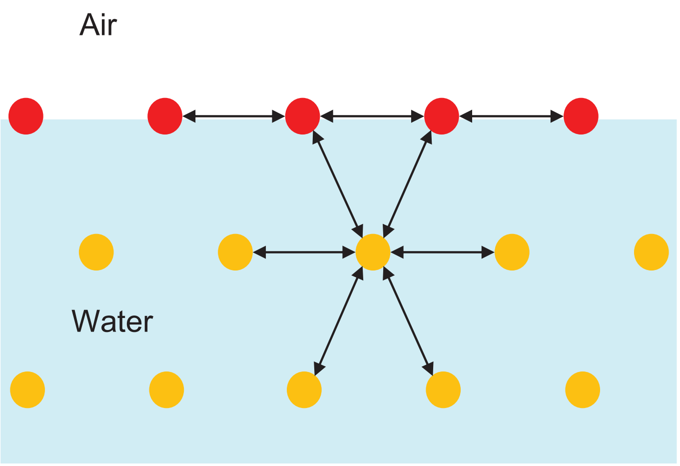

Fig. 5.1: Schematic illustration of the molecular basis of the surface tension.

Consider the case of water taken in a flat vessel where the top surface is open. Each water molecule is attracted to its neighboring molecules by a force which may be due to van der Waals force or hydrogen bonds [162]. In the bulk, the net force acting on the molecule is zero because a molecule is attracted equally in every direction, i.e., molecules are in a uniform force field. In the case of a molecule at the free surface, the net attraction from the bulk liquid is much higher than that from the gas phase, resulting in an energetically unfavorable state. This leads to an internal pressure and force making the surface contract to its minimum surface area. Fig. 5.1 schematically represents the force acting on the molecules both in the bulk (yellow spheres) and at the interface (red spheres). The same reasoning applies to the interface between two immiscible liquids, for example water and oil. Molecules near water-oil interface are in an energetically unfavorable situation due to the unequal attractive forces from the two phases. In this case, the net pressure on the molecule is called interfacial tension instead of surface tension. Interfacial tension is the reason behind the natural phenomena like bubble formation and separation of oil in water. The surface tension of water-air system is about 72 mN/m at room temperature, and for most of the water-oil interface, it is about 50 mN/m. Surface tension is a vital parameter whose effect increases as the length scale of the system decreases [75]. So surface tension plays a pivotal role in microfluidics where surface area to volume of a fluid element is large.

5.2.2 Microfluidic governing equations

Microfluidic flows are characterized by being laminar [75]. The Laminar flow of an incompressible Newtonian fluid of uniform density ρ and viscosity μ is governed by the Navier - Stokes equations (conservation of momentum) and the equation of continuity (conservation of mass) [75, 163]. The time dependent Navier - Stokes equation is expressed as:

$$\rho\left(\frac{\partial \mathbf{u}}{\partial t}+(\mathbf{u}\cdot\nabla)\mathbf{u}\right)=-\nabla p+\mu\nabla^2\mathbf{u}+\mathbf{F}_b \tag{5.1}$$

where $\boldsymbol{u}$ is the fluid velocity, p is the pressure and $\mathbf{F}_b$ is the body force. For a fluid moving with a velocity $\boldsymbol{u}$, the relevance of the inertial force and the viscous force is given by a dimensionless quantity called Reynolds number [75]. The Reynolds number is given by:

$$R_e=\rho u D_h/\mu \tag{5.2}$$

where D_h is a characteristic dimension of the system, for e.g., the diameter of a pipe or the thickness of a liquid film. For a microfluidic system, this length is so small that the flow has low Reynolds number. This means, the viscous force dominates over the inertial force. In this limit, the pressure force is balanced solely by the viscous force. Then the Navier-Stokes equation reduces to the Stokes equations:

$$\rho\frac{\partial \mathbf{u}}{\partial t}=-\nabla p+\mu\nabla^2\mathbf{u}+\mathbf{F}_b \tag{5.3}$$

The continuity equation for an incompressible liquid (ρ is constant) is written as:

$$\nabla\cdot\mathbf{u}=0 \tag{5.4}$$

Additionally, boundary conditions need to be specified at the fluid interfaces, e.g., no-slip at the solid walls and continuity of velocity and stresses at the fluid-fluid interfaces. Consider a liquid film of height h and width w as shown in fig. 5.2.

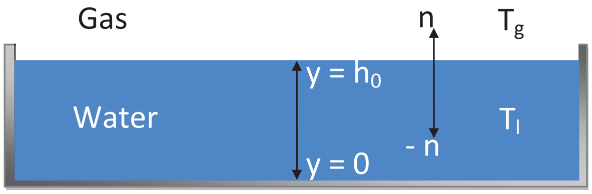

Fig. 5.2: Schematic representation of a liquid film having height h_0 and width w.

The no-slip boundary condition at the bottom wall ($y = 0$) is given by:

$$\mathbf{u} = 0 \tag{5.5}$$

At the free surface with $y = h_0$, there arises two stress boundary conditions, namely the normal stress balance condition and the tangential stress balance condition. At the interface, the projected stress tensor is balanced by the surface tension forces. In general, we can write the stress balance condition at the liquid-gas interface as [75, 163]:

$$\mathbf{n}\cdot \overset{\leftrightarrow}{\mathbf{T}}_g - \mathbf{n}\cdot \overset{\leftrightarrow}{\mathbf{T}}_l = \sigma \mathbf{n}(\nabla \cdot \mathbf{n}) - \nabla_s \sigma \tag{5.6}$$

where $\mathbf{n}\cdot \overset{\leftrightarrow}{\mathbf{T}}_g$ and $\mathbf{n}\cdot \overset{\leftrightarrow}{\mathbf{T}}_l$ are the stresses exerted by the gas on the liquid and the liquid on the gas respectively. The first term on the right hand side of the eq. 5.6 represents the normal curvature per unit area and the second term corresponds to the tangential stress associated with the gradient in surface tension. ∇_s denotes the surface gradient operator defined as $\nabla_s = \nabla - \mathbf{n}(\nabla \cdot \mathbf{n})$.

The normal stress at the free surface is balanced by the curvature force associated with the surface tension which can be represented as (neglecting the viscous stress from the gas phase) [75]:

$$\mathbf{n}\cdot \overset{\leftrightarrow}{\mathbf{T}}_l \cdot \mathbf{n} = -\sigma(\nabla \cdot \mathbf{n}) \tag{5.7}$$

where $\mathbf{n}$ is the unit normal to the surface and $\overset{\leftrightarrow}{\mathbf{T}}_l$ is the stress tensor. Stress tensor can be written as the sum of pressure and viscous contributions [163]:

$$\overset{\leftrightarrow}{\mathbf{T}}_l = -p \overset{\leftrightarrow}{\mathbf{I}} + 2\mu \overset{\leftrightarrow}{\mathbf{E}} \tag{5.8}$$

where $\overleftrightarrow{\mathbf{E}}$ is the deviatoric stress tensor:

$$\overleftrightarrow{\mathbf{E}} = \frac{1}{2}[\nabla \mathbf{u} + (\nabla \mathbf{u})^T] \tag{5.9}$$

and $\overleftrightarrow{\mathbf{I}}$ is the identity matrix.

The tangential stress arises from two sources: the component of the viscus stress tangent to the interface and the tangential stress caused by a gradient in surface tension [75]. The tangential viscous stress is discontinuous if the surface tension is not uniform along the interface. The tangential stress balance condition at the free surface can be written as (neglecting the viscous stress from the gas phase) [163]:

$$\mathbf{n} \cdot \overleftrightarrow{\mathbf{T}}_l \cdot \mathbf{t} = \nabla_s \sigma \cdot \mathbf{t} \tag{5.10}$$

where **t** is the unit tangent to the interface. The tangential component of the hydrodynamic stress at the surface must balance the tangential stress associated with the gradient in surface tension. This results in a hydrodynamic flow known as Marangoni flow [82].

5.2.3 Marangoni flow

Molecules in a region of higher surface tension bind the nearby molecules stronger than those in a lower surface tension region. As a result, the molecules are attracted towards the higher surface tension region. Presence of a gradient in surface tension on a fluid surface creates a hydrodynamic flow from a lower surface tension region to a higher surface tension region. This effect is known as Marangoni effect, named after the Italian physicist Carlo Giuseppe Matteo Marangoni (1840-1925) [82]. Fig. 5.3 schematically represents this phenomenon. The Marangoni effect can occur in both single- and multi-component systems [162]. The rate of this hydrodynamic flow depends on the magnitude of surface tension gradient and the liquid properties.

The surface tension of a system depends on concentration and temperature at the liquid surface [82, 164]. So the gradient in surface tension can be developed by altering any of these parameters. If the Marangoni effect is generated due to the concentration gradient, the effect is called Solutal Marangoni effect, and if the flow arises due to the temperature gradient, it is called thermal Marangoni effect [165, 166]. Solu-

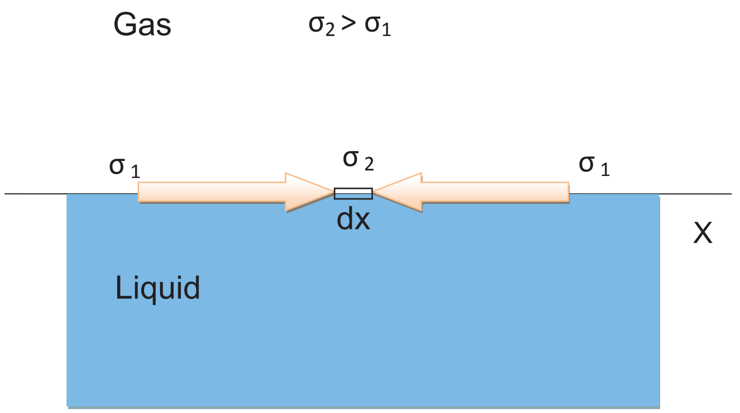

Fig. 5.3: Marangoni flow at the liquid-gas interface

tal Marangoni flow can be developed by the use of surface active materials [10] and chemical reactions [167]. The thermal Marangoni flow can be generated by locally heating the liquid film or substrate [168]. This type of flow can be seen in pure liquids too. Since the surface tension of majority of liquids decrease with the temperature, the induced flow directs away from the hot region [165]. In multi-component systems, a gradient in surface tension arises due to the adsorption related phenomena or due to different evaporation rates of the system [162].

Tears of wine on a glass surface is a typical example for solutal Marangoni effect [169]. This phenomena is qualitatively explained by James Thomson (1822-1892) [170]. Wine is a mixture of water and alcohol. Alcohol has a lower surface tension than that of water. At the glass surface, due to the capillary forces, wine climbs upward to form a thin liquid film. Alcohol is more volatile than water which results in increased evaporation of the alcohol. As the content of the alcohol decreases, the surface tension of the film increases. So more molecules get attracted towards this region. This process continues until the drop falls down due to the gravity which appears as tears of wine. This shows that Marangoni effect is able to drive liquids along the interface.

In short, variation in surface tension at the free surface cause imbalance in shear stress, which results in the fluid motion. Now consider the stress balance condition along the x-direction (neglecting the tangential stress from the air), the force balance condition at $y = h_0$ becomes [163]:

$$\mu \frac{du}{dy} = \frac{d\sigma}{dx} \tag{5.11}$$

where u is the velocity at the free surface.

In the limit of low surfactant concentration and small temperature variation, the surface tension σ of a liquid surface as the function of both the temperature (T) and the surface excess concentration (Γ) can be expressed as a linear relation [171]:

$$\sigma = \sigma_0 - \gamma_T (T - T_0) - \gamma_\Gamma (\Gamma - \Gamma_0) \tag{5.12}$$

where σ_0 is the surface tension of the pure solvent. Surface excess concentration gives the number of solute molecules present at the interface per unit area. $\gamma_T = -\partial \sigma / \partial T$ is the thermal expansion coefficient of the material which gives the change in cohesive force with the temperature. For most liquids, surface tension vanishes at the critical point which indicates that the cohesive force between the molecules in the liquid decreases with increasing in temperature. γ_T for water at room temperature is about 1.5 x 10^{-4} N/mK [163]. $\gamma_\Gamma = -\partial \sigma / \partial \Gamma$ is the solutal expansion coefficient which can be either negative or positive.

Under isothermal condition, the surface tension of a system can be altered by changing the concentration of the system using surfactants. In general, surfactants have the tendency to adsorb to the interface, thus reducing the interfacial tension. The resultant interfacial tension depends on the chemical composition and the concentration of the surfactant [160]. Relation between the surface tension and the surfactant concentration can be expressed as [163]:

$$\sigma = \sigma_0 - \gamma_\Gamma (\Gamma - \Gamma_0) \tag{5.13}$$

Let us consider a small element of length dx along the interface as shown in fig. 5.3, the gradient in surface tension is expressed in terms of gradient in concentration as:

$$\frac{d\sigma}{dx} = \frac{d\sigma}{d\Gamma}\frac{d\Gamma}{dx} \tag{5.14}$$

Combining eq: 5.13 and eq: 5.14, we obtain:

$$\frac{d\sigma}{dx} = -\gamma_\Gamma \frac{d\Gamma}{dx} \tag{5.15}$$

Equating with the stress balance condition to obtain:

$$\frac{du}{dy} = \frac{-\gamma_\Gamma}{\mu}\frac{d\Gamma}{dx} \tag{5.16}$$

For a horizontal surface and zero pressure jump across the interface, the horizontal velocity field at $y = h_0$ is expressed as [172]:

$$u = \frac{-\gamma_\Gamma}{\mu}\frac{d\Gamma}{dx}h_0 \tag{5.17}$$

This assumes $\nabla p = 0$, i.e, no back flow. The direction of the flow depends on the nature of γ_Γ, that can be either positive or negative. The strength of the solutal Marangoni flow is characterized by a dimensionless number called solutal Marangoni number which can be expressed as [173]:

$$Ma_\Gamma = \frac{\gamma_\Gamma h_0 \Delta\Gamma}{\mu D_s} \tag{5.18}$$

where $\Delta\Gamma$ is the difference in concentration and D_s is the molecular diffusivity of the surface active material.

The present work focuses on light-induced solutal Marangoni flow. In this context, the following section of this chapter outline the basic properties of the surfactants with an emphasis on the photosurfactant material used in the present study.

5.3 Photoresponsive surfactants

A surfactant is a chemical compound which alters the interfacial tension between two immiscible phases by adsorbing at the interface [160]. This change in interfacial tension depends directly on the replacement of the pure solvent molecules by the surfactant molecule. The reduction of the surface tension depends on the excess concentration of the surfactant molecule at the interface which is given by Gibbs adsorption equation [174]:

$$d\sigma = -\sum \Gamma_i d\mu_i \tag{5.19}$$

where $d\sigma$ is the change in surface tension of the solvent, Γ_i is the surface excess concentration of the surfactant molecule and $d\mu_i$ is the change in chemical potential of the system.

Surfactant finds numerous applications in the field of petroleum processing, life sciences, painting, health and food industry [174]. Applications also include modification of wettability of a substrate, stabilization of dispersion (foams or emulsions) and creation of interfacial flows [160,174,175]. Surfactants are amphiphilic molecules, which show affinity for both polar and non-polar groups [174, 175]. The polar group is typically aligned in contact with the aqueous phase while the non-polar phase stretches out into the other phase. Polar interaction is stronger than non-polar interaction, so the surfactant molecule form a bulky polar head and a stretched non-polar tail. For an air-water interface, the hydrophobic part of the surfactant orients towards the air phase so as to minimize contact with the water phase and the hydrophilic portion orients in contact with the water molecules which leads to the decrease in free energy of the whole system [160]. This situation is schematically represented in fig. 5.4.

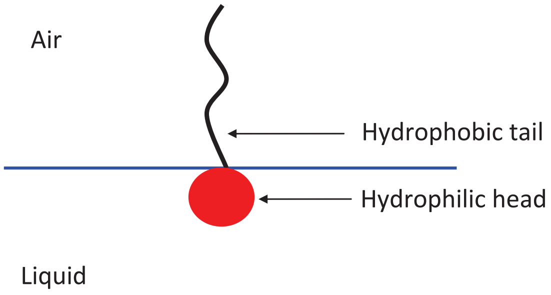

Fig. 5.4: Surfactant molecule at the interface.

Surfactants are generally classified on the basis of the ionic character of their hydrophilic group. Anionic surfactants have a negative charge (due to the presence of carboxyl, sulfonate or sulfate groups), cationic surfactants have a positive charge (e.g., quaternary ammonium halides), nonionic surfactants bear no charge but derive their water solubility from highly polar groups such as polyoxyethylene or polyol groups and zwitter ionic surfactants have both negative and positive charge (due to the presence of sulfobetaines) [162].

For a freshly prepared solution, the surface tension of the solution containing surfactant will be close to that of the pure solvent. Surfactant molecules need to diffuse, adsorb and orient at the interface [176]. This means, the reduction in surface tension is not instantaneous. Adsorption continues until the surface reaches at its equilibrium surface tension. At equilibrium state, the adsorption rate and the desorption rate are equal [162]. The time required for reaching the equilibrium surface tension depends on the nature of the surfactant, their concentration and temperature. This time scale can vary from some milliseconds to many days [177].

In solution, surfactants exhibit a tendency to self associate to form micelles [178]. The hydrophobic part of the surfactant is responsible for both the adsorption at the interface and the micelles formation in the solution. Fig. 5.5 schematically represents the mechanism of adsorption, desorption and micelle formation.

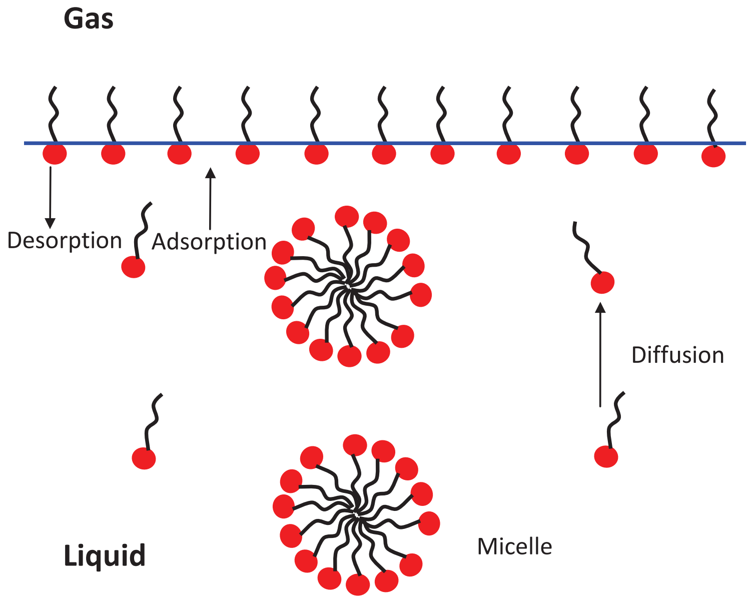

Fig. 5.5: Adsorption and desorption mechanism in micellar solutions.

Aggregate formation happens when the surfactant concentration is above a particular concentration called critical micellar concentration (CMC) [160]. Above the CMC, the surface tension of the solution does not change but remains constant as the interface is saturated with the surfactant molecules. Micelles are formed in such a way that the hydrophilic part of the surfactant is in contact with the surrounding liquid. The shape of the aggregate depends on the temperature, surfactant concentration or any other additives in the solution. The shape can be spherical, rod-like, worm-like or lamellar sheets [175]. Below the CMC, the surfactants exist as unassociated molecules. The presence of micelles changes the properties of the solvent such electrical conductivity and light scattering [162].

Once the saturation state is achieved, an interface hosting a monolayer of the surfactants exhibit uniform surface tension all over the interface [179]. To generate an interfacial flow based on solutal Marangoni effect, one has to alter the surface tension locally. This can be achieved by stretching the film, evaporation or by chemical reaction. Another possibility is the use of photosensitive surfactants.

Photosensitive surfactants are capable of changing interfacial properties on irradiation with light. This offers a non-contact manipulation of interfacial properties. Photoresponsive surfactants found numerous applications in microfluidics and biological sciences [180]. Photocontrol offers high spatial and temporal resolutions. Photoresponsive surfactant contains a photochromic functional unit such as azobenzene [181], stilbene or spiropyran [182] in their hydrophobic tail. Both the azobenzene and spyropyran exhibits reversible structural change under UV - Visbile irradiation. UV illumination induces a conformational change that changes the interfacial and self-assembly properties of the photosurfactant [91]. Such a photoactive molecule has numerous applications, ranging from life science [180] to interfacial fluid mechanics [9, 10]. A few to mention are the creation of a reversible wettabilty gradient over a solid surface [9] or an interfacial-tension gradient at a liquid-liquid interface [10] to transport millimeter-sized droplets.

The present work adopts photoswitchable surfactant incorporated with an azobenzene molecule for generating light-induced Marangoni flow that is capable of trapping and manipulation of particles adsorbed to the gas-liquid interface. Interfacial and bulk properties of the surfactant are controlled by the photoswitching of the azobenzene group. Owing to its clean photochemistry, azobenzene is the most popular candidate among the light-responsive molecules [112, 183].

Azobenzene molecule is characterized by the azo bond (-N=N-) that bridges two phenyl groups. The absorption of light anywhere within the broad *trans* absorption band will elicit photochemical isomerization to the *cis* state as shown in fig. 5.6.

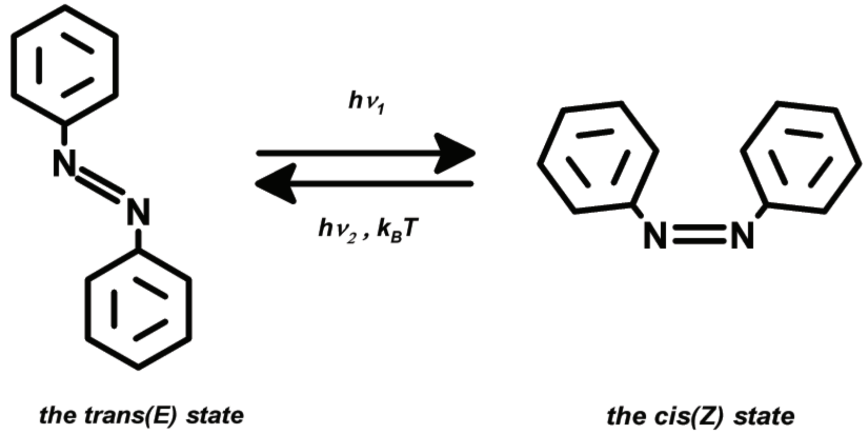

Fig. 5.6: Photoswitching of azobenzene ($h\nu_1 > h\nu_2$).

The reverse transition from the *cis* to the *trans* form can happen via two routes, either via irradiation with the appropriate wavelength or via thermal relaxation. In general, the thermal relaxation path is slow and the rate of reverse switching depends upon the substetuent group in the phenyl ring [112]. In order to explain the photoisomerization of the azobenzene molecule, two different pathways have been proposed: a twisting around the N=N double bond (rotation mechanism) and planar variation of the one of the C-N-N angles (inversion mechanism) [184]. Photoisomerization also induces a change of the molecular size. The conversion from the *tans* to the *cis* state reduces the distance between the ends of the moiety from 0.99 nm in the *trans* state to 0.55 nm in the *cis* state [112]. The steady-state composition of a bulk azobenzene sample under irradiation with an appropriate wavelength depends upon the competition between photoisomerization and thermal relaxation back into the *trans* state. At room temperature, the *trans* state is thermodynamically favored over the *cis* state by an energy shift of 50 kJ/mol. The excitation energy for the photo-excited state is 200 kJ/mol [185]. Photoisomerization happens at a time scale of picoseconds [184]. The steady-state composition as well as the photoisomerization rate of an azobenzene sample depends upon the irradiation intensity, wavelength, temperature, as well as the composition of the host matrix [181].

Several photoswitchable surfactants which exhibits switchable surface tension can be found in the literature, but the difference in saturated surface tension between the *trans* and the *cis* state is very small [186, 187]. An exemption is the work by Shang et al., who reported a new class of photosurfactant material containing azobenzene with large surface tension difference between the *trans* saturated state and the *cis* saturated state [181]. Among the class of compounds studied in ref. [181], a molecule abbreviated as $C_4AzoOC_4E_2$ (diethyleneglycol mono(4',4-butyloxy,butyl-azobenzene)) which exhibits a surface tension difference of more than 10 mN/m is used for the present work.

5.3.1 Properties of $C_4AzoOC_4E_2$ surfactant

$C_4AzoOC_4E_2$ is a nonionic, water soluble surfactant consists of a polar di(ethylene oxide) head group attached to an alkyl spacer of four methylene groups [181]. The hydrophobic tail of the surfactant is linked with a photoswitchable azobenzene moiety. Both the azobenzene and the ether group play important roles in the control of chemical structure of the photosurfactant and hence the surface tension. The photoswitching behavior of the surfactant is controlled by the photochromic azobenzene molecule incorporated into the hydrophobic tail of the surfactant. The photosurfactant exists in two isomeric states, a *trans* and a *cis* state. The *trans* state is the thermodynamically stable state. Light of 325 nm wavelength induces the photoisomerization from the *trans* to the *cis*, light of 442 nm does the reverse. The surface tension of an aqueous surface covered with corresponding molecules depends on the illumination conditions. The molecular structure of $C_4AzoOC_4E_2$ is shown in fig. 5.7. The relative molecular weight of the photosurfactant is 414.6.

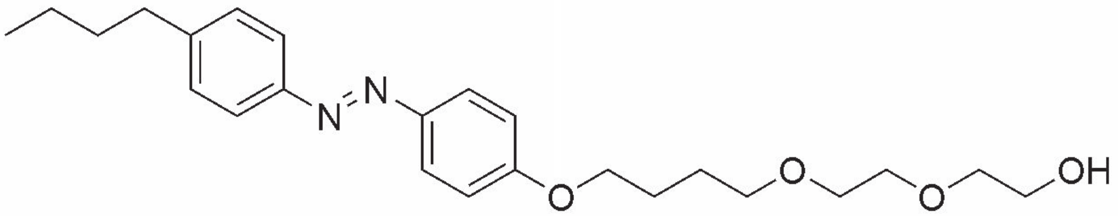

Fig. 5.7: Molecular structure of $C_4AzoOC_4E_2$.

The *trans* form of the surfactant has a planar structure with a dipole moment of 0.5 D while the *cis* form has a loop form with a dipole moment of 3.1 D, where D is the Debye unit = 3.336 x 10^{-30} Cm. For pure water, the dipole moment is about 2 D [162]. In the planar structure, the surfactant orients away from the interface as shown in fig. 5.8. A system with predominantly *cis* isomers has substantially higher surface tension than a system with an excess of *trans* isomers. Table. 5.1 summarize the properties of the

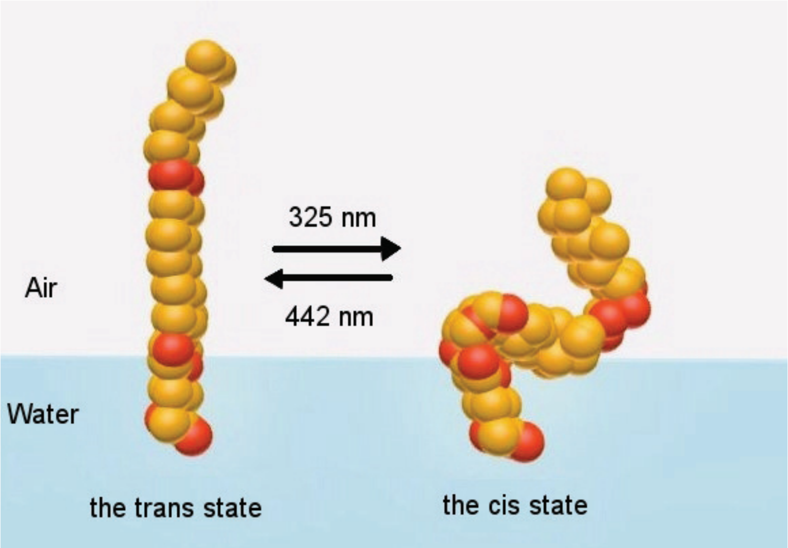

Fig. 5.8: Schematic representation of the orientation of the photosurfactant at the water-air interface.

surfactant at their *trans* and *cis* states.

Parameter	*the trans* state	*the cis* state
CMC (μM)	1.6	23.8
σ_{CMC} ($\mu N/m$)	28.9	39.6
Adsorption coefficient (m^3/mol)	1380	555
Molecular area (Å^2)	21	35
Dipole moment (D)	0.5	3.1

Table 5.1: Properties of the photosurfactant material [181]

The difference in saturated surface tension between the *trans* state and the *cis* state varies with the surfactant concentration. $C_4AzoOC_4E_2$ exhibits a surface tension difference of more than 10 mN/m between the two states for a wide range of concentration above their CMC [181]. Fig. 5.9 shows the equilibrium surface tension of all the photosurfactant solutions measured at various surfactant concentrations (reused with permission from Langmuir, [181]). Fig. 5.9(b) represents the data corresponding to $C_4AzoOC_4E_2$.

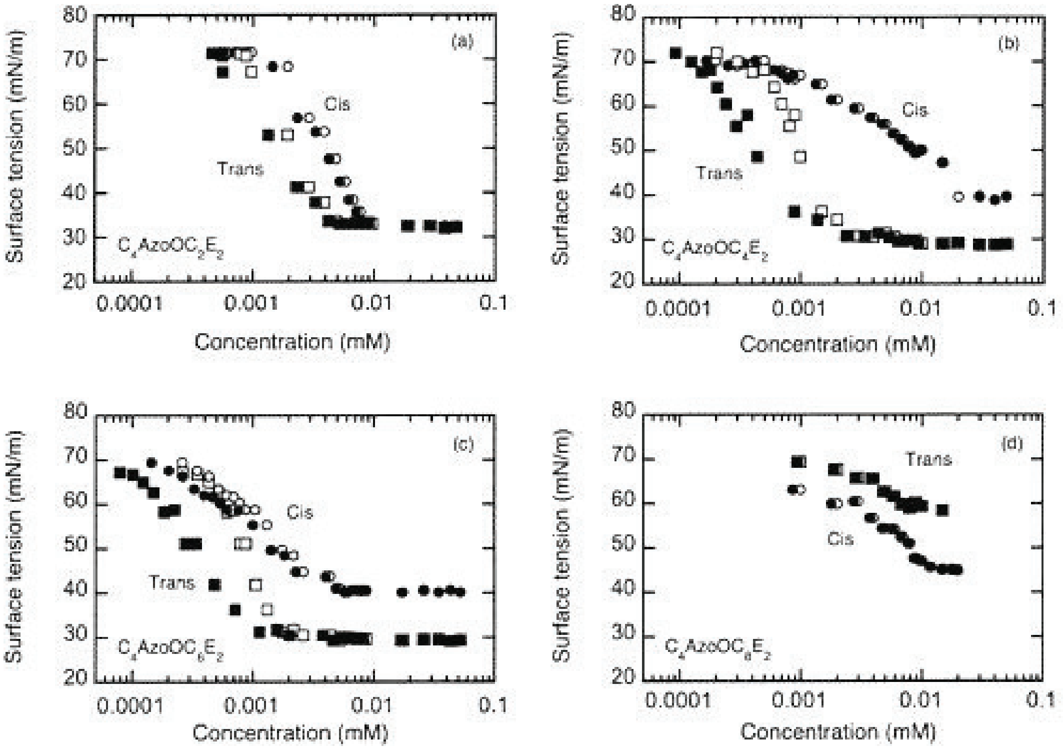

Fig. 5.9: Concentration dependence of equilibrium surface tension of photoresponsive surfactants under visible (squares) and UV light (circles). The open symbols represent the original data and solid symbols represent data corrected for interfacial adsorption to give the bulk concentration. Fig. 5.9(b) represents the data corresponds to $C_4AzoOC_4E_2$. Reused with permission from Langmuir [181]).

It is reported that the *cis* form of the surfactant reaches the interface quickly, leading to a *cis* rich state at the beginning but it is ultimately replaced by the *trans* isomers [177]. The photosurfactant material at CMC requires about 35 h to reach at its equilibrium surface tension value at room temperature [177]. For this reason, the surfactant concentrations used in the present study were well above CMC value of the *trans* form of the surfactant.

5.3.2 Photoswitching behavior of $C_4AzoOC_4E_2$ surfactant

As explained in the previous section, the surfactant material is photosensitive because of the presence of a photochromic azobenzene molecule in the surfactant system. To characterize the photoswitching behavior of the surfactant material, UV - Visible absorption spectra measurements were performed at different illumination conditions. Absorption spectra of 10 μM $C_4AzoOC_4E_2$ solution was recorded using SPECOL 2000

(Analytic Jena, Germany) spectrophotometer. The device consists of one sample arm and one reference arm. Both the $C_4AzoOC_4E_2$ solution (sample arm) and water (reference arm) were taken in clean quartz cubets. The length and breadth of the cubet was 1 cm. The light source used for UV illumination was a Hamamastu UV lamp (at 130 mW/cm^2) and a He-Cd laser was used for blue illumination (at 70 mW/cm^2). Initially, the absorption spectra of the sample was measured without any illumination (dark state) which is shown in fig. 5.10 (black symbols).

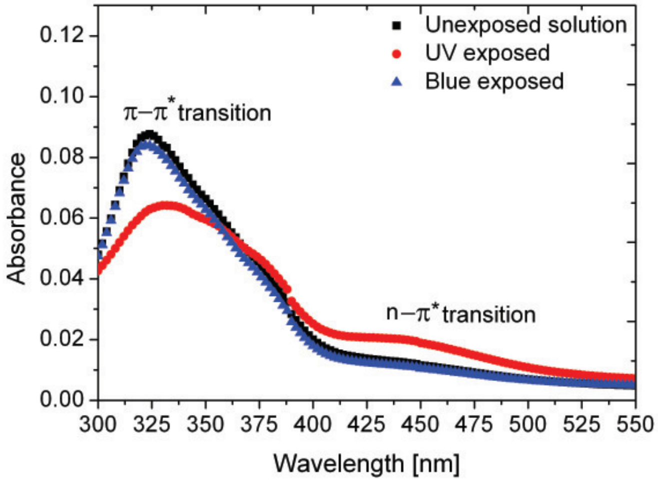

Fig. 5.10: Absorbtion spectra of 10 μM photosurfactant solution in water under different illumination conditions.

The absorption spectra exhibit two distinct absorption peaks, a strong absorption peak centered at 325 nm and a relatively small absorption peak centered at 440 nm. First peak corresponds to the absorption of the *trans* molecules ($\pi - \pi^*$ transition) and the second peak corresponds to the absorption of the *cis* molecules ($n - \pi^*$ transition) [181]. To analyze the photoswitching behavior of the photosurfactant solution, the following experiments were performed. The sample was illuminated with UV light for five minutes, and the corresponding spectrum was recorded using the spectrophotometer (red symbols in fig. 5.10). It was observed that the absorption peak at 325 nm decreased while the absorption peak at 440 nm increased. This shows the *trans-cis* conversion under UV illumination. The percentage of *trans* molecules in the sample after photoconversion can be calculated using the expression [188],

$$\%trans = \frac{Abs_{UV,325nm}}{Abs_{dark,325nm}} x100 \tag{5.20}$$

where $Abs_{UV,325nm}$ and $Abs_{dark,325nm}$ are the absorbance of the sample at 325 nm after UV irradiation and at dark state respectively. Here, % *trans* yeilds a value of about 30 % to that of the dark state. Further increase in the irradiation time does not change the absorbance value corresponding to the saturated *trans/cis* ratio in the solution in agreement with the reported work for azobenzene incorporated photosurfactants [188]. The method to determine the isomerization time scale is explained in chapter 6. To analyze the *cis-trans* conversion of the photosurfactant, UV exposed sample was illuminated with 442 nm emission of He-Cd laser and the corresponding absorption spectrum was recorded. At this stage, the absorption at UV increased while absorption at blue region decreased (blue symbols). From the fig. 5.10, it is clear that the photoisomerization was almost completely reversible. Repeatability of photoisomerization was confirmed by recording the spectra for alternate UV and blue irradiation for 10 cycles, which is shown in fig. 5.11.

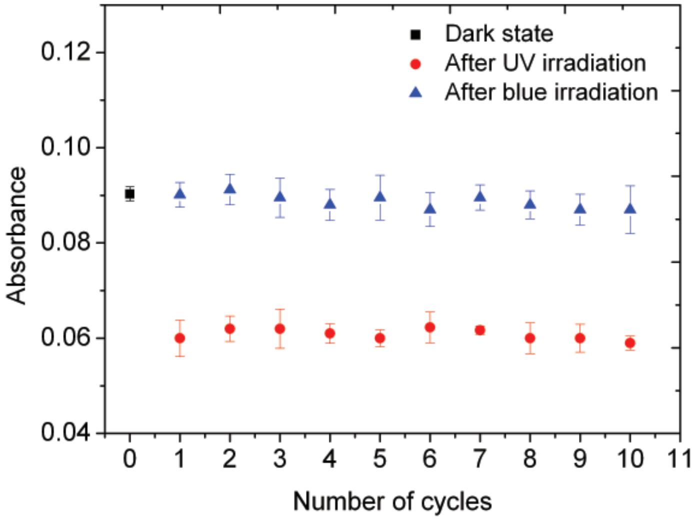

Fig. 5.11: Reversibility of photoisomerization of the 10 μM photosurfactant solution. The sample was alternately illuminated with UV and blue light. Absorbance measured at 325 nm after each illumination is shown here.

5.3.3 Photoisomerization kinetics of $C_4AzoOC_4E_2$ surfactant

The photoisomerization kinetics of the surfactants containing azobenzene is reported in ref. [125, 181, 189]. First order kinetics of photoisomerization is analyzed on the assumption that the absorption of UV photons by the *trans* molecules results in conversion to the *cis* molecules. Thermal isomerization of the *cis* isomers back to the *trans* isomers is neglected. The rate of change of *trans* molecules due to light absorption is given by [125, 181]:

$$\frac{d\Gamma_{trans}}{dt} = -a_{trans}\Gamma_{trans} + b_{cis}\Gamma_{cis} \tag{5.21}$$

and for *cis* isomers:

$$\frac{d\Gamma_{cis}}{dt} = a_{trans}\Gamma_{trans} - b_{cis}\Gamma_{cis} \tag{5.22}$$

where a_{trans} and b_{cis} are the kinetic constants of the photoisomerization for *trans*-*cis* and *cis*-*trans* respectively. a_{trans} is defined as:

$$a_{trans} = \epsilon_{trans} I_0 \phi_{trans} \lambda / hN_A c \tag{5.23}$$

Similarly, b_{cis} is expressed as:

$$b_{cis} = \epsilon_{cis} I_0 \phi_{cis} \lambda / hN_A c \tag{5.24}$$

where ϵ_{trans} and ϵ_{cis} are the molar extinction coefficient for the *trans* and the *cis* molecules respectively, I_0 is the incident intensity, h is the Planck constant, c is the velocity of light and ϕ_{trans} and ϕ_{cis} are the quantaum efficiency for *trans*-*cis* and *cis*-*trans* conversion respectively. On introducing a non-dimensional concentration $\Gamma_{trans}(t)$, defined as,

$$\Gamma_{trans}(t) = \Gamma_{trans} / \Gamma^0_{trans} \tag{5.25}$$

where Γ^0_{trans} is the initial concentration of the *trans* molecules. At the initial condition where the *trans* rich surface is irradiated with 325 nm beam, the influence of the term $b_{cis}\Gamma_{cis}$ in eq. 5.21 can be neglected. To get the relation between photoconversion time scale and the incident intensity, solving the equation for *trans*-*cis* photoconversion under the initial condition, at *t=0*, $\Gamma_{trans}(t)$=1, we get for small time scale,

$$\Gamma_{trans}(t) = exp(-a_{trans} t) \tag{5.26}$$

The above equation shows that the time scale of photoisomerization is inversely proportional to the incident intensity, the molar extinction coefficient and the photoconversion efficiency. Since the molar extinction coefficient and the photoconversion efficiency are constant for a material, the isomerization mechanism rate can be controlled by varying the incident intensity.

To understand the dynamic response of the interface, one has to account for the adsorption-desorption flux in addition to the photoconversion process. This approach is limited to the case where the surfactant concentration is below the CMC. The adsorption flux is proportional to the available area at the interface and the desorption flux is proportional to the surface excess concentration of the surfactant molecule [125]. For a system containing both the *trans* and the *cis* isomers, the rate of surface excess due to adsorption-desorption mechanism can be expressed as [125],

$$\frac{d\Gamma_{trans}}{dt} = k_{ads}^{trans} c_{sub}(1-\omega_{trans}\Gamma_{trans}-\omega_{cis}\Gamma_{cis}) - k_{des}^{trans}\omega_{trans}\Gamma_{trans} \tag{5.27}$$

and

$$\frac{d\Gamma_{cis}}{dt} = k_{ads}^{cis} c_{sub}(1-\omega_{trans}\Gamma_{trans}-\omega_{cis}\Gamma_{cis}) - k_{des}^{cis}\omega_{cis}\Gamma_{cis} \tag{5.28}$$

where k_{ads}^{trans} and k_{des}^{trans} are the adsorption and desorption constants for the *trans* molecule, k_{ads}^{cis} and k_{des}^{cis} are the adsorption and desorption constants for the *cis* molecule, ω_{trans} and ω_{cis} are the surface area per molecule of the surfactant and c_{sub} is the surfactant concentration in the subphase. Combining the fluxes due to absorption-desorption and photoconversion, we get,

$$\frac{d\Gamma_{trans}}{dt} = k_{ads}^{trans} c_{sub}(1-\omega_{trans}\Gamma_{trans}-\omega_{cis}\Gamma_{cis}) - k_{des}^{trans}\omega_{trans}\Gamma_{trans} - a_{trans}\Gamma_{trans} + b_{cis}\Gamma_{cis} \tag{5.29}$$

This change in surface excess concentration results in a hydrodynamic flow from higher surface tension region to lower surface tension region. There are two works which utilizes photosurfactant adsorbed to the interface for generating light-induced Marangoni flow [10, 125]. Diguet et al. utilized this mechanism for controlling the motion of an oil droplet floating over photosurfactant solution [10]. E. Chevallier et al. reported the accumulation of talcum powder sprinkled over photosurfactant solution using light [125]. They observed inward flow for both the UV and blue illumination. Their kinetic model predicts that fast desorption of the *cis* surfactant from the interface increases the surface tension in the illuminated area, irrespective to the irradiation wavelength.

6 Light-induced Marangoni tweezers - Experimental techniques and flow profile diagnostics

6.1 Introduction

Photoswitchable molecules that undergo reversible structural change upon light irradiation have numerous applications, ranging from life science [180] to interfacial fluid mechanics [9, 10]. A few to mention are the creation of a reversible wettability gradient over a solid surface [9] or an interfacial tension gradient at a liquid-liquid interface [10] to transport millimeter-sized droplets. The present work demonstrates the trapping and manipulation of microparticles using light-induced surface tension gradient. Commonly employed particle manipulations techniques are optical trapping [2], dielectrophoresis [3], optoelectronic tweezers [5] or plasmonic tweezers [190]. All these schemes rely on the so-called gradient force that scales as the third power of the particle diameter in the Rayleigh regime [2]. For this reason the trapping force rapidly diminishes with decreasing particle diameter. This chapter presents an optical method for the trapping and manipulation of micron-sized particles adsorbed at a gas-liquid interface based on optically-induced Marangoni flow.

This chapter has two sections. The first section describes the principle of particle trapping based on optically-induced Marangoni flow. The second section deals with the experimental design and the analysis techniques used for velocity profile diagnostics at the air-water interface. Dependence of experimental parameters such as laser exposure time, laser intensity, particle size and surfactant concentration is studied. As a potential application of this method, it is demonstrated that the inward Marangoni flow can be utilized to trap and manipulate adsorbed micro-spheres at the air-water interface at much lower intensity than conventional optical tweezers.

6.2 Principle of optically-induced Marangoni flow

The principle of optically-induced Marangoni flow is demonstrated in fig. 6.1.

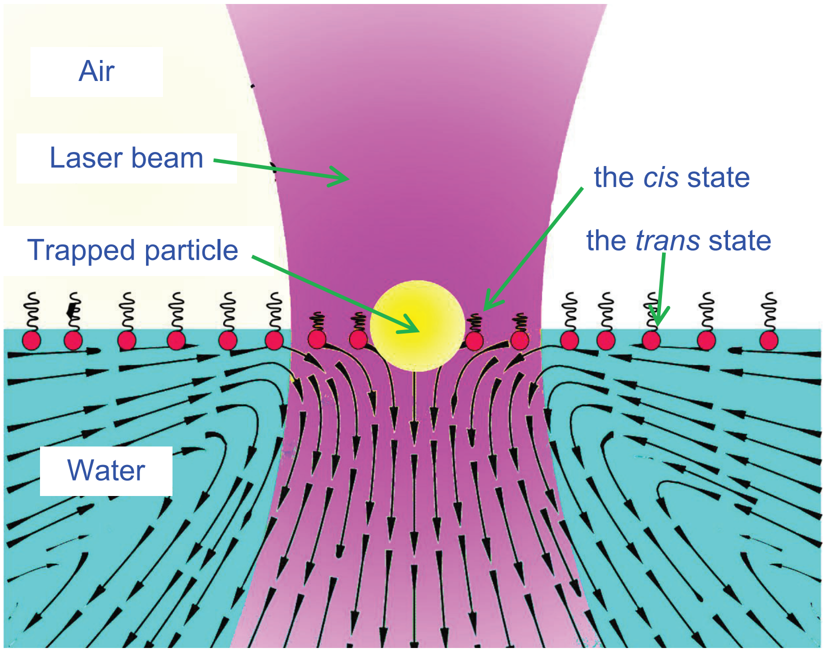

Fig. 6.1: Principle of optically-induced Marangoni flow. A laser beam of either 325 nm or 442 nm wavelength is focused onto a liquid surface covered with photoresponsive surfactants. The local change in surface tension creates an inward or outward flow that may be utilized to trap and manipulate particles.

The method relies on the photoswitching of photosurfactant molecules adsorbed to the air-water interface. The surfactant exists in two isomeric states, a *trans* state and a *cis* state. When adsorbed at the interface, the *cis* rich surface exhibits higher surface tension that of the *trans* rich state. Light of 325 nm wavelength induces the photoisomerization from *trans* to *cis* state, light of 442 nm the reverse. One can locally change the surface tension at the liquid surface using light that generates a hydrodynamic flow from the lower surface tension region to the higher surface tension region. Upon focused illumination with the 325 nm wavelength, population of the *cis* molecules increase at the focal region, which results in a localized increase in the surface tension. The inward flow generated by the gradient in surface tension along the interface is utilized to trap and manipulate the microparticles adsorbed at the air-water interface. Particles are dragged towards the focal spot and get trapped at the focal spot. Fig. 6.2

shows the artistic representation of the trapping mechanism.

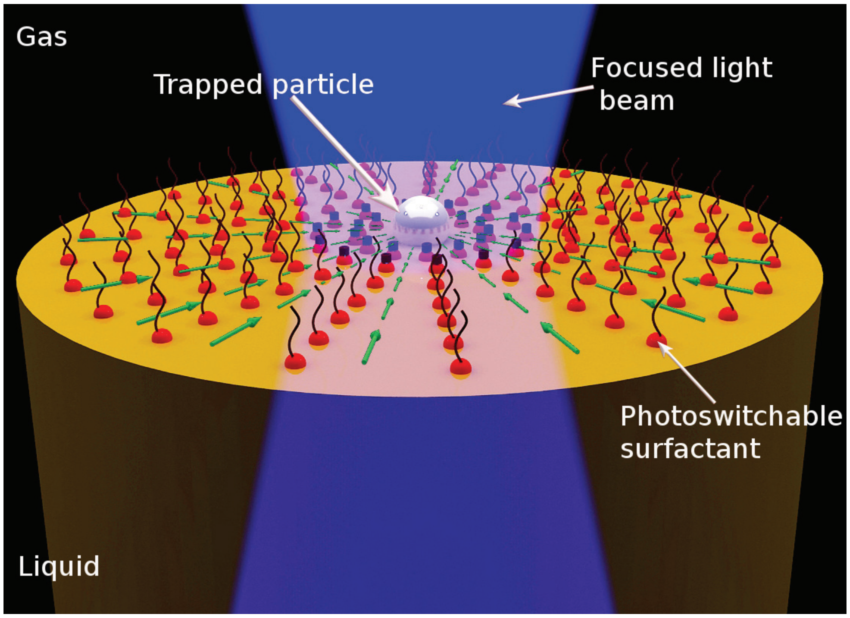

Fig. 6.2: Artistic representation of particle trapping using optically-induced Marangoni flow.

Furthermore, the direction of the flow can be reversed by switching the wavelength to 442 nm (after irradiating with 325 nm). At 442 nm irradiation, the *cis* molecule switches back to the *trans* molecule, resulting in a relatively lower surface tension at the focal point. Another important advantage of this technique is the trapped particle can be manipulated along the interface. A potential landscape that extends over some millimeter range can be created using a single light beam makes this technique a suitable candidate for the massive manipulation of particles adsorbed at the fluid-fluid interface.

6.3 Experimental setup

Fig. 6.3 shows the schematic of the experimental setup used for the trapping and manipulation of microparticles adsorbed at the air-water interface using optically-induced Marangoni flow. The experimental setup consists of a dual-wavelength He-Cd laser (325 and 442 nm), beam steering optics, focusing lens, inverted microscope and imaging optics.

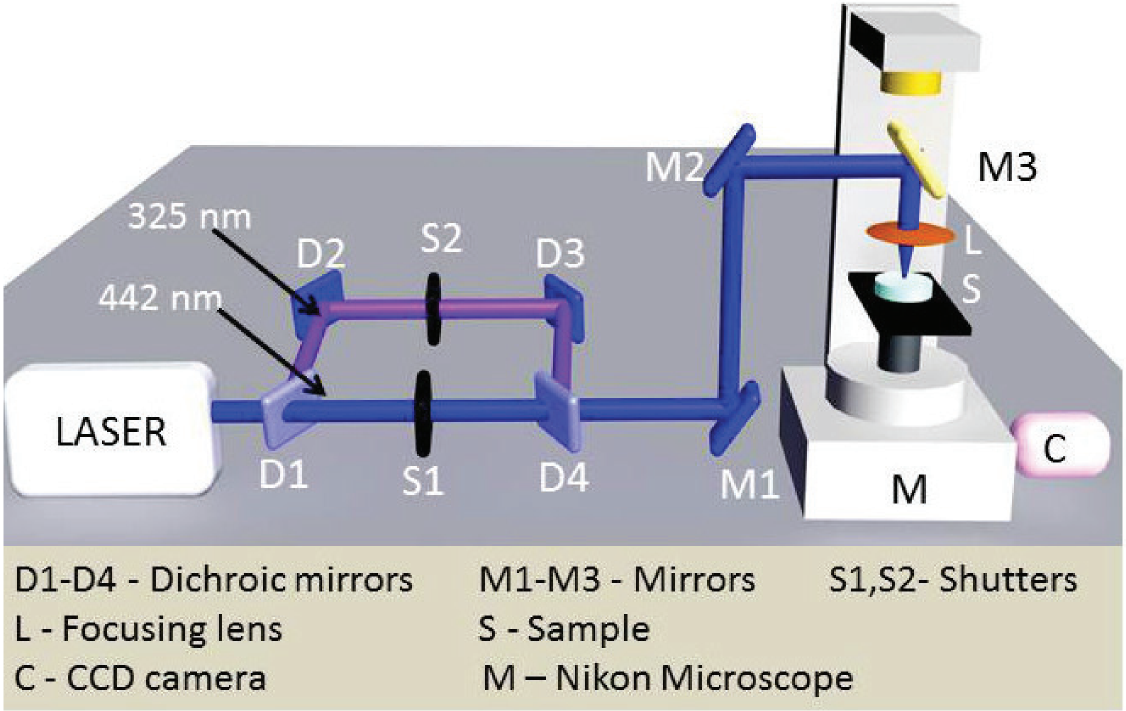

Fig. 6.3: Experimental setup comprising a dual wavelength (325 nm and 442 nm) He-Cd laser and a microscope for imaging the flow at the liquid surface.

Laser source

The photosurfactant material used in the present study exhibits reversible photoisomerization property (for more details, refer sec: 5.3.1). The photosurfactant material exhibits two absorption peaks centered at 325 nm and 440 nm wavelength. The present work requires both UV and blue light to explore the photoswitching behavior of the molecule. A He-Cd laser (Kimmon Koha, Japan) that emits both the 325 nm and 442 nm wavelengths simultaneously was used for the experiments. Laser delivers a maximum output power of 80 mW at 442 nm and 20 mW at 325 nm. For more technical details of the He-Cd laser, reader is referred to sec: 3.7 of this thesis.

Dichroic mirror assembly

For selective tuning of the flow direction, it was necessary to switch the wavelength between 325 nm and 442 nm. Laser output mode which emits both the wavelengths simultaneously was chosen for the experiments. To select the desired wavelength, a system of 4 dichroic mirrors as shown in fig. 6.4 was used. Dichroic mirrors were

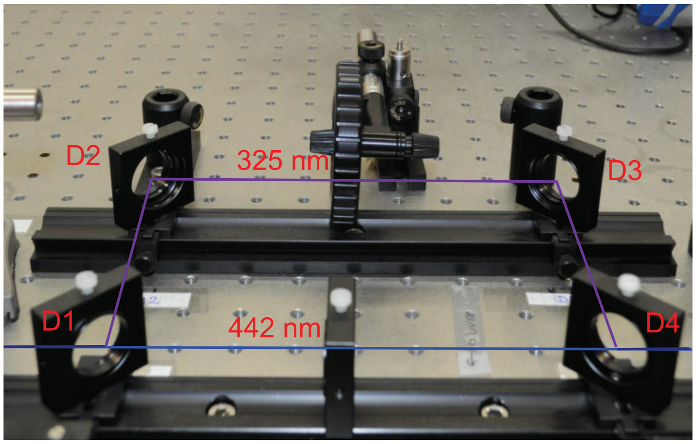

Fig. 6.4: Dichroic mirror assembly.

chosen in such a way that, it reflects 325 nm beam and transmits 442 nm beam. At the position of D1, both the beams incident the mirror at an angle of 45^o. D1 reflects 325 nm beam and transmits 442 nm laser beam. Dichroic mirrors D2 and D3 were used to guide the 325 nm laser beam to D4. At the position of D4, both the beams combine together and propagate along the designed optical path. Beam shutters (Newport Model SC10) were used to control the laser exposure time, and the tunable neutral density filters were used to control the laser power.

Beam steering optics

The output beam from the dichroic assembly was expanded using a 1 : 9 Galilean beam expander setup (as explained in sec: 3.7.2). Mirrors M1 and M2 in the fig. 6.3 were manually adjustable mirrors that guides the laser beam to the cubic filter M3. Cubic filter M3 reflects both the 325 nm and 442 nm laser beams and transmits all other wavelengths. The white light source used for imaging also passes through this cubic filter. Laser light was irradiated from the top and the imaging was performed from the bottom as shown in fig. 6.5.

Focusing lens

A plano-convex lens (L, Thorlabs, Germany) having a focal length of 10 cm was used to focus the laser beam at the air-water interface. The planoconvex lens was

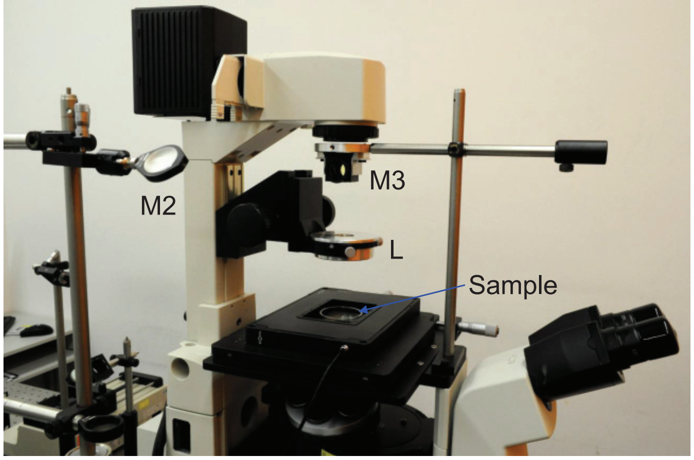

Fig. 6.5: Photograph of the experimental setup used for trapping and manipulation of particles using optically-induced Marangoni flow

incorporated into the microscope as shown in fig. 6.5. The diffraction limited spot size of a Gaussian beam at the laser focus can be calculated using the expression [191]:

$$d_{spot} = 2.44 \frac{\lambda f_{lens}}{d_{beam}} \tag{6.1}$$

where λ is the wavelength of the laser beam, d_{beam} is the diameter of the laser beam and f_{lens} is the focal length of the plano-convex lens used. The diameter of the incident beam was 10 mm. Calculation yields a focal spot size of about 8 μm at 325 nm and 11 μm at 442 nm wavelength.

Imaging optics

A Nikon Eclipse TE 2000 microscope equipped with a UV-VIS CCD camera (ANDOR iXon, model DU-897D-CSO-UVB) was employed for monitoring the dynamics at the air-water interface. Objectives used for the present work were Nikon 4X (NA 0.2) and 20X (NA 0.45). Microscope was equipped with a white light source for bright light illumination.

Materials

A 1 mm layer of the photosurfactant solution was filled into a clean glass petri-dish with a diameter of 5 cm. The height of the surfactant film was measured using the microscope by monitoring the glass-water and the water-air interface. If not mentioned otherwise, at the beginning of an experiment ($t = 0$), the solution was in its "dark" state, where "dark" refers to the equilibrium attained after a prolonged absence of light. Samples in the dark state are almost exclusively (> 99 %) in *trans* form [181]. A freshly prepared photosurfactant solution exhibits a surface tension of about 70 mN/m which decreases to about 30 mN/m at its saturated state [177, 181]. The photosurfactant material requires approximately 10^4 s to reach at its saturated surface tension value at the concentrations used in this work [177]. So the solution was kept at dark for 3 h before starting the experiments.

Polystyrene microparticles (15 μm diameter) purchased from Micromod, Germany was used for both the flow diagnostics and trapping experiments. These particles were surfactant free, and charge stabilized. Very low concentration of the particle dispersion was dried. The dried particles were then carefully sprinkled over the surfactant solution. Density of the polystyrene particle (1.05 g/m^3) was very close to that of water (about 1 g/m^3) at room temperature. So the gravitational force acting on the particle was negligible compared to the surface forces making them to adsorb at the air-water interface. To characterize the velocity field at the air-water interface, particle streak velocimetry was performed.

6.4 Particle streak velocimetry

Commonly employed particle-based flow visualization methods are Laser Doppler Velocimetry (LDV) [192], Particle Streak Velocimetry (PSV) [193, 194] and Particle Image Velocimetry (PIV) [195, 196]. Both the LDV and PIV require an additional laser beam for realizing the flow diagnostics. General requirement for the selection of particles used for flow visualization is that the particles are neither corrosive nor toxic, and the image contrast between the particle and the background is high.

The present work adopts particle streak velocimetry for flow profile diagnostics. This method is relatively simple and can be performed without an additional laser beam for the excitation of the probe particle. In PSV, particles are illuminated with a continuous light source and the particle trajectory is recorded for a finite exposure time. The recorded image appears as a streak line with a length proportional to the velocity magnitude. Presence of streaks connecting the initial and end points of the particle trajectory makes the velocity estimation easier. Earlier studies report that the velocity data obtained by PSV is around 10 % less accurate than that obtained from PIV [197].

Another disadvantage is that, the direction of flow cannot be revealed from the streak images. For the study of converging or diverging flow as in the present case, PSV is a suitable tool for getting the basic nature of the velocity field. Experimental procedure followed to record streak image is explained as follows. The air-water interface is illuminated with a white light source equipped with the microscope. Illumination intensity is controlled in such a way that the exposure time for recording the streak image does not result in the saturation of the CCD pixels. Andor CCD camera is used here, and the camera operation is controlled by Andor software, in its accumulation mode. In accumulation mode, camera captures N frames, each having exposure time of t s, then merge all these frames together to form a single image having exposure time of $N.t$ s. To extract the velocity data from the streak images, Nikon NIS elements image analysis software is used. Initially, pixel calibration is performed as explained in sec: 3.7.4. Then, a line is drawn over the streak connecting the initial and the end point, and the length of the streak is measured. Value of the particle diameter is subtracted from this length, which gives the displacement of the particle. Average velocity of the particle is computed by taking the ratio of the streak length to the corresponding exposure time. [1]

6.5 Results and discussion

The following sections deal with the results and discussion. Dependence on experimental parameters such as laser exposure time, incident intensity and surfactant concentration are discussed.

6.5.1 Inward flow characterization

Illumination with 325 nm beam induces an inward flow directed towards the focal point. To characterize the inward flow profile, the following experiment was performed. A 50 μM photosurfactant solution was prepared, and polystyrene particles were sprinkled over the surfactant solution. Then 325 nm beam (5 mW power) was focused at the air-water interface, and the irradiation continued for 0.5 s, simultaneously the images were recorded using Andor camera. Typical examples of the particle streak images recorded at 325 nm illumination corresponding to an exposure starting

---

[1] A part of the results discussed in this chapter is published in Angew. Chem. Intl. ed. (DOI: 10.1002/anie.201302111). This author, Prof. Steffen Hardt, Dr. S.D. George and Dr. Tobias Baier were involved in the interpretation of the results. Prof. Markus Biesalski and Mrs. Martina Ewald are greatly acknowledged for the surfactant synthesis and the characterization.

at $t = 0$ and lasting for 0.5 s is shown in fig: 6.6. To evaluate the radial flow profile, the plane around the laser spot was subdivided into radial segments of 20 μm extension, corresponding to the resolution of the velocimetry. The velocity in a specific radial bin was determined by evaluating the average over 5 particles. The standard deviation, plotted as error bars, was determined based on these 5 measurements. Particle velocity as a function of the distance of the particle from the laser spot was determined and fig. 6.7 displays the corresponding inward flow profile.

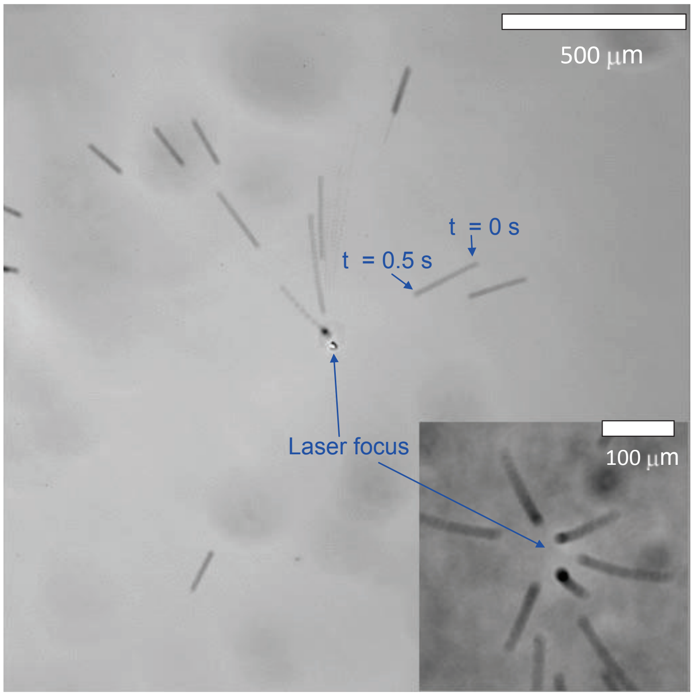

Fig. 6.6: Particle streak velocimetry image recorded using a 4X objective. Inset shows the image recorded using a 20X objective.

One of the most striking features of the inward flow profile is the maximum velocity occurring at around 300 μm away from the focal point. Certainly, owing to the finite exposure time and particle size in the particle streak velocimetry measurements, the spatial resolution was limited, but this cannot explain why the velocity maximum occurs at a radial distance much bigger than the beam waist. The flow at the liquid surface has a dilatational character with $\nabla.u \neq 0$, where u is the velocity at the surface. The radial inflow compresses the surfactant monolayer, and, after some time, leads to the formation of aggregates that are presumably multilayer arrangements of surfactant molecules. The formation of multilayer structures is a process occurring when a Langmuir monolayer is compressed beyond its stability limit [198, 199]. In

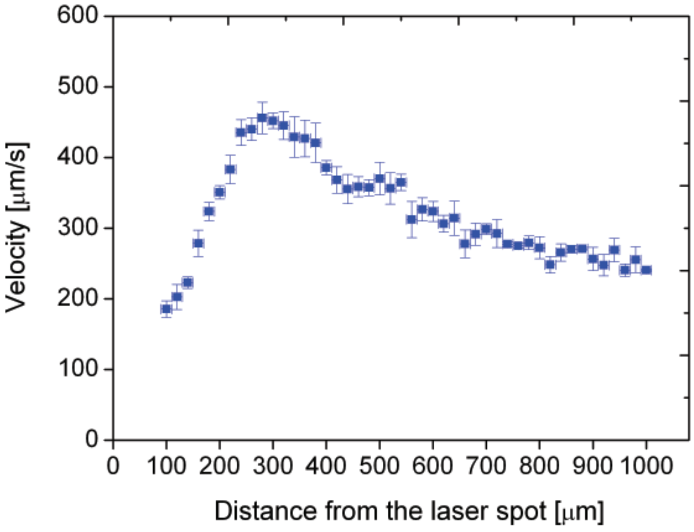

Fig. 6.7: Flow profile obtained after 0.5 s exposure with 325 nm light at a laser power of 5 mW.

general, the dilatational flow produces a radial surfactant concentration gradient and a surfactant-crowded region close to the focal spot. The crowding is expected to give rise to a region of high (shear and dilatational) surface viscosity, while the surfactant concentration gradient is expected to produce Marangoni stresses [82, 200]. It is conjectured that due to the former, an almost immobile liquid surface is formed around the laser focus, which results in a maximum of the velocity occurring at a comparatively large radial distance away from the focal spot. When the illumination at 325 nm continues, the flow velocity decreases, bringing the inflow to a halt after about 10 s. Though the exact physical mechanism behind this observation is not clear, it is hypothesized the surfactant crowding stops further inflow of *trans* molecules towards the focal point. Fig. 6.8 shows the formation of aggregates around the laser focus. In this case, the surfactant solution was free from tracer particles. It can be seen that, as 325 nm illumination progress, surfactant crowded area increase. This observation explains the behavior of the velocity profile.

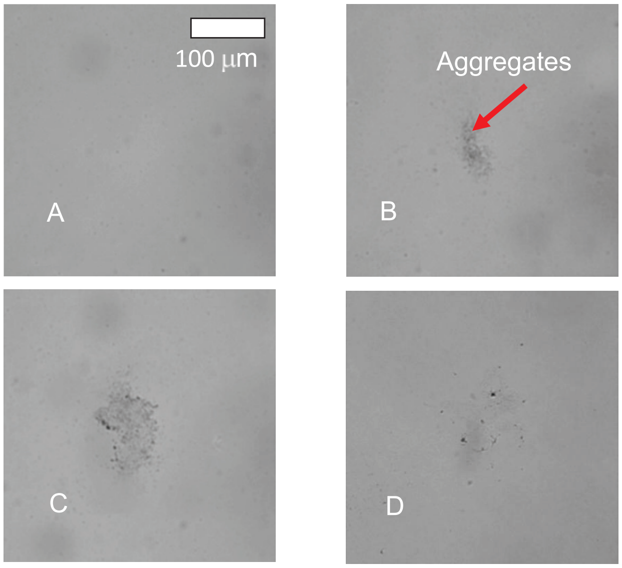

Fig. 6.8: CCD images showing the presence of aggregates around the laser spot. A)-C). Sequence of images recorded upon UV illumination at 0, 1 and 2 s exposure respectively. D). Image shows the disintegration of aggregates upon blue irradiation.

6.5.2 Outward flow characterization

The flow direction at the interface can be reversed by switching the wavelength to 442 nm. To study this mechanism, 442 nm light was switched on after 2 s illumination with 325 nm light. It was observed that the direction of the flow reversed, i.e., directs away from the laser spot. The laser power was set at 30 mW to get a significant outward flow. A typical example of particle streak image recorded for outward flow recorded using 20X objective lens is shown in fig. 6.9 (Left). Fig 6.9 (Right) shows the corresponding outward flow velocity profile. It should be noted that, for outward flow, the maximum flow velocity was substantially less than that observed for inward flow. Possible reasons for this observation are, the *cis-trans* isomerization mechanism is slower than the *trans-cis* isomerization and the photoconversion efficiency is less in the case of *cis-trans* conversion compared to *trans-cis* conversion [181]. Photoconversion efficiency of *trans-cis* photoisomerization is close to 1 while *cis-trans* conversion, this value is about 0.69 only. Moreover, the chromatic aberration of the lens used leads to larger spot size at the interface for 442 nm, which results in a reduction in the incident intensity.

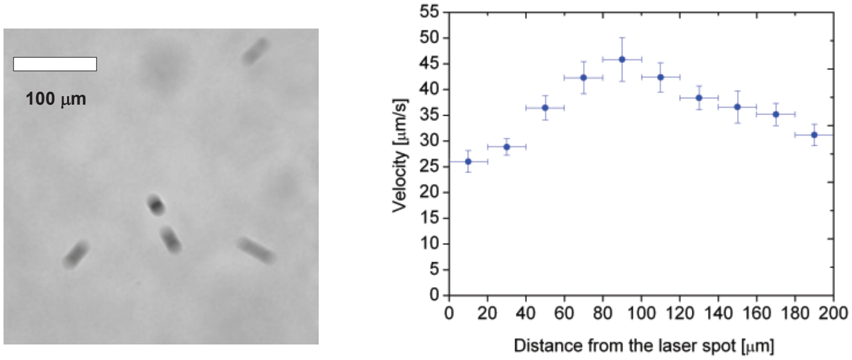

Fig. 6.9: Outward flow characterization: (Left) Particle streak image showing the outward flow profile while irradiated with blue light at 30 mW (Right) Flow profile at 30 mW.

6.5.3 Dependence of laser exposure time on flow profile

To analyze the effect of laser exposure time on the inward flow, the following experiment was performed. A 1 mm layer of 50 μM solution was irradiated using 325 nm beam at an incident power of 5 mW for two different exposure times: 0.25 s and 0.5 s. The resulting flow profile is shown in fig. 6.10.

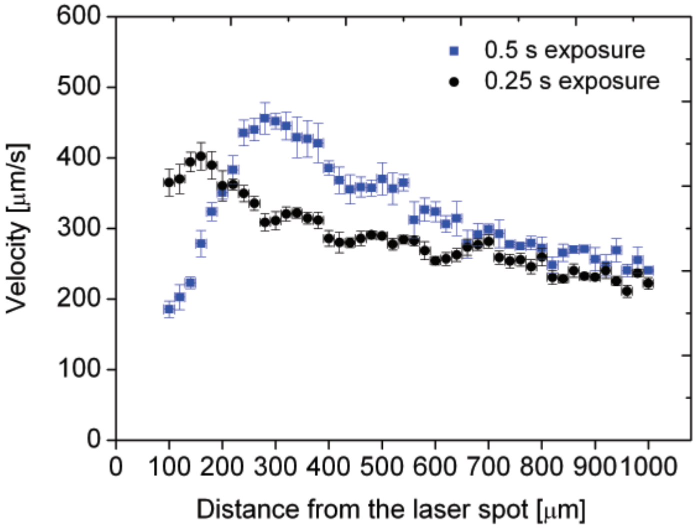

Fig. 6.10: Flow profiles at the surface of a 50 μM solution after different exposure times at a laser power of 5 mW.

It can be seen that for $t = 0.25$ s, the velocity maximum occurs at a smaller value of the radial coordinate. This can be explained by the fact that at this point in time, the surfactant aggregate is less extended than at $t = 0.5$ s, yielding a smaller region with a high surface viscosity.

6.5.4 Dependence of incident intensity on flow profile

Increase in incident intensity enhances the photoisomerization mechanism. Photoisomerization kinetics of photosurfactants incorporated with azobenzene molecule predict an inverse relation with the photoisomerization time scale and intensity [181]. As a result, one expects increased flow velocity at higher intensity than that of the lower intensity. To study the dependence of laser intensity on the velocity profile, the following experiments were performed. Table 6.1 gives the values of the incident laser power and corresponding intensity at the focal spot for 325 nm beam while focused using a 10 cm lens. Fig. 6.11 displays the velocity profile for 50 μM and 25 μM solutions at different incident intensities.

Laser power (mW)	Intensity at the focal spot (W/m^2)
0.25	0.49 x 10^8
0.5	0.98 x 10^8
2.5	4.9 x 10^8
5	9.8 x 10^8

Table 6.1: Intensity at the focal spot for 325 nm wavelength

A maximum flow velocity of about 500 $\mu m/s$ was achieved with 5 mW laser power. The shift of the velocity maximum can again be explained by the increasing size of the surfactant aggregate, corresponding to a growing region of low surface mobility. The increase in velocity can be explained in terms of photoisomerization time scales. The time scale of the photoisomerization kinetics is inversely proportional to the light intensity [181]. Therefore, a few instants after the illumination has started, one expects a higher fraction of *cis* isomers in the focal region if the light intensity is increased. Certainly, the photoisomerization time scale will only play a role if it is not much smaller than the time span over which the flow is observed, which is 500 ms in fig. 6.11.

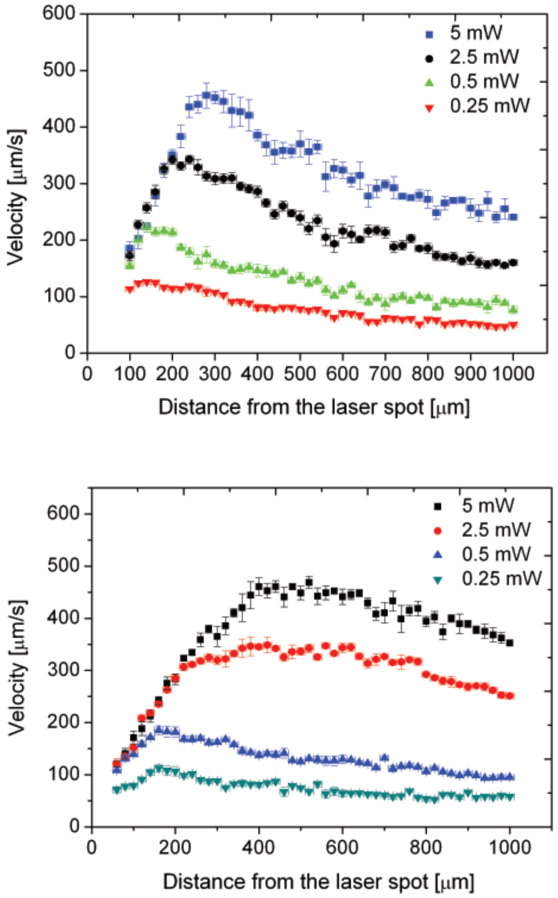

Fig. 6.11: Dependence of incident intensity on velocity profile: (Top) Flow profiles at the surface of a 50 μM solution after an exposure time of 0.5 s at different values of the laser power. (Bottom) Flow profiles at the surface of a 25 μM solution.

6.5.5 Time constant determination from the transmittance measurements

Photoisomerization time constant for *trans-cis* isomerization was determined from transmittance measurement of the photosurfactant material. Fig. 6.12 shows the schematic of the experimental setup used for the transmittance measurement. A Hamamastu UV Lamp with a UV filter was used as the excitation source. Intensity of the UV light was set at 2.97 x 10^3 W/m^2. A low power He-Cd laser (5 mW) was used to measure the transmittance change of the photosurfactant solution at the 325 nm wavelength. The transmitted laser power was measured using a Newport laser power meter (Model Number 1918-C). All the measurements were carried out only after the laser was stabilized (20 minutes) so that the variation in power was less than

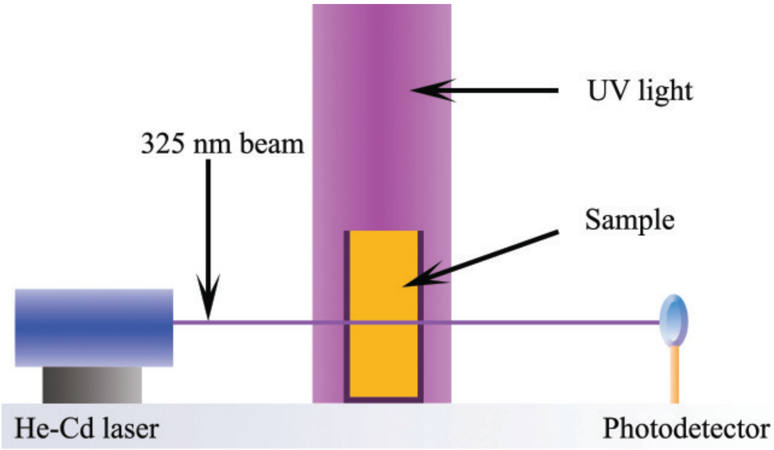

Fig. 6.12: Experimental setup used for the transmittance measurements.

2 %. A 50 μM surfactant solution taken in a 1 cm x 1 cm cubet was placed on the UV light path. The transmitted power of the 325 nm beam through the sample was measured before irradiation with the UV source. Let P_I be the incident power and P_T be the transmitted power at time t, then the transmittance of the for the surfactant solution T_λ for a particular wavelength λ can be calculated using the simple relation,

$$T_\lambda = \frac{P_T}{P_I} \tag{6.2}$$

Transmitted power through the sample was measured using the power meter and the corresponding transmittance value was calculated using eq: 6.2. Fig: 6.13 shows the transmittance at 325 nm wavelength as a function of irradiation time for 50 μM surfactant solution at an intensity of 2.97 x 10^3 W/m^2. Transmittance curve shows an exponential increase with respect to the irradiation time. Illumination with the UV light switches the molecules from *trans* state to *cis* state, results in a reduction in population of the *trans* molecule. Correspondingly, the absorption at 325 nm decreases that explain the observed exponential variation in the early stages of the temporal response of the transmittance. On prolonged irradiation, the solution reaches in a photostationary state where no more transmittance change was observed [188]. This corresponds to the saturated *cis/trans* ratio in the solution. The exponential nature of the transmittance can be fitted using the exponential function as [188],

$$T_\lambda = T_{initial} - A\exp(-t/\tau) \tag{6.3}$$

where $T_{initial}$ is the transmittance value before UV illumination and t is the irradiation time. Exponential fit for the experimentally determined transmittance measurement

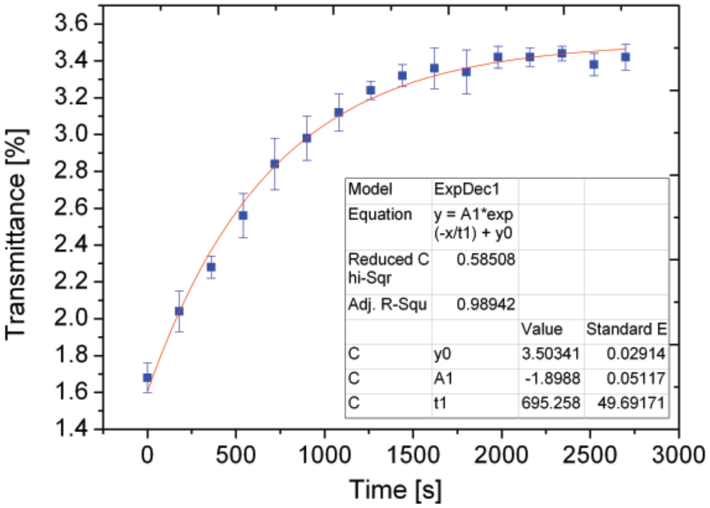

Fig. 6.13: Graph showing the transmittance measured at 325 nm plotted against the irradiation time.

yields a *trans-cis* time constant of 695 ± 49 s. Exponential fitting was performed using Origin 8 software (OriginLab Corporation, USA). The fitting parameters are shown in fig 6.13.

Assuming the inverse relation between the incident intensity and the isomerization time constant [181], one can determine the time constant t_i corresponding to an incident intensity I_i using the relation,

$$t_i = t_0 \frac{I_0}{I_i} \tag{6.4}$$

where t_0 is the photoisomerization time constant at an incident intensity I_0. Fig. 6.14 shows the calculated *trans-cis* time constants corresponds to the intensities shown in table. 6.1. A photoisomerization time constant of 41.6 ms was obtained for a light intensity of 0.49 x 10^8 W/m^2 (corresponding to a laser power of 0.25 mW at 325 nm wavelength), dropping to 2.08 ms when the laser power was increased to 5 mW. These time scales are roughly of the order of the flow observation time scale, therefore corroborating the hypothesis that the increase of flow velocity at higher values of the laser power is due to the faster conversion from *trans* to *cis* isomers.

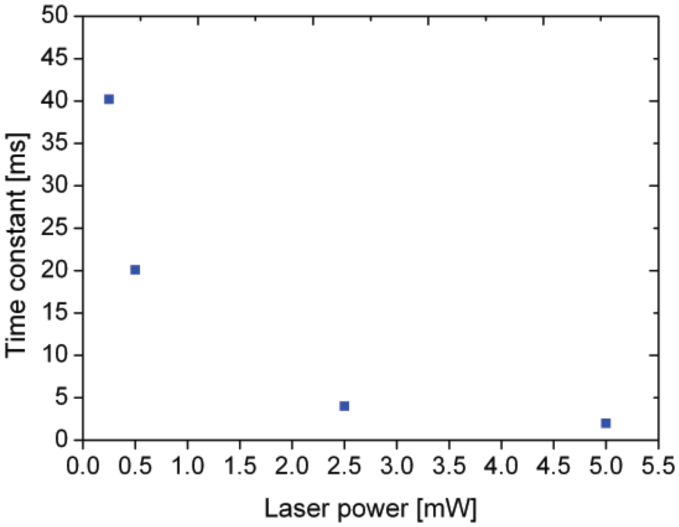

Fig. 6.14: *Trans-cis* photoconversion time scale for 50 μM solution at various incident intensities.

6.5.6 Dependence of surfactant concentration on flow profile

The dependence of surfactant concentration was studied by performing the flow profile measurements for different concentrations of the surfactant solution: 10 μM, 25 μM and 50 μM. In each case, the flow velocity measurements were performed as explained in sec: 6.4. Figure. 6.15 (Top) displays the dependence of the inward flow field on the surfactant concentration at an incident laser power of 5 mW. Initially, the sample contains almost exclusively *trans* isomers that are converted to *cis* isomers by the UV irradiation. It is worth noting that the critical micelle concentration (*CMC*) is significantly different for the trans ($CMC_{trans} = 1.6\ \mu M$) and the *cis*-enriched ($CMC_{cis} = 23.8\ \mu M$) state [181]. Above the *CMC*, the surfactant monolayer is virtually incompressible. For concentrations between CMC_{trans} and CMC_{cis} photoisomerization by 325 nm light converts the virtually incompressible surfactant phase into a compressible one. The latter could explain why a substantial augmentation of the overall flow velocity was being observed when increasing the surfactant concentration from 10 μM to 25 μM, but no further increase was found (apart from local variations) when elevating the concentration level to 50 μM.

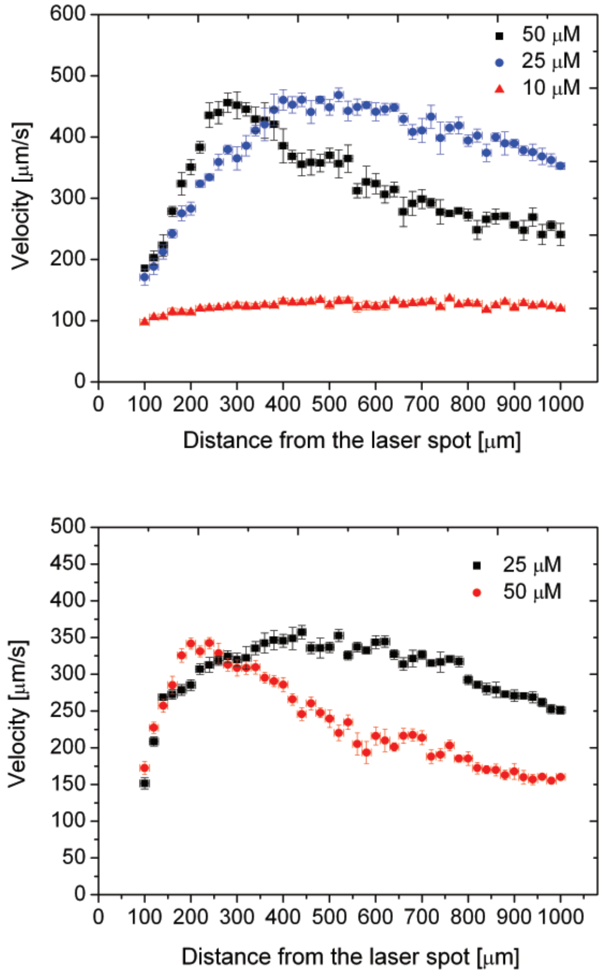

Fig. 6.15: Dependence of surfactant concentration on flow profile: (Top) at 5 mW and (Bottom) at 2.5 mW.

In general, it should be mentioned that the experiments presented here address the dynamic surface tension behavior of the system under study which is governed by a complex interplay of different processes, most importantly the adsorption/desorption kinetics of surfactants and their diffusion to the surface [125]. However, presumably with the exception of the squeezing out of *cis* surfactants from an overcrowded surface, these processes become relevant on time scales much larger than those considered here [172]. Fig. 6.15 (Bottom) shows the flow profile at a laser power of 2.5 mW. Nature of the velocity profile is similar to that of shown in fig. 6.15 (Top), but the overall velocity was decreased. This reduction in velocity can be attributed in terms of photoisomerization time scale.

6.6 Particle manipulation using optically-induced Marangoni flow

In this section, two potential applications of optically-induced Marangoni flow is demonstrated: particle trapping and particle manipulation.

To prove the trapping was not based on optical forces, the following experiment was performed. The 325 nm laser beam focused at the air-water interface (without surfactant), then a single particle (15 μm polystyrene particle) was moved towards the laser spot using the a translational stage. The translational stage was moved with a low velocity (10 $\mu m/s$), and it was observed that the particle was not staying at the laser focus, it followed the motion of the stage. It is reported that optical trapping is not possible if NA < 0.8 [145]. NA of the lens used is calculated using the equation $NA = n_m d_{beam}/2f_{lens}$. Substituting the values of the parameters ($n_m = 1$, $d_{beam} = 1$ cm and $f_{lens} = 10$ cm), yields a value of about 0.05. Clearly, this low NA lens is not sufficient to generate large optical gradient required for optical trapping.

To demonstrate the ability of the hydrodynamic trap to manipulate the position of the trapped particle, the following experiment was performed. Irradiation with focused 325 nm beam induces inward flow directed toward the laser focus. Particles (15 μm in diameter) adsorbed at the interface get dragged towards the focus and gets stably trapped at the focal region. Manipulation of the trapped particle can be achieved by tilting the manually adjustable mirrors M1 or M2. In that way, position of the laser focus can be moved over the liquid surface. It was observed that, the particle follows the motion of the laser spot. Fig. 6.16 (Top) shows the particle trajectory as a series of individual frames with a temporal offset of 10 s (extracted from the recorded video). From the trajectory the particle velocity as a function of distance along its path was computed using Nikon NIS elements software, as shown in fig. 6.16 (Bottom).

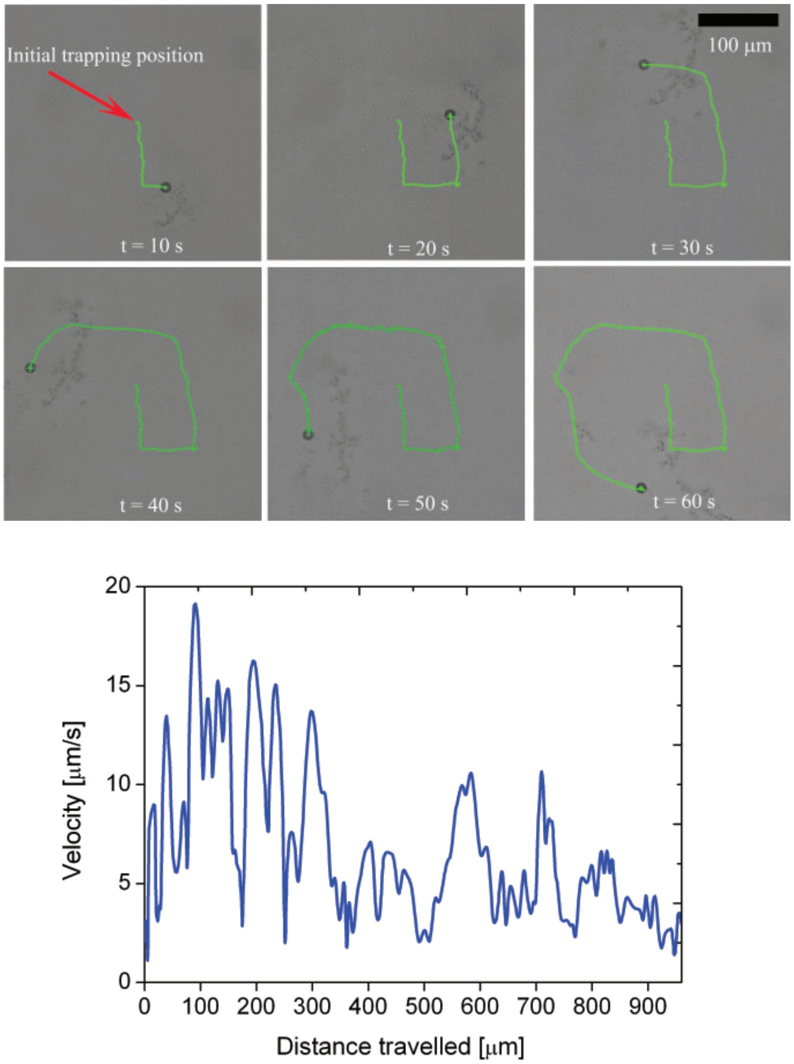

Fig. 6.16: Particle manipulation using optically-induced Marangoni flow: (Top) Sequence of images showing the particle trajectory after different time spans. The motion was induced by tilting the mirror guiding the laser beam. (Bottom) Particle velocity as a function of the distance traveled.

In that case a maximum particle velocity of about 15 $\mu m/s$ was obtained. When the mirror was tilted faster and the laser spot moves at about 20 $\mu m/s$, the particle was no longer able to follow its motion. This can be explained on the fact that the velocity at which particle experience near the focal spot is reduced due to the surfactant crowding around the focal spot makes the particle motion slower. Computing the Stokes drag force acting on the particle using the expression, $F_{drag} = 6\pi\mu R v$, where R is the particle radius and v is the velocity of the particle (here, it is 15 $\mu m/s$) yields a value of 2.11 pN. Comparing with the optical tweezers, one can see that optical tweezers require about 10^3 times higher intensity than that of used here to achieve pN forces. Additionally, optical tweezers require tightly focused laser beam to achieve stable trapping. In the present case, a moderately focused beam with very low NA was used for the experiments.

6.7 Summary

This chapter describes the principle and the preliminary results of a novel particle trapping mechanism. In conclusion, it is shown that photoresponsive surfactants allow creating dilatational flows at a liquid surface whose direction can be reversed by switching the laser wavelength. The flow patterns can be utilized to trap small particles at lower light intensities than with conventional optical tweezers. The favorable force scaling with the particle diameter makes this a promising principle for the manipulation of nanoscale objects. Up to now macro-molecules are being handled indirectly in a focused laser beam by attaching them to micrometer-sized particles. Sparing the need to link the molecules to such large objects could greatly enhance the flexibility of optical manipulation techniques.

7 Light-induced wettability studies of PNIPAM thin films

7.1 Introduction

Digital microfluidics refers to the manipulation of discrete droplets. Open surface digital microfluidics is an emerging field with potential applications in medicine and biological analysis. Droplet manipulation along the free surface has been achieved using several methods such as electrowetting [13], thermocapillarity [14], dielectrophoresis [3], magnetic force [15] and thermo-chemical effect [16]. Over such methods, light as stimuli have several advantages like non-contact, non-destructive and parallel manipulation. Additionally, they allow programmed optical pattern over the surfaces. Methods like opto-electrowetting [89], opto-thermocapillarity [102] and photochemical effect [9,10] have proposed for driving the droplet over the surface. These methods require either complex pattern of electrodes, strongly absorbing medium or a specific chemical protocol to achieve the droplet manipulation. Motivation of this work is to realize droplet manipulation on a thermo-sensitive polymer coated on a UV absorbing substrate.

This chapter describes the studies on light-induced wettability studies using polymer films. The first part discusses the basic theory behind the wettability and droplet movement. The second part provides the properties of the polymer material, experimental techniques and the results.

The contact angle gives the ability of a liquid to spread when it is placed on a surface. It is also called as the wetting angle. Young equation gives the equilibrium contact angle (θ_Y) based on three parameters: the solid - liquid interfacial tension (σ_{SL}), the solid - vapor interfacial tension (σ_{SV}) and the liquid - vapor interfacial tension (σ_{LV}). Young equation is represented as [161]:

$$\sigma_{LV} \cos\theta_Y = \sigma_{SV} - \sigma_{SL} \tag{7.1}$$

Fig. 7.1 schematically illustrates this physical scenario.

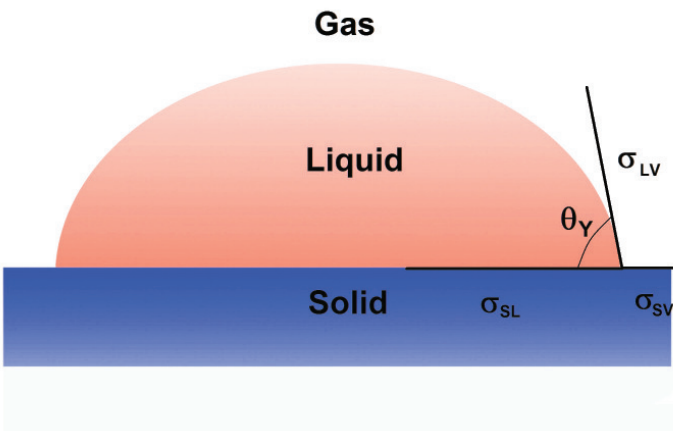

Fig. 7.1: Liquid-solid-gas contact angle.

A surface can be classified on the basis of its wettability: the hydrophilic surface and the hydrophobic surface. As the name suggest, water wets the hydrophilic surface more than that of hydrophobic surface. A surface is called as hydrophobic, when the equilibrium contact angle is higher than 90^o. If the contact angle is less than 90^o, the surface is referred to as hydrophilic. Fig. 7.2 illustrates the classification of the surfaces based on the equilibrium contact angle.

Young equation is based on the assumptions that the solid surface is smooth and chemically inert. As a result, one expects a unique contact angle for a system, but in practice, a range of contact angles is usually obtained. The upper limit of the contact angle is called the advancing contact angle (θ_A), and the lower limit is the receding contact

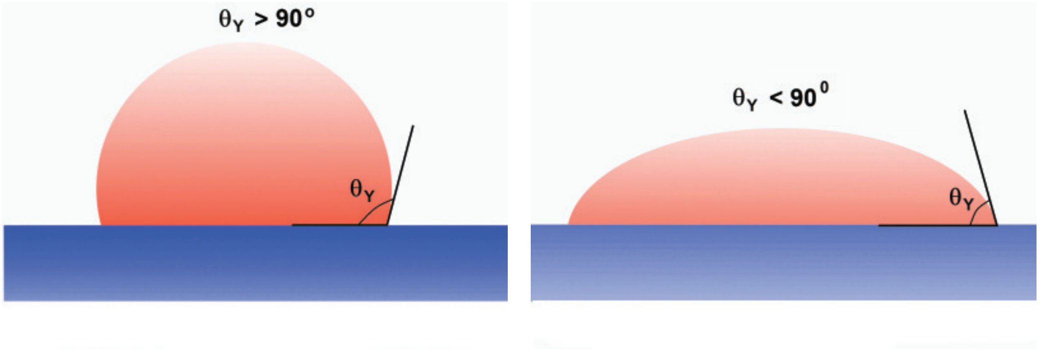

Fig. 7.2: Classification of surfaces based on wetting angle: (Left) the hydrophobic surface and (Right) the hydrophilic surface.

angle (θ_R). The difference of the advancing and the receding contact angles gives the contact angle hysteresis:

$$\Delta\theta_h = \theta_A - \theta_R \tag{7.2}$$

Studies attributed the origin of the hysteresis contact angle as surface heterogeneity, surface roughness or surface swelling [161, 201].

7.3 Poly(N-isopropylacrylamide) (PNIPAM) polymer

Environmental sensitive smart materials have enormous applications in the field of chemical separations, drug delivery, sensors, catalysis and fabrication of lab-on-a-chip devices [202–206]. Such materials exhibit chemical or physical transitions upon the action of stimuli. The external stimuli can be light, pH, temperature, electric field and magnetic field. They are very good candidates for making tunable microfluidic devices. Among such materials, Poly(N-isopropylacrylamide) (PNIPAM) is a widely used material [207, 208]. PNIPAM exhibits a Lower Critical Solution Temperature (LCST) in water. PNIPAM undergoes a reversible phase change at room temperature, around 32 ^oC. In its solution state, PNIPAM changes its optical transparency according the temperature. In its solid form, i.e., thin films or gels, PNIPAM undergoes changes in its surface properties such as wettability and surface roughness. Below LCST, the PNIPAM layer is hydrophilic due to the intermolecular hydrogen bond formed between PNIPAM chains and water molecule. Above LCST, the layer is hydrophobic because of the intramolecular hydrogen bond formation between C=O and N-H groups of the PNIPAM chains [209, 210]. The material is in swollen state (hydrophilic) below LCST and in deswollen state (hydrophobic) above LCST. Thus, contact angle of a water drop placed on such a surface depends on the temperature of the surface as shown in fig. 7.3.

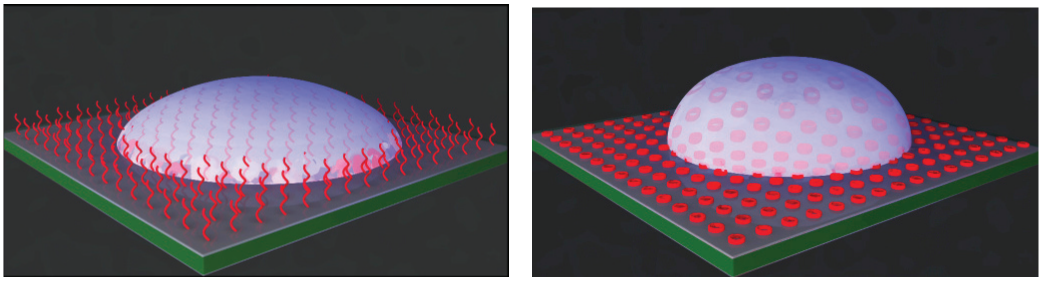

Fig. 7.3: Schematic representation of the wettability of the PNIPAM film: (Left) below the LCST and (Right) above the LCST.

7.4 Principle of light-induced motion of a liquid drop over the PNIPAM surface

Principle of light-induced wettability change relies on the phase transition of temperature sensitive (PNIPAM) material grafted on a UV absorbing glass substrate. The temperature rise of the glass substrate is governed by the equation $\Delta T = P_{in}\alpha_{abs}t/mC_p$, where α_{abs} is the absorbance of the sample and C_p specific heat capacity of the material. This formula gives the upper limit of the temperature rise where the heat loss to the surrounding medium is not considered. In the practical cases, the temperature rise will be smaller than the theoratically estimated value. The absorption of UV photons by the glass substrate rises the temperature above the LCST of the PNIPAM layer. At this state, water drop placed on PNIPAM film exhibits higher contact angle. Upon locally cooling one side of the droplet creates a wettability gradient over the surface. A liquid drop can move over a surface if it is subjected to a wettability gradient. Here, the contact angle at each side of the drop differs from its equilibrium value as shown in fig. 7.4.

This leads to an imbalance in the horizontal capillary force that results in a pulling force given by [90]:

$$F_c = L_d \sigma_{LV}(cos\theta_r - cos\theta_a) \tag{7.3}$$

where θ_r and θ_a represents the contact angle of the either side of the drop as shown in fig. 7.4. L_d represents the length between the front and rear ends of the drop. This capillary force is responsible for the spreading or retraction of the droplet on the substrate.

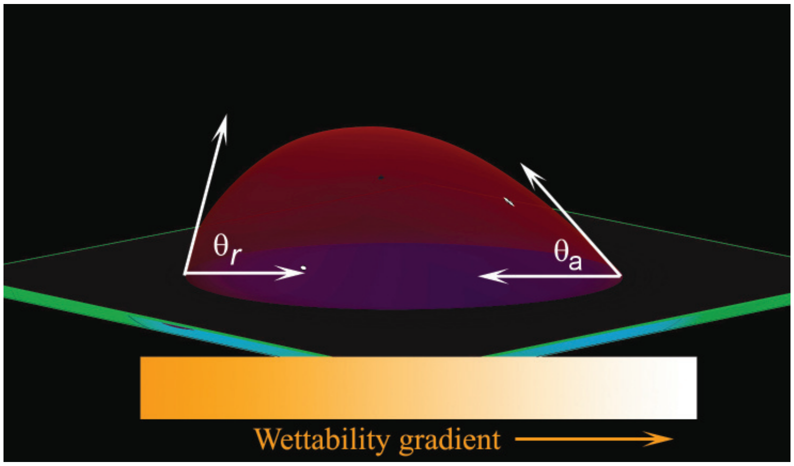

Fig. 7.4: Schematic representation of a droplet placed on a surface with a wettability gradient

The motion of a droplet on a surface depends on the hysteresis of the contact angles that pin the drop edge. To move a droplet along a surface, the difference in contact angle on either side of the drop must be higher than the hysteresis contact angle:

$$\Delta\theta_{drop} > \Delta\theta_h \tag{7.4}$$

where $\Delta\theta_{drop}$ refers to the difference in contact angle of the either side of the drop.

7.5 Experiments for determining the LCST of the film

Contact angle measurements were performed using Kruss DSA 100 model drop shape analysis system. This setup consist of software controlled motorized syringe system, imaging camera, bright light illumination source and a platform to keep the sample as shown in fig. 7.5. The camera records video at a frame rate of 40 fps. DSA software allows both the static and the dynamic contact angle measurements. Both these methods were adopted in this work. A 1 ml syringe with a needle of inner diameter 0.4 mm was used for dispensing the water drop over the surface.

A Newport temperature controller (Model 3040) was used for controlling the temperature of the PNIPAM sample. The controller was connected to a copper plate equipped with a temperature sensor (NTC 2 - wire thermistor) and a Peltier element (type TEC1-7105). Experimental procedure followed to determine the LCST of the film is as follows. The PNIPAM film (coated on glass substrate) was placed on the copper plate,

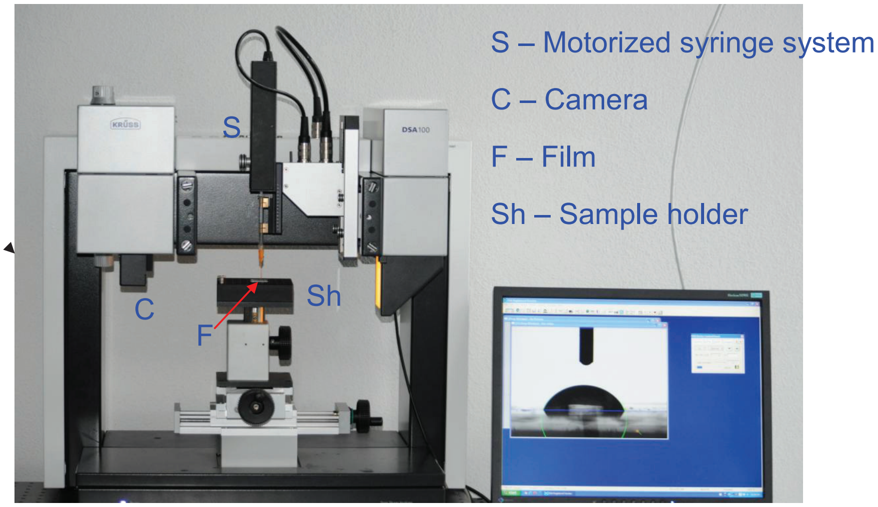

Fig. 7.5: Photograph of the contact angle measurement system.

and the temperature of the plate was set at 20 ^{o}C. Then a 3 μl water drop (Milli Q water) was placed on the PNIPAM film using the motorized syringe. The contact angle of the water drop was then measured to be 53 $\pm$ 3^{o}. Experiments were repeated for five individual measurements, and the standard deviation was calculated. The contact angle measurements were repeated at various temperature ranging from 20 ^{o}C to 35 ^{o}C. At each temperature, the contact angle of the water drop was determined which is shown in fig. 7.6. The contact angle of the water drop at 35 ^{o}C was measured to be 78 $\pm$ 2^{o}. It was observed that, after an initial increase in contact angle with temperature, the contact angle remains the same (78 $\pm$ 2^{o}C) above the temperature of 26 ^{o}C. From these measurements, it was concluded that the PNIPAM films undergoes phase transition from a swollen state to deswollen state between the temperature 24 - 26 $\pm$ 2 ^{o}C. Fig. 7.7 shows the image of a water drop placed on the PNIPAM substrate at 20 ^{o}C and 35 ^{o}C respectively.

Experiments were also performed on PNIPAM coated silicon substrate. Fig. 7.6 shows the variation in contact angle with temperature for PNIPAM coated glass (black symbol) and silicon substrate (red symbol) respectively. Both the films showed a transition in contact angle around a temperature of 26 $\pm$ 2^{o}C. From this result, it is attributed that substrate has no significant influence in wettability properties of the PNIPAM layer. To study the effect of the thickness of the PNIPAM film on the surface wettability, experiments were performed with samples having three different thickness. Table. 7.1 summarize the contact angle change of all the films. Among the films studied, films

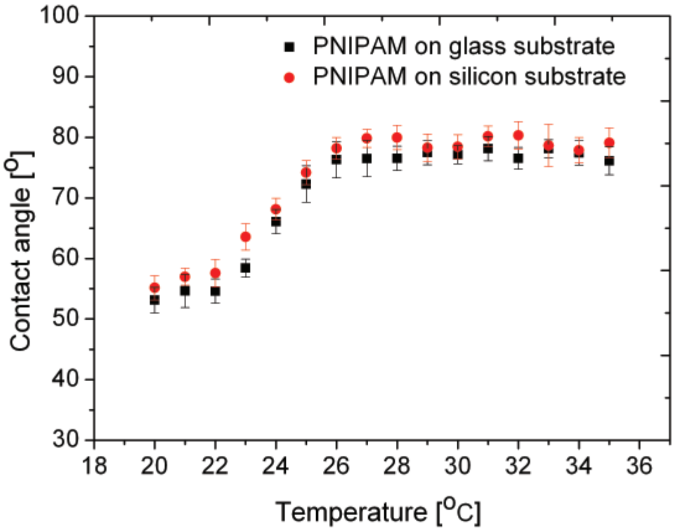

Fig. 7.6: Graph showing the contact angle of PNIPAM films as a function of the substrate temperature.

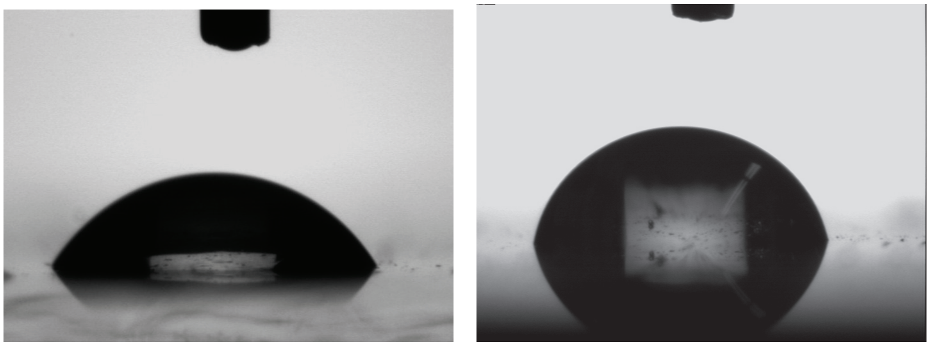

Fig. 7.7: Images of the water drop placed on the PNIPAM layer: (Left) at substrate temperature 20 ^{o}C and (Right) at 35 ^{o}C.

with 36 nm thickness showed the maximum difference in contact angle above and below the LCST. So this film was selected for the experiments explained in the coming sections. Repeatability of the phase transition of the PNIPAM surface was analyzed by repeating the contact angle measurements at a temperature above and below the LCST on the same spot of the film for 10 cycles. Fig. 7.8 shows the result of such an experiment.

Thickness (nm)	at 35 ^{o}C	at 20 ^{o}C
36	78 ± 2^o	53 ± 2^o
34	76 ± 2^o	55 ± 4^o
27	73 ± 3^o	58 ± 4^o

Table 7.1: Table showing the water contact angle for films having different thickness.

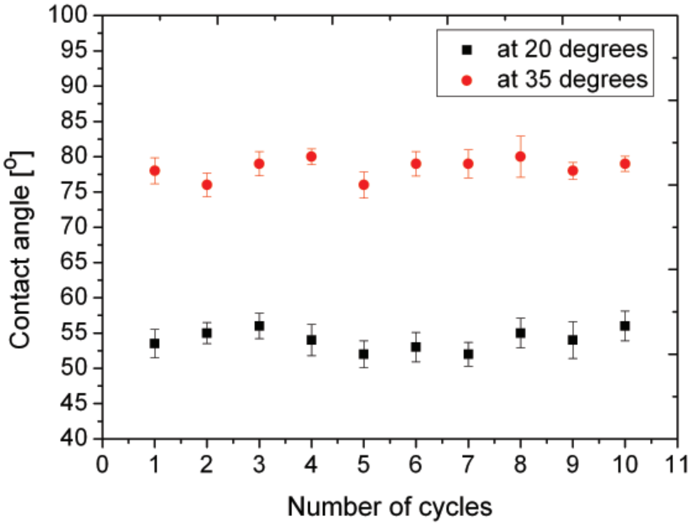

Fig. 7.8: Graph showing the repeatability of phase transition of the PNIPAM film.

7.6 Measurement of hysteresis contact angle

The advancing contact angle was determined by increasing the volume of the drop at a flow rate of 15 μl/m. The advancing contact angle is the contact angle at which the three phase line of the drop starts to move, i.e., the contact angle at which the the droplet starts spreading. The receding contact angle was measured by reducing the droplet volume at a flow rate of 15 μl/m. The receding contact angle corresponds to the retrieval of the three phase line. The experiments were performed at 35 ^{o}C and 20 ^{o}C. Fig. 7.9 shows the images recorded at the advancing and the receding position of the drop at 35 ^{o}C. The advancing contact angle at 40 ^{o}C was measured to be 84 $\pm$ 2^o and the receding contact angle was 23 ± 4^o. The difference between these two values gives the hysteresis contact angle. The PNIPAM surface shows a large hysteresis of about 60^o above the LCST.

Similarly, the experiments were performed at 20 ^{o}C. Here, the advancing contact angle was measured to be 64 ± 3^o and the receding contact angle was about 21^o. This yields

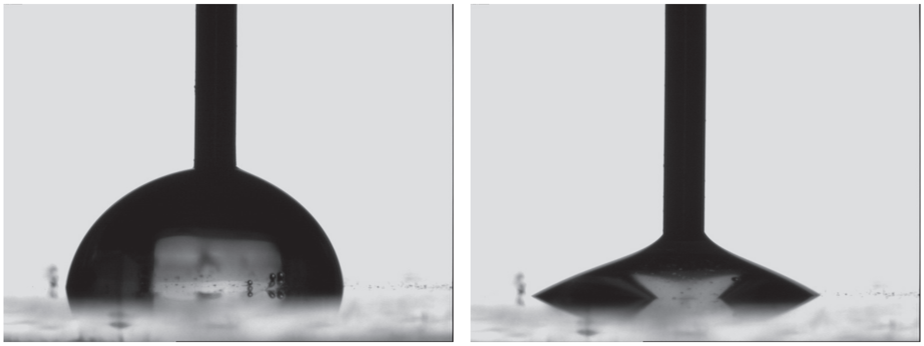

Fig. 7.9: Hysteresis contact angle measurement at 35 ^{o}C: (Left) the advancing contact angle and (Right) the receding contact angle.

a hysteresis contact angle of more than 40^{o}. It should be noted that the receding contact angle of the film was nearly independent of the temperature. To confirm this behavior, the following experiment was performed. Initially, the film temperature was kept at 20 ^{o}C. A 3 μl water drop was placed over the surface. The equilibrium contact angle was measured to be 53 ± 2^{o}. The substrate temperature was increased in steps till the temperature reaches at 35 ^{o}C. It was observed that, there was no change in the base line diameter of the water drop shows that the receding contact angle is independent of the temperature. In another experiment, initially the substrate was kept above the LCST temperature, then a drop was placed on the surface. Thereafter, the substrate temperature was decreased below the LCST, and it was observed that the three phase line of the drop starts spreading near the LCST temperature. The large hysteresis in contact angle of the PNIPAM film can be either due to physical or chemical inhomogeneities of the surface. Some studies reports that, once PNIPAM molecule is in contact with the water, even though the temperature rises above the LCST, the hydrogen bond formed between the water molecules and PNIPAM chains remains [211–214].

7.7 Light-induced wettability measurements

The motivation behind this study was to achieve droplet motion controlled by light. For that, the temperature of the PNIPAM sample was controlled by the absorption of light. The absorption spectrum of the glass substrate having thickness of 0.5 mm was measured for UV-VIS region using Specol 2000 spectrometer (Analytic Gena, Germany). The absorption spectra of both the glass and glass with PNIPAM was recorded which is shown in fig. 7.10. Both the curves show similar absorption behavior indicating that PNIPAM has no significant absorption in the UV-VIS region.

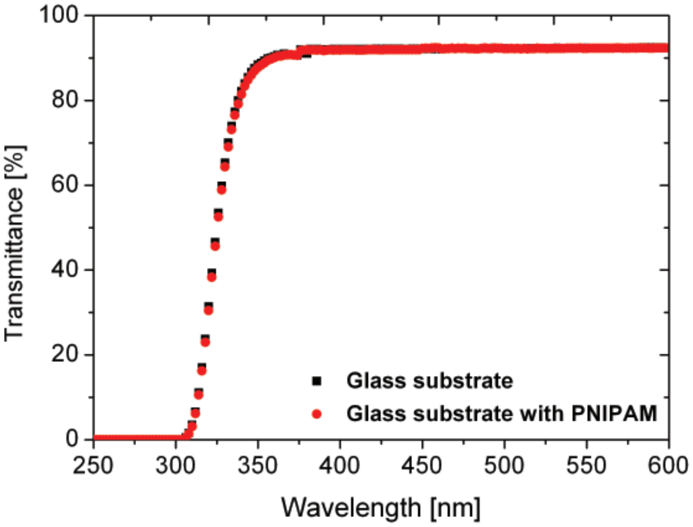

Fig. 7.10: Absorption spectra of the the glass substrate.

The glass shows a strong variation in absorbance with the wavelength in the UV range. The light source used for this experiment was Hamamastu UV lamp with a UV filter (type A9616-03). The temperature measurements at the sample were performed using a LabVIEW controlled thermocouple (type K). The UV lamp and the thermocouple were incorporated in to DSA 100 model contact angle measurement instrument. The UV lamp was switched on (at an intensity of 100 mW/cm^2 at the sample) till the temperature of the sample raises to 35 ^{o}C, then a 3 μl water drop was placed on the PNIPAM film. UV lamp was switched off and the film was allowed to cool down to the room temperature. The spreading mechanism was captured using the camera at a frame rate of 40 fps. Fig 7.11 (Left) shows a typical graph for the change in contact angle as a function of the cooling time. A small decrease in contact angle was observed before the sharp change in contact angle. The sharp decrease in contact angle is corresponds to the phase transition of the PNIPAM film from the hydrophobic state to the hydrophilic state. To understand the decrease in contact angle in the initial stage, the variation in base diameter of the drop as a function of the cooling time was analyzed. Fig. 7.11 (Right) shows the variation in drop diameter as a function of temperature. From the graphs, it was attributed that, the initial decrease in contact angle was due to the evaporation of the water drop, not due to the wettability change.

The normal cooling process took around 60 s to decrease the temperature from 35 ^{o}C to 20 ^{o}C. To speed up the cooling process, a compressed air cylinder with a 1 mm nozzle was used. In this way, a temperature decrease of 15 ^{o}C (from 35 ^{o}C to 20 ^{o}C) was

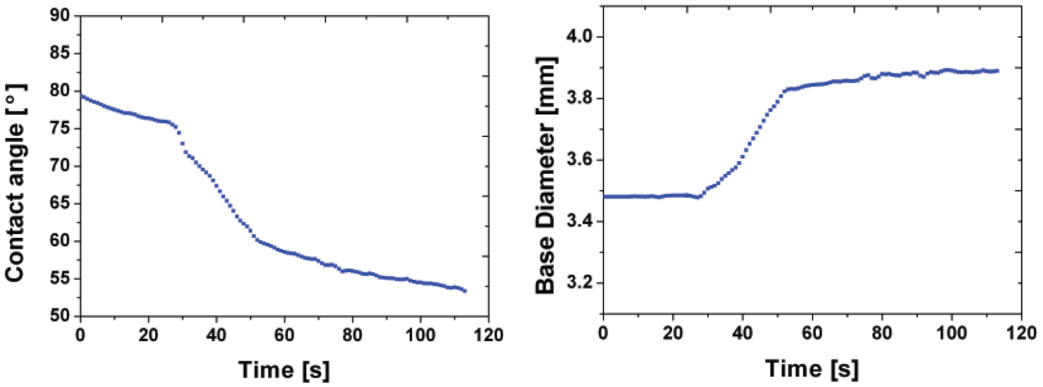

Fig. 7.11: Light-induced wettability measurements: (Left) Variation in water contact angle with cooling time and (Right) Variation in base diameter of the drop with cooling time.

achieved in 2 s. Fig. 7.12 shows the change in contact angle as a function of cooling time.

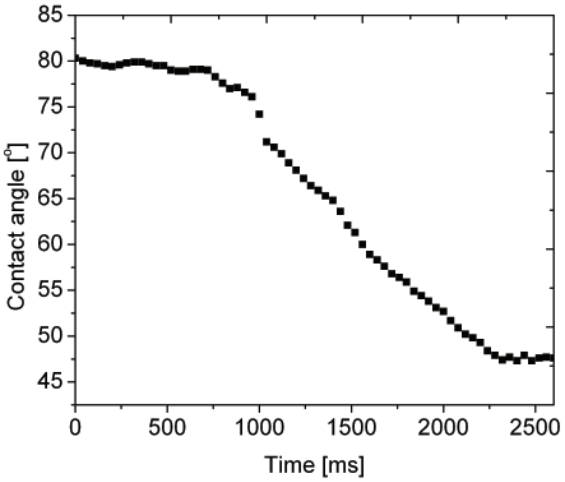

Fig. 7.12: Graph showing the contact angle measurement by cooling method.

7.8 Experiments for the droplet movement over PNIPAM substrate

The schematic of the experimental setup used for the droplet manipulation experiment is shown in fig. 7.13. Initially, the substrate was kept above the LCST temperature by UV irradiation. Then a 3 μl drop was placed on the PNIPAM layer. Thereafter, one side of the drop was cooled locally using the compressed air nozzle. Fig. 7.14 shows the variation in contact angle on advancing and receding edge of the drop as a function of spreading time. Due to the wettability gradient, the droplet spreads towards

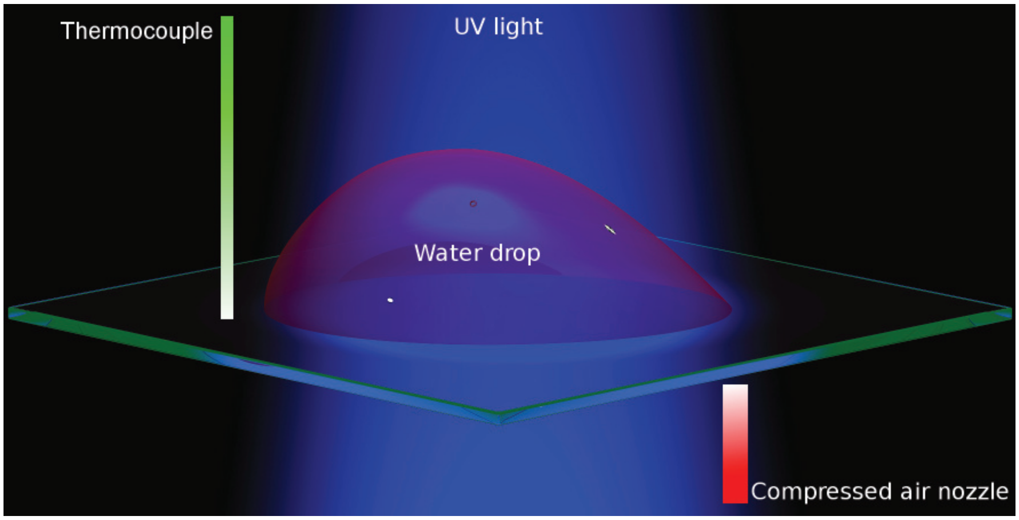

Fig. 7.13: Schematic diagram of the experimental setup used for light-induced droplet manipulation.

the colder region as shown fig. 7.15. But the other side of the drop was pinned at the contact line due to the high hysteresis contact angle. It can be seen that, the contact angle at the advancing edge reaches to about 43^o and that of the receding edge reaches to about 54^o.

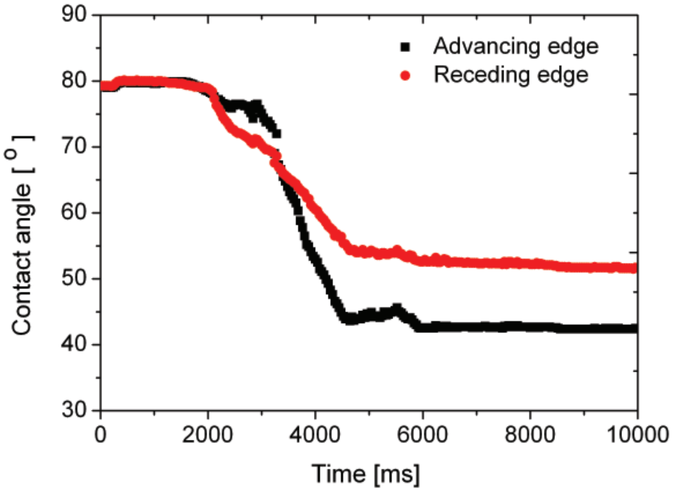

Fig. 7.14: Graph showing the contact angle at receding and advancing edge of the drop.

Now considering eq. 7.3, the horizontal capillary force responsible for the droplet motion depends on the change in contact angle. Another critical condition to be satisfied is, the difference in contact angle on either side of the drop must be higher than the

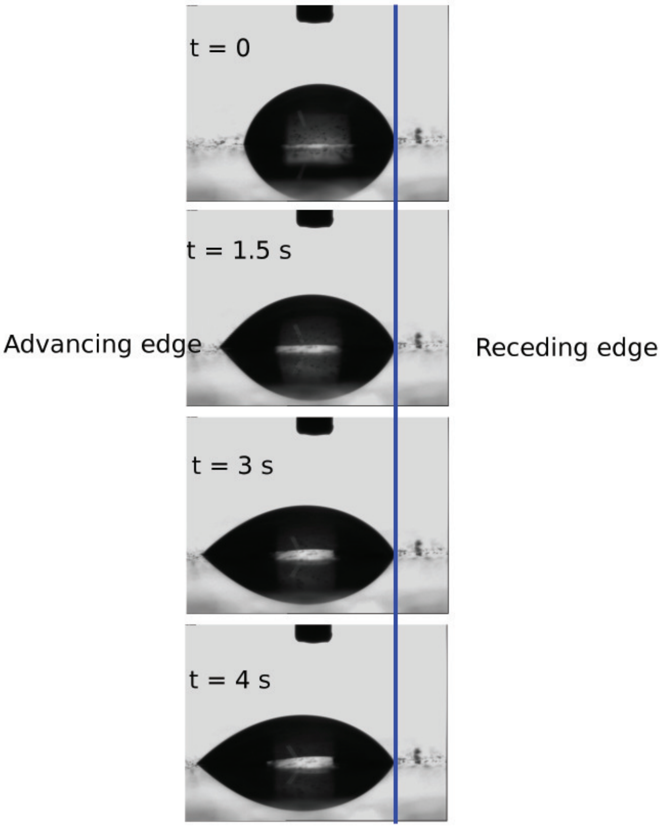

Fig. 7.15: Images showing the droplet spreading towards the colder region.

hysteresis contact angle. It is observed that, the hysteresis in contact angle above LCST is more than 60^o. The difference in contact angle on either side of the drop is 10^o which is much less than the hysteresis contact angle. This explains why the droplet pins at the surface rather than moving. Some recent studies on PNIPAM coated nano-structured surfaces reports that hysteresis contact angle can be reduced to less than 4^o [17]. Such a material is suitable candidate for the droplet manipulation over the PNIPAM surface.

7.9 Summary

This chapter describes the wettability measurement of temperature sensitive PNIPAM polymer films. PNIPAM films were prepared on UV absorbing glass plate. Thus the temperature of the film was controlled using UV irradiation. A large difference in contact angle of about 25^o was observed below and above LCST. Localized cooling method was employed to make the cooling process faster. Experiments were performed to drive the droplet over the surface by creating a wettability gradient over the surface. Large hysteresis in contact angle prevents the droplet movement.

8 Conclusion and future direction

The precise control over the movement and arrangement of small particles and liquid drops have enormous applications. To mention a few are study of single molecules in biology, transport of hazardous chemicals, mass transport along the interface and fabrication of tunable optical elements. Though several methods are available to achieve this goal, precise control and manipulation is a challenging work, especially as the size of the objects downs to nanometer regime. Among such methods, optical methods have unique advantages such as non-contact and single particle manipulation capability. Such optical methods also faces some fundamental limitations such as unfavorable force scale and high intensity requirement. To overcome such limitations, combination of optics with other prominent manipulation methods have been proposed. This Ph.D. thesis focuses on combining the properties of light and microfluidics, called Optofluidics to achieve particle and droplet manipulation. Optofluidics offers remote control and tunability. Additionally, the hydrodynamic nature of the force which scales to the diameter of the particle can be an advantage while handling small objects. The first part of the thesis describes the studies on light-induced particle manipulation techniques, and the second part discusses the studies on light-induced wettability manipulation.

Light-induced particle manipulation

Studies on light-induced particle manipulation are performed using two methods: Optical tweezers and Marangoni tweezers. This section summarizes the main outcome of the study with the future direction.

Optical trapping in microfluidic channel

This work focuses on size dependent study of microparticles trapped inside a microchannel. Influence of flow profile on the trapped particle is analyzed by comparing the escape force and maximum lateral displacement by performing the experiments at two flow conditions: with parabolic profile (inside the microfluidic channel) and uniform velocity profile (inside the sample chamber). Additionally, the influence of trapping at lower wavelength is studied. Main outcome of the study are,

1. Saffman lift force enhances the trapping performance for particles with intermediate size.

2. Maximum lateral displacement of 0.81 R is achieved for larger particles by implementing 442 nm wavelength for optical trapping.

3. Experimentally measured trapping stiffness found to be in good agreement with the theoretical model.

4. From these studies, it is concluded that, flow profile has to be taken in to account while trapping particles inside a microfluidic channel. Influence of Saffman lift force can be vital while handling biological cells or deformable objects inside the microchannel.

Light-induced particle manipulation using Marangoni tweezers

A novel technique for trapping and manipulation of particles adsorbed at the air-water interface is demonstrated. The principle behind this trapping mechanism relies on the surface tension variation due to the photoswitching of photosurfactant molecules adsorbed at the air-water interface. The photoswitchable surfactant exhibits two isomeric states: a *trans* state and a *cis* state. When adsorbed at the interface, a *cis* rich surface exhibits higher surface tension than a *trans* rich surface. Upon irradiation with a 325 nm beam, molecules transforms from *trans* state to *cis* state resulting in an increase in surface tension at the illuminated area. This surface tension gradient generates a hydrodynamic flow direct towards the laser focus. This inward flow is used to trap the particle at the laser spot. Particle streak velocimetry is used to characterize the velocity profile at the air-water interface. Main outcome of this work is outlined below:

1. A smart interface is constructed using photoswitchable surfactants.

2. Capability of the smart surface for the trapping and manipulation of microparticles adsorbed at the air-water interface is demonstrated.

3. Detailed analysis on velocity profile shows that the maximum velocity occurs at larger radial distance from the laser focus. This observation is attributed to the surfactant crowding near the focal region due to the inward flow.

4. Particle trapping and manipulation are achieved at 10^3 times lesser intensity than the optical tweezers.

5. It is experimentally shown that, the direction of the flow can be reversed by switching the illumination wavelength from 325 nm to 442 nm. The following section provides a brief comparison between Marangoni tweezers and the conventional trapping methods.

Advantages of particle trapping using optically-induced Marangoni flow

There are several advantages for optically-induced Marangoni trap over conventional optical trapping methods. They are,

1. Trapping of nanoparticles using conventional optical tweezer is a challenging task because the trapping force scales to the third power of the particle diameter, so the trapping force rapidly diminishes with a decrease in particle diameter. In the case of Marangoni trap, particles are trapped by hydrodynamic force instead of optical forces. This implies a force scaling with the particle diameter instead of the third power of the particle diameter, which opens up the perspective to manipulate nanoscale objects at moderate light intensities.

2. Commonly employed optical manipulation techniques rely on gradient forces generated by high numerical aperture microscope objective lens at high laser intensity. Manipulation using Optically-induced Marangoni tweezer is achieved with a moderately focused laser beam.

3. All the optical manipulation techniques rely on the properties of the particle such as their refractive index, polarizability and absorbance. Here, particles are trapped using hydrodynamic forces, so optical properties of the particles are less important.

4. Furthermore, when distributing the light intensity over an optical landscape as in the case of holographic optical tweezers, each of the individual traps of a tweezer array only shares a fraction of the photon flux of the laser beam. Therefore, since a specific threshold intensity is required to manipulate small objects, there is only a limited flexibility in creating different optical landscapes with a laser of given power. Here, Marangoni tweezer creates a potential landscape which extends over some millimeters with a single light beam.

Light-induced droplet manipulation

Research on light-induced wettability aims at fast movement of water drop placed on a temperature sensitive polymer material (PNIPAM). PNIPAM material is coated on a UV absorbing glass substrate. PNIPAM undergoes phase transition from a hydrophilic to a hydrophobic phase around a temperature of 26^{o}C. The temperature of the substrate is controlled by the UV irradiation. By implementing a localized cooling method, a fast wettability change of about 25^{o} is achieved in 2 s. Such a substrate is used for the experiments performed for the droplet movement. This experiment is performed by keeping the temperature of the substrate above the phase transition temperature of the PNIPAM, then locally cooling one side of the drop, thus creating wettability change over the surface. Though a fast spreading towards the colder region is achieved in 2 s, a large hysteresis contact angle prevents the droplet movement towards the colder region.

Future direction

One of the work presented in this thesis demonstrates a novel method for the manipulation of particles using optically-induced hydrodynamic flow. Conventional particle manipulation techniques such as optical tweezers, dielectrophoresis and opto-electronic tweezers rely on so-called gradient force which scales to the third power of the particle diameter. As a result, nanoparticle manipulation is challenging with conventional techniques. The hydrodynamic nature of the optically-induced Marangoni tweezer scales linearly to the particle diameter, which can be more efficient while handling nanoparticles. The current experimental setup and the flow profile diagnostic methods has to be modified to achieve this goal. The present work adopts a proof of principle experimental setup and diagnostic method for analyzing the velocity profile. On incorporating, an aberration free (both spherical and chromatic) lens can significantly enhance the trapping performance of the Marangoni tweezers. Another potential application of this method is parallel manipulation of particles over a wide area. Here, a potential landscape ranging in millimeter order can be created with a single light source. Incorporating diffractive optical elements with Marangoni tweezer setup can open a new field for the parallel manipulation. Additionally, Marangoni tweezers works at low intensity (about 10^3 times) than conventional optical tweezers, as result the handling of biological cells can be benefited by implementing Marangoni tweezers.

The section on light-induced wettability change using PNIPAM polymer is showing fast wettability change controlled by light. The large hysteresis contact angle prevents the droplet movement. The hysteresis contact angle can be reduced by preparing the PNI-

PAM layer on hydrophobic surfaces. Such a surface could prove to be effective for the droplet manipulation over the surface.

Appendix A

Photodegradation of Polystyrene particles at 442 nm

A specific particle is immobilized in three dimensions using 442 nm emission from the He-Cd laser. Such an image of the optically trapped particle with a size of 5 μm is shown in fig. A.1 (Left). However, after a certain residence time in the optical trap, the polystyrene particle exhibits luminescence as shown in fig. A.1 (Right). [1]

In the case of an optically trapped polystyrene particle, one can expect photodegradation due to the spatial localization of photon flux and the increase in temperature of the particle. Being a polymer with very low thermal conductivity 0.08W/mK [215], the observed luminescence in the present study may be a combined effect of localized temperature rise and photon induced damage in the polymer chain. The threshold energy required to break the αC-H bond without considering the radical stabilization is 71 kcal/mol [216]. But the stabilization of the αC-H radical species by a nearby double bond in the polystyrene backbone can significantly lower the activation energy for the production of the radical. The energy of the radiation employed in the present study corresponds to 65 kcal/mol (counting one photon per molecule), which is close to the isolated αC-H bond-breaking energy. Hence there is a high possibility that a αC-H bond near a double-bond on the back bone chain of polystyrene can be broken under irradiation at 442 nm. The high photon flux could provide the possibility that this event can occur with the phenyl group directly with impurities such as peroxides (oxygen incorporated into the polymer chain during the polymerization process), or regions of conjugation in the polymer. Thus bond stabilization in combination with high photon fluxes provides a means of generating polystyrene radicals as shown in fig. A.2.

The hydrogen radical formed in this way is free to move down in the polymer backbone to abstract a hydrogen atom from a second carbon atom. A lower energy state

---

[1] A part of this chapter is published in Journal of World Academy of Science, Engineering and Technology. Citation detals: Subramanyan Namboodiri V, Sajan D George, Steffen Hardt, Photodegradation of optically trapped polystyrene beads at 442 nm, World Academy of Science, Engineering and Technology 45 (2010)

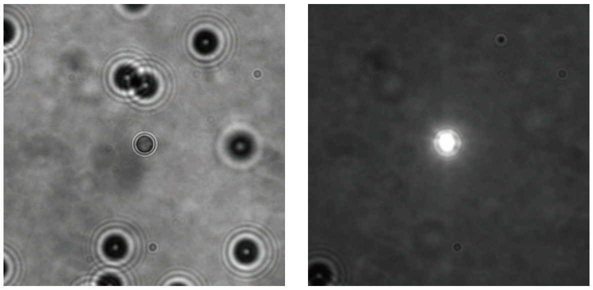

Fig. A.1: Optically trapped polystyrene particle: (Left) Immediately after trapping (Right) Exhibiting luminescence.

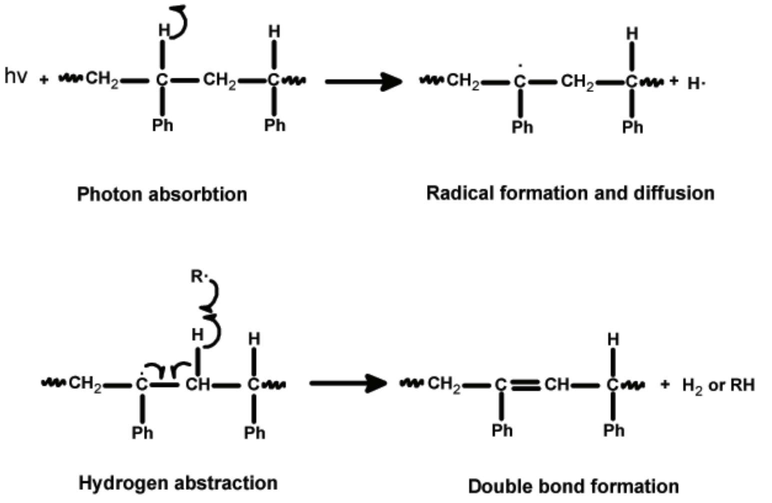

Fig. A.2: Photodegradation path of the polystyrene molecule

for hydrogen abstraction can be found in the vicinity of the double bond or conjugated region of the backbone since radicals are stabilized by resonance. The radical recombination results in the formation of a double bond in the backbone. This series of double bonds in the polymer chain is responsible for the observed luminescence. It has already been reported that a polymer backbone with more than six double bonds can produce a polyene chromophore with an emission wavelength greater than 500 nm [217]. The important feature to be noticed here is that this luminescence from the particle can be observed only after a finite residence time in the optical trap. Although the radical formation following photon absorption can be instantaneous, the diffusion of hydrogen radicals, the subsequent hydrogen extraction and double-bond formation require a certain amount of time. In order to understand the influence of the laser power on the initiation of luminescence, the particle is trapped with different power levels. The initiation time required to exhibit a visible luminescence in the CCD sensor is plotted as a function of input power at the back aperture of the microscope objective is shown in fig. A.3.

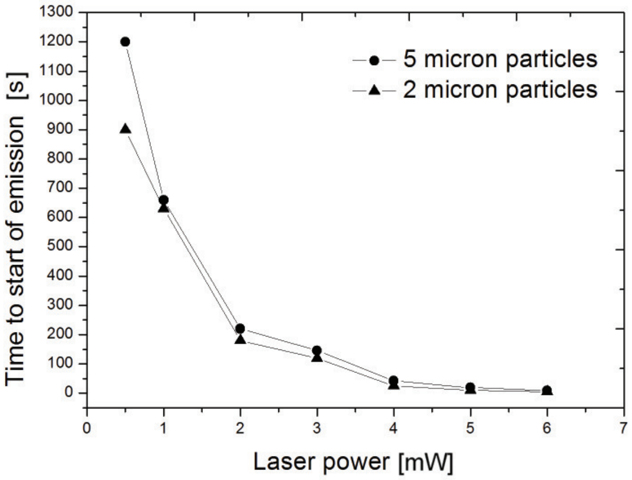

Fig. A.3: Effect of particle size and laser power on luminescence initiation time from optically trapped (at 442 nm) polystyrene particles.

It is clear from the fig. A.3 that for both types of particles, the initiation time decreases drastically (almost exponentially) with increasing laser power. At lower power levels, the particle size also plays an important role. In the case of optically trapped micron size particles, the particles are normally trapped away from the focal point at distance corresponding to the particle size. As a result, the 2 micron particles experiences large radiant flux density in comparison to the 5 micron particle. It has already been reported that the rate of production of hydrogen free radicals in the polystyrene molecule is proportional to the light intensity [217,218]. The higher rate of production of free hydrogen radicals results in shorter initiation time for the luminescence. The conventional reciprocity law ($I.t$ = constant), which states that the progress of a photochemical reaction mechanism depends only on the absorbed energy. i.e. the product of light intensity I and exposure time t, fails to apply to most reactions [219]. A more general relationship applying to the photodegradation of polymers is Schwarzchild´s law, reading $I^{\phi}t$ = constant, where is the ϕ Schwarzchild coefficient. The reported values of this coefficient for polystyrene under polychromatic illumination range from 0.6 to 0.75 [219]. Accordingly, in the case of an optically trapped polystyrene particle, the initiation time for the luminescence is given by, $t = KI^{-\phi}$ where K is a constant. This dependence explains the observed decrease of luminescence initiation time with increasing laser power. The difference in luminescence initiation time for particles with different sizes at low laser power levels can be explained in terms of the differential form of Schwarzchild´s law $\Delta t = K(-\phi)I^{-\phi-1}\Delta I$. As explained earlier, an optically trapped smaller particle experiences a high intensity. However since, $\Delta t \propto 1/I^{\phi+1}$, this difference decreases quiet rapidly with increasing laser power. This explains why both particles exhibit almost the same initiation time for the luminescence at 6 mW.

Appendix B

Materials

Synthesis of the photosurfactant

Synthesis of the photosurfactant material was done by Mrs. Martina Ewald and Prof. Dr. rer. nat. Markus Biesalski, Department of Chemistry, TU Darmstadt. The synthesis was based on ref. [181].

Step 1.

4-Butyl-4′-hydroxyl azobenzene was prepared by dissolving 14.9 g of 4-butylaniline in 64 mL of 5 M hydrochloric acid and reacting it with 15 mL of aqueous sodium nitrite (6.67 M) at 0^{o}C for 1 h. The resulting diazonium solution was then coupled with phenol in a slurry (9.4 g of phenol + 26.5 g of sodium carbonate + 50 mL of MilliQ water) at 0^{o}C for 1 h. The product was collected by filtration, dried in a vacuum oven overnight. The yield was 91 %.

Step 2.

4-Butyl-4′-(4-brom)butoxy azobenzene was prepared by first dissolving 10.08 g of *4-Butyl-4′-hydroxyl azobenzene* in 40 mL of THF and adding this solution drop wise to a mixture of 21.6 g of 1,4-Bromobutane, 4.49 g of potassium hydroxide, and 200 mL of THF. After 19h reflux solvent was removed, followed by column chromatography using eluent cyclohexane: ethylacetat = 7:3 to remove polar impurities, then 1,4-Dibromobutane excess was removed by vacuum destillation, recrystallization in 2-propanol. Yield 41%.

Step 3

diethyleneglycol mono(4',4-butyloxy,butyl-azobenzene))$C_4AzoOC_4E_2$. To prepare $C_4AzoOC_4E_2$, 3.89 g of sodium hydride was first reacted with 21.22 g of di(ethylene glycol) in 80mL of THF under N_2 protection for 2 h. A solution of 3.61 g of *4-Butyl-4′-hydroxyl azobenzene* with 40 mL of THF was added dropwise into this reaction mixture, and the resulting solution was refluxed for 64 h under N_2. The solvent was removed from the reaction mixture by rotary evaporation, and vacuum distillation was used to remove residual di(ethylene glycol). The product was separated by chromatography (60 Å silica, ethylacetat as the eluent). The yield was 51%.

Synthesis of the PNIPAM films

Synthesis of the PNIPAM polymer was done by Mr. Helge Schenderlein and Prof. Dr. rer. nat. Markus Biesalski, Department of Chemistry, TU Darmstadt.

P(NiPAM-Co-MABP) Polymer was synthesized by free radical copolymerization. For this, N-isopropylacrylamide (NIPAM) and Methacryloxybenzophenone (MABP) were dissolved in DMF. To this reaction mixture radical initiator Azoisobutyronitrile (AIBN) was added and reaction heated to 65 ^{o}C which resulted the P(NIPAM-Co-MABP) Polymer. Ratio between NIPAM and MABP units in polymer can be varied by change in NIPAM and MABP ratio in feed. Variation in the MABP content varies the crosslink-density of the networks formed.

Film deposition was performed by spin coating of polymer solutions in n-Butanol (2s 300rpm; 2s 500 rpm; 20s 3000 rpm). Films were prepared on silicon wafers and glass substrates equipped with a triethoxy-benzophenone-silane surface linker. In film deposition, copolymer with photocurable benzophenone side groups were illuminated with UV-light (λ = 365 nm; dose = 16 J/Cm^2), followed by soxlett extraction in acetone, resulted a network of P(NiPAM-Co-MABP) polymer on the substrate. Thickness of the films were measured using films coated on silicon wafers by nulling ellipsometry. Thickness of the films were varied by changing the P(NiPAM-Co-MABP) content.

List of figures

List of Tables

Bibliography

[1] D. G. Grier, “A revolution in optical manipulation,” *Nature*, vol. 424, no. 6950, pp. 810–816, 2003.

[2] A. Ashkin, J. M. Dziedzic, J. E. Bjorkholm, and S. Chu, “Observation of a single-beam gradient force optical trap for dielectric particles,” *Opt. Lett.*, vol. 11, no. 5, pp. 288–290, 1986.

[3] R. Pethig, “Review article-dielectrophoresis: Status of the theory, technology, and applications,” *Biomicrofluidics*, vol. 4, no. 2, pp. 022811–35, 2010.

[4] S. Kawata and T. Sugiura, “Movement of micrometer-sized particles in the evanescent field of a laser beam,” *Opt. Lett.*, vol. 17, no. 11, pp. 772–774, 1992.

[5] M. C. Wu, “Optoelectronic tweezers,” *Nat. Photonics*, vol. 5, no. 6, pp. 322–324, 2011.

[6] C. Monat, P. Domachuk, and B. J. Eggleton, “Integrated optofluidics: A new river of light,” *Nat. Photonics*, vol. 1, no. 2, pp. 106–114, 2007.

[7] D. Erickson, C. Yang, and D. Psaltis, “Optofluidics emerges from the laboratory,” *Photonics Spectra*, vol. 42, pp. 74–79, 2008.

[8] C. Pei-Yu, A. T. Ohta, A. Jamshidi, H. Hsin-Yi, and M. C. Wu, “Light-actuated ac electroosmosis for nanoparticle manipulation,” *J. Microelectromech. Syst.*, vol. 17, no. 3, pp. 525–531, 2008.

[9] K. Ichimura, S.-K. Oh, and M. Nakagawa, “Light-driven motion of liquids on a photoresponsive surface,” *Science*, vol. 288, no. 5471, pp. 1624–1626, 2000.

[10] A. Diguet, R.-M. Guillermic, N. Magome, A. Saint-Jalmes, Y. Chen, K. Yoshikawa, and D. Baigl, “Photomanipulation of a droplet by the chromocapillary effect,” *Angew. Chem. Int. Ed.*, vol. 48, no. 49, pp. 9281–9284, 2009.

[11] E. Higurashi, O. Ohguchi, T. Tamamura, H. Ukita, and R. Sawada, “Optically induced rotation of dissymmetrically shaped fluorinated polyimide micro-objects in optical traps,” *J. Appl. Phys.*, vol. 82, no. 6, pp. 2773–2779, 1997.

[12] S. L. Neale, M. P. MacDonald, K. Dholakia, and T. F. Krauss, “All-optical control of microfluidic components using form birefringence,” *Nat. Mater.*, vol. 4, no. 7, pp. 530–533, 2005.

[13] M. G. Pollack, R. B. Fair, and A. D. Shenderov, “Electrowetting-based actuation of liquid droplets for microfluidic applications,” *Appl. Phys. Lett.*, vol. 77, no. 11, pp. 1725–1726, 2000.

[14] V. Pratap, N. Moumen, and R. S. Subramanian, “Thermocapillary motion of a liquid drop on a horizontal solid surface,” *Langmuir*, vol. 24, no. 9, pp. 5185–5193, 2008.

[15] Y. Zhao, J. Fang, H. Wang, X. Wang, and T. Lin, “Magnetic liquid marbles: Manipulation of liquid droplets using highly hydrophobic fe_3o_4 nanoparticles,” *Adv. Mater.*, vol. 22, no. 6, pp. 707–710, 2010.

[16] C. Song, K. Kim, K. Lee, and H. K. Pak, “Thermochemical control of oil droplet motion on a solid substrate,” *Appl. Phys. Lett.*, vol. 93, no. 8, pp. 084102–3, 2008.

[17] J. Byun, J. Shin, S. Kwon, S. Jang, and J. K. Kim, “Fast and reversibly switchable wettability induced by a photothermal effect,” *Chem. Commun.*, vol. 48, no. 74, pp. 9278–9280, 2012.

[18] A. Ashkin, “Acceleration and trapping of particles by radiation pressure,” *Phys. Rev. Lett.*, vol. 24, no. 4, pp. 156–159, 1970.

[19] V. G. Shvedov, A. V. Rode, Y. V. Izdebskaya, A. S. Desyatnikov, W. Krolikowski, and Y. S. Kivshar, “Giant optical manipulation,” *Phys. Rev. Lett.*, vol. 105, no. 11, pp. 118103–4, 2010.

[20] F. M. Fazal and S. M. Block, “Optical tweezers study life under tension,” *Nat. Photonics*, vol. 5, no. 6, pp. 318–321, 2011.

[21] A. D. Mehta, M. Rief, A. Spudich, D. A. Smith, and R. M. Simmons, “Single-molecule biomechanics with optical methods,” *Science*, vol. 283, no. 5408, pp. 1689–1695, 1999.

[22] T. L. Gustavson, A. P. Chikkatur, A. E. Leanhardt, A. Görlitz, S. Gupta, D. E. Pritchard, and W. Ketterle, “Transport of bose-einstein condensates with optical tweezers,” *Phys. Rev. Lett.*, vol. 88, no. 2, pp. 020401–4, 2001.

[23] K. C. Neuman and S. M. Block, “Optical trapping,” *Rev. Sci. Instrum.*, vol. 75, no. 9, pp. 2787–2809, 2004.

[24] K. C. Neuman and A. Nagy, “Single-molecule force spectroscopy: optical tweezers, magnetic tweezers and atomic force microscopy,” *Nat. Methods*, vol. 5, no. 6, pp. 491–505, 2008.

[25] A. Ashkin, “Forces of a single-beam gradient laser trap on a dielectric sphere in the ray optics regime,” *Biophys. J.*, vol. 61, no. 2, pp. 569–582, 1992.

[26] S. P. Smith, S. R. Bhalotra, A. L. Brody, B. L. Brown, E. K. Boyda, and M. Prentiss, “Inexpensive optical tweezers for undergraduate laboratories,” *Am. J. Phys*, vol. 67, no. 1, pp. 26–35, 1999.

[27] J. Bechhoefer and S. Wilson, “Faster, cheaper, safer optical tweezers for the undergraduate laboratory,” *Am. J. Phys*, vol. 70, no. 4, pp. 393–400, 2002.

[28] W. M. Lee, P. J. Reece, R. F. Marchington, N. K. Metzger, and K. Dholakia, “Construction and calibration of an optical trap on a fluorescence optical microscope,” *Nat. Protocols*, vol. 2, no. 12, pp. 3226–3238, 2007.

[29] R. M. Simmons, J. T. Finer, S. Chu, and J. A. Spudich, “Quantitative of force and displacement using an optical trap,” *Biophys. J.*, vol. 70, no. 4, pp. 1813–1822, 1996.

[30] H. Felgner, O. Müller, and M. Schliwa, “Calibration of light forces in optical tweezers,” *Appl. Opt.*, vol. 34, no. 6, pp. 977–982, 1995.

[31] R. Pool, “Trapping with optical tweezers,” *Science*, vol. 241, no. 4869, p. 1042, 1988.

[32] J. A. Spudich, S. E. Rice, R. S. Rock, T. J. Purcell, and H. M. Warrick, “Optical traps to study properties of molecular motors,” *Cold Spring Harbor Protocols*, vol. 2011, no. 11, pp. 1305–1318, 2011.

[33] M. Dao, C. T. Lim, and S. Suresh, “Mechanics of the human red blood cell deformed by optical tweezers,” *J. Mech. Phys. Solids*, vol. 53, no. 2, pp. 2259–2280, 2005.

[34] J. R. Moffitt, Y. R. Chemla, S. B. Smith, and C. Bustamante, “Recent advances in optical tweezers,” *Annu. Rev. Biochem.*, vol. 77, no. 1, pp. 205–228, 2008.

[35] K. Svoboda and S. M. Block, "Optical trapping of metallic rayleigh particles," *Opt. Lett.*, vol. 19, no. 13, pp. 930–932, 1994.

[36] K. Takahashi, M. Ichikawa, and Y. Kimura, "Force between colloidal particles in a nematic liquid crystal studied by optical tweezers," *Phys. Rev. E*, vol. 77, no. 2, pp. 020703–4, 2008.

[37] S. Maruo and H. Inoue, "Optically driven viscous micropump using a rotating microdisk," *Appl. Phys. Lett.*, vol. 91, no. 8, pp. 084101–3, 2007.

[38] D. G. Grier and Y. Roichman, "Holographic optical trapping," *Appl. Opt.*, vol. 45, no. 5, pp. 880–887, 2006.

[39] M. Padgett and R. Di Leonardo, "Holographic optical tweezers and their relevance to lab on chip devices," *Lab on a Chip*, vol. 11, no. 7, pp. 1196–1205, 2011.

[40] K. T. Gahagan and G. A. Swartzlander, "Trapping of low-index microparticles in an optical vortex," *J. Opt. Soc. Am. B*, vol. 15, no. 2, pp. 524–534, 1998.

[41] A. T. O'Neil and M. J. Padgett, "Axial and lateral trapping efficiency of laguerre-gaussian modes in inverted optical tweezers," *Opt. Commun.*, vol. 193, no. 1-6, pp. 45–50, 2001.

[42] K. C. Neuman, E. H. Chadd, G. F. Liou, K. Bergman, and S. M. Block, "Characterization of photodamage to escherichia coli in optical traps," *Biophys. J.*, vol. 77, no. 5, pp. 2856–2863, 1999.

[43] U. Mirsaidov, W. Timp, K. Timp, M. Mir, P. Matsudaira, and G. Timp, "Optimal optical trap for bacterial viability," *Phys. Rev. E*, vol. 78, no. 2, pp. 021910–7, 2008.

[44] L. Novotny and B. Hecht, *"Principles of Nano-Optics"*. Cambridge University Press, NY, USA, 2006.

[45] D. Erickson, X. Serey, Y.-F. Chen, and S. Mandal, "Nanomanipulation using near field photonics," *Lab Chip*, vol. 11, pp. 995–1009, 2011.

[46] S. Kuriakose, D. Morrish, X. Gan, J. W. M. Chon, K. Dholakia, and M. Gu, "Near-field optical trapping with an ultrashort pulsed laser beam," *Appl. Phys. Lett.*, vol. 92, no. 8, pp. 081108–3, 2008.

[47] A. N. Grigorenko, N. W. Roberts, M. R. Dickinson, and ZhangY, “Nanometric optical tweezers based on nanostructured substrates,” *Nat. Photonics*, vol. 2, no. 6, pp. 365–370, 2008.

[48] L. Huang, S. J. Maerkl, and O. J. Martin, “Integration of plasmonic trapping in a microfluidic environment,” *Opt. Express*, vol. 17, no. 8, pp. 6018–6024, 2009.

[49] G. Volpe, R. Quidant, G. Badenes, and D. Petrov, “Surface plasmon radiation forces,” *Phys. Rev. Lett.*, vol. 96, no. 23, pp. 238101–4, 2006.

[50] A. Jonás and P. Zemánek, “Light at work: The use of optical forces for particle manipulation, sorting, and analysis,” *Electrophoresis*, vol. 29, no. 24, pp. 4813–4851, 2008.

[51] M. Siler, T. Cizmár, M. Serý, and P. Zemánek, “Optical forces generated by evanescent standing waves and their usage for sub-micron particle delivery,” *Appl. Phys. B*, vol. 84, no. 1-2, pp. 157–165, 2006.

[52] S. G. Bike, “Measuring colloidal forces using evanescent wave scattering,” *Curr. Opin. Colloid Interface Sci.*, vol. 5, no. 1-2, pp. 144–150, 2000.

[53] A. R. Hawkins and H. Schmidt, *“Handbook of Optofluidics”*. CRC Press, Taylor and Francis Group, 6000 Broken Sound Parkway NW, 2010.

[54] S. Kawata and T. Tani, “Optically driven mie particles in an evanescent field along a channeled waveguide,” *Opt. Lett.*, vol. 21, no. 21, pp. 1768–1770, 1996.

[55] M. Gu, J.-B. Haumonte, Y. Micheau, J. W. M. Chon, and X. Gan, “Laser trapping and manipulation under focused evanescent wave illumination,” *Appl. Phys. Lett.*, vol. 84, no. 21, pp. 4236–4238, 2004.

[56] C. D. Mellor, T. A. Fennerty, and C. D. Bain, “Polarization effects in optically bound particle arrays,” *Opt. Express*, vol. 14, no. 21, pp. 10079–10088, 2006.

[57] C. D. Mellor and C. D. Bain, “Array formation in evanescent waves,” *ChemPhysChem*, vol. 7, no. 2, pp. 329–332, 2006.

[58] S. Mohanty, “Optically-actuated translational and rotational motion at the microscale for microfluidic manipulation and characterization,” *Lab on a Chip*, vol. 12, no. 19, pp. 3624–3636, 2012.

[59] A. Jamshidi, A. T. Ohta, J. K. Valley, H.-Y. Hsu, S. L. Neale, and M. C. Wu, "Optofluidics and optoelectronic tweezers," *Proc. of the SPIE: MEMS, MOEMS, and Micromachining III.*, vol. 6993, pp. 69930A–10, 2008.

[60] R. Pethig, H. Ying, W. Xiao-bo, and J. P. H. Burt, "Positive and negative dielectrophoretic collection of colloidal particles using interdigitated castellated microelectrodes," *J. Phys. D: Appl. Phys.*, vol. 25, no. 5, pp. 881–888, 1992.

[61] G. H. Markx, M. S. Talary, and R. Pethig, "Separation of viable and non-viable yeast using dielectrophoresis," *J. Biotechnol.*, vol. 32, no. 1, pp. 29–37, 1994.

[62] A. Heeren, C. P. Luo, W. Henschel, M. Fleischer, and D. P. Kern, "Manipulation of micro- and nano-particles by electro-osmosis and dielectrophoresis," *Microelectron. Eng.*, vol. 84, no. 5-8, pp. 1706–1709, 2007.

[63] P. Y. Chiou, A. T. Ohta, and M. C. Wu, "Massively parallel manipulation of single cells and microparticles using optical images," *Nature*, vol. 436, no. 7049, pp. 370–372, 2005.

[64] S.-Y. Park, S. Kalim, C. Callahan, M. A. Teitell, and E. P. Y. Chiou, "A light-induced dielectrophoretic droplet manipulation platform," *Lab Chip*, vol. 9, no. 22, pp. 3228–3235, 2009.

[65] H. A. Pohl, "The motion and precipitation of suspensoids in divergent electric fields," *J. Appl. Phys.*, vol. 22, no. 7, pp. 869–871, 1951.

[66] A. Jamshidi, P. J. Pauzauskie, P. J. Schuck, A. T. Ohta, P.-Y. Chiou, J. Chou, P. Yang, and M. C. Wu, "Dynamic manipulation and separation of individual semiconducting and metallic nanowires," *Nat. Photonics*, vol. 2, no. 2, pp. 86–89, 2008.

[67] P. J. Pauzauskie, A. Jamshidi, J. K. Valley, J. J. H. Satcher, and M. C. Wu, "Parallel trapping of multiwalled carbon nanotubes with optoelectronic tweezers," *Appl. Phys. Lett.*, vol. 95, no. 11, pp. 113104–3, 2009.

[68] L. Oroszi, A. Dér, H. Kirei, V. Rakovics, and P. Ormos, "Manipulation of microfluidic flow pattern by optically controlled electroosmosis," *Microfluid. Nanofluid.*, vol. 6, no. 4, pp. 565–569, 2009.

[69] J. Moorthy, C. Khoury, J. S. Moore, and D. J. Beebe, "Active control of electroosmotic flow in microchannels using light," *Sens. Actuators, B*, vol. 75, no. 3, pp. 223–229, 2001.

[70] L. Oroszi, A. Der, H. Kirei, P. Ormos, and V. Rakovics, "Control of electro-osmostic flow by light," *Appl. Phys. Lett.*, vol. 89, no. 26, pp. 263508–3, 2006.

[71] X. Fan and I. M. White, "Optofluidic microsystems for chemical and biological analysis," *Nat. Photonics*, vol. 5, no. 10, pp. 591–597, 2011.

[72] D. Erickson, D. Sinton, and D. Psaltis, "Optofluidics for energy applications," *Nat. Photonics*, vol. 5, no. 10, pp. 583–590, 2011.

[73] A. J. Chung and D. Erickson, "Optofluidic waveguides for reconfigurable photonic systems," *Opt. Express*, vol. 19, no. 9, pp. 8602–8609, 2011.

[74] D. Mark, S. Haeberle, G. Roth, F. von Stetten, and R. Zengerle, "Microfluidic lab-on-a-chip platforms: requirements, characteristics and applications," *Chem. Soc. Rev.*, vol. 39, no. 3, pp. 1153–1182, 2010.

[75] B. J. Kirby, *"Micro- and Nanoscale Fluid Mechanics Transport in Microfluidic Devices"*. Cambridge University Press, 32 Avenue of the Americas, New York, NY 10013-2473, USA, 2010.

[76] M. I. Kohira, A. Isomura, N. Magome, S. Mukai, and K. Yoshikawa, "Optical levitation of a droplet under a linear increase in gravitational acceleration," *Chem. Phys. Lett.*, vol. 414, no. 4-6, pp. 389–392, 2005.

[77] N. Jordanov and R. Zellner, "Investigations of the hygroscopic properties of ammonium sulfate and mixed ammonium sulfate and glutaric acid micro droplets by means of optical levitation and raman spectroscopy," *Phys. Chem. Chem. Phys.*, vol. 8, no. 23, pp. 2759–2764, 2006.

[78] N. Magome, M. I. Kohira, E. Hayata, S. Mukai, and K. Yoshikawa, "Optical trapping of a growing water droplet in air," *J. Phys. Chem. B*, vol. 107, no. 16, pp. 3988–3990, 2003.

[79] D. R. Burnham and D. McGloin, "Holographic optical trapping of aerosol droplets," *Opt. Express*, vol. 14, no. 9, pp. 4175–4181, 2006.

[80] R. M. Lorenz, J. S. Edgar, G. D. M. Jeffries, Y. Zhao, D. McGloin, and D. T. Chiu, "Vortex-trap-induced fusion of femtoliter-volume aqueous droplets," *Anal. Chem.*, vol. 79, no. 1, pp. 224–228, 2006.

[81] S. Y. Park and P. Y. Chiou, "Light-driven droplet manipulation technologies for lab-on-a-chip applications," *Adv. Optoelectron.*, vol. 2011, pp. 1–12, 2011.

[82] L. E. Scriven and C. V. Sternling, “The marangoni effects,” *Nature*, vol. 187, no. 4733, pp. 186–188, 1960.

[83] D. Psaltis, S. R. Quake, and C. Yang, “Developing optofluidic technology through the fusion of microfluidics and optics,” *Nature*, vol. 442, no. 7101, pp. 381–386, 2006.

[84] A.-Q. Liu, “Preface to special topic: Optofluidics,” *Biomicrofluidics*, vol. 4, no. 4, pp. 042901–2, 2010.

[85] S. B. Amar and B. G. Yogesh, “Virtual microfluidic traps, filters, channels and pumps using marangoni flows,” *J. Micromech. Microeng.*, vol. 18, no. 11, pp. 115031–12, 2008.

[86] M. L. Cordero, D. R. Burnham, C. N. Baroud, and D. McGloin, “Thermocapillary manipulation of droplets using holographic beam shaping: Microfluidic pin ball,” *Appl. Phys. Lett.*, vol. 93, no. 3, pp. 034107–3, 2008.

[87] S.-Y. Park, T.-H. Wu, Y. Chen, M. A. Teitell, and P.-Y. Chiou, “High-speed droplet generation on demand driven by pulse laser-induced cavitation,” *Lab on a Chip*, vol. 11, no. 6, pp. 1010–1012, 2011.

[88] D. K. N. Sinz and A. A. Darhuber, “Self-propelling surfactant droplets in chemically-confined microfluidics - cargo transport, drop-splitting and trajectory control,” *Lab on a Chip*, vol. 12, no. 4, pp. 705–707, 2012.

[89] P. Y. Chiou, H. Moon, H. Toshiyoshi, C.-J. Kim, and M. C. Wu, “Light actuation of liquid by optoelectrowetting,” *Sens. Actuators, A: Physical*, vol. 104, no. 3, pp. 222–228, 2003.

[90] S.-K. Oh, M. Nakagawa, and K. Ichimura, “Photocontrol of liquid motion on an azobenzene monolayer,” *J. Mater. Chem.*, vol. 12, no. 8, pp. 2262–2269, 2002.

[91] D. Baigl, “Photo-actuation of liquids for light-driven microfluidics: state of the art and perspectives,” *Lab on a Chip*, vol. 12, no. 19, pp. 3637–3653, 2012.

[92] H. Moon, S. K. Cho, R. L. Garrell, and C.-J. C. J. Kim, “Low voltage electrowetting-on-dielectric,” *J. Appl. Phys.*, vol. 92, no. 7, pp. 4080–4087, 2002.

[93] B. Berge and J. Peseux, “Variable focal lens controlled by an external voltage: An application of electrowetting,” *Eur. Phys. J. E*, vol. 3, pp. 159–163, 2000.

[94] T. Roques-Carmes, R. A. Hayes, B. J. Feenstra, and L. J. M. Schlangen, "Liquid behavior inside a reflective display pixel based on electrowetting," *J. Appl. Phys.*, vol. 95, no. 8, pp. 4389–4396, 2004.

[95] S. K. Cho, S.-K. Fan, H. Moon, and C.-J. Kim, "Towards digital microfluidic circuits: creating, transporting, cutting and merging liquid droplets by electrowetting-based actuation," in *The Fifteenth IEEE International Conference on Micro Electro Mechanical Systems, 2002.*, pp. 32–35, 2002.

[96] C. Pei-Yu, C. Zehao, and M. C. Wu, "Droplet manipulation with light on optoelectrowetting device," *J. Microelectromech. Syst.*, vol. 17, no. 1, pp. 133–138, 2008.

[97] D. E. Kataoka and S. M. Troian, "Patterning liquid flow on the microscopic scale," *Nature*, vol. 402, no. 6763, pp. 794–797, 1999.

[98] N. O. Young, J. S. Goldstein, and M. J. Block, "The motion of bubbles in a vertical temperature gradient," *J. Fluid Mech.*, vol. 6, no. 3, pp. 350–356, 1959.

[99] N. Garnier, R. O. Grigoriev, and M. F. Schatz, "Optical manipulation of microscale fluid flow," *Phys. Rev. Lett.*, vol. 91, no. 5, pp. 054501–4, 2003.

[100] A. T. Ohta, A. Jamshidi, J. K. Valley, H.-Y. Hsu, and M. C. Wu, "Optically actuated thermocapillary movement of gas bubbles on an absorbing substrate," *Appl. Phys. Lett.*, vol. 91, no. 7, pp. 074103–3, 2007.

[101] R. T. Kelly, *"Advances in Microfluidics"*. InTech. cop., Rijeka, Croatia, 2012.

[102] K. T. Kotz, K. A. Noble, and G. W. Faris, "Optical microfluidics," *Appl. Phys. Lett.*, vol. 85, no. 13, pp. 2658–2660, 2004.

[103] S. S. Dixit, H. Kim, A. Vasilyev, A. Eid, and G. W. Faris, "Light-driven formation and rupture of droplet bilayers," *Langmuir*, vol. 26, no. 9, pp. 6193–6200, 2010.

[104] E. Vela, M. Hafez, and S. Régnier, "Laser-induced thermocapillary convection for mesoscale manipulation," *Int. J. Optomechatronics*, vol. 3, no. 4, pp. 289–302, 2009.

[105] D. Okawa, S. J. Pastine, A. Zettl, and J. M. J. Frechet, "Surface tension mediated conversion of light to work," *J. Am. Chem. Soc.*, vol. 131, no. 15, pp. 5396–5398, 2009.

[106] D. W. Berry, N. R. Heckenberg, and H. Rubinszteindunlop, “Effects associated with bubble formation in optical trapping,” *J. Mod. Opt.*, vol. 47, no. 9, pp. 1575–1585, 2000.

[107] G. K. Kurup and A. S. Basu, “Rolling, aligning, and trapping droplets on a laser beam using marangoni optofluidic tweezers,” in *16th International Conference on Solid-State Sensors, Actuators and Microsystems, 2011*, pp. 266–269, 2011.

[108] L. M. Siewierski, W. J. Brittain, S. Petrash, and M. D. Foster, “Photoresponsive monolayers containing in-chain azobenzene,” *Langmuir*, vol. 12, no. 24, pp. 5838–5844, 1996.

[109] C. L. Feng, Y. J. Zhang, J. Jin, Y. L. Song, L. Y. Xie, G. R. Qu, L. Jiang, and D. B. Zhu, “Reversible wettability of photoresponsive fluorine-containing azobenzene polymer in langmuir blodgett films,” *Langmuir*, vol. 17, no. 15, pp. 4593–4597, 2001.

[110] J. Eastoe and A. Vesperinas, “Self-assembly of light-sensitive surfactants,” *Soft Matter*, vol. 1, no. 5, pp. 338–347, 2005.

[111] X. Liu and N. L. Abbott, “Spatial and temporal control of surfactant systems,” *J. Colloid Interface Sci.*, vol. 339, no. 1, pp. 1 – 18, 2009.

[112] K. G. Yager and C. J. Barrett, “Novel photo-switching using azobenzene functional materials,” *J. Photochem. Photobiol., A*, vol. 182, no. 3, pp. 250–261, 2006.

[113] J. Lahann and R. Langer, “Smart materials with dynamically controllable surfaces,” *MRS Bulletin*, vol. 30, pp. 185–188, 2005.

[114] Y. Liu, L. Mu, B. Liu, and J. Kong, “Controlled switchable surface,” *Chem. Eur. J.*, vol. 11, no. 9, pp. 2622–2631, 2005.

[115] N. Delorme, J.-F. Bardeau, A. Bulou, and F. Poncin-Epaillard, “Azobenzene-containing monolayer with photoswitchable wettability,” *Langmuir*, vol. 21, no. 26, pp. 12278–12282, 2005.

[116] P. Dietrich, F. Michalik, R. Schmidt, C. Gahl, G. Mao, M. Breusing, M. B. Raschke, B. Priewisch, T. Elsässer, R. Mendelsohn, M. Weinelt, and K. Rück-Braun, “An anchoring strategy for photoswitchable biosensor technology: azobenzene-modified sams on si(111),” *Appl. Phys. A*, vol. 93, no. 2, pp. 285–292, 2008.

[117] J. Berna, D. A. Leigh, M. Lubomska, S. M. Mendoza, E. M. Perez, P. Rudolf, G. Teobaldi, and F. Zerbetto, “Macroscopic transport by synthetic molecular machines,” *Nat. Mater.*, vol. 4, no. 9, pp. 704–710, 2005.

[118] R. Rosario, D. Gust, A. A. Garcia, M. Hayes, J. L. Taraci, T. Clement, J. W. Dailey, and S. T. Picraux, “Lotus effect amplifies light-induced contact angle switching,” *J. Phys. Chem. B*, vol. 108, no. 34, pp. 12640–12642, 2004.

[119] B. Tylkowski, S. Peris, M. Giamberini, R. Garcia-Valls, J. A. Reina, and J. C. Ronda, “Light-induced switching of the wettability of novel asymmetrical poly(vinyl alcohol)-co-ethylene membranes blended with azobenzene polymers,” *Langmuir*, vol. 26, no. 18, pp. 14821–14829, 2010.

[120] W. Jiang, G. Wang, Y. He, X. Wang, Y. An, Y. Song, and L. Jiang, “Photo-switched wettability on an electrostatic self-assembly azobenzene monolayer,” *Chem. Commun.*, vol. 0, no. 28, pp. 3550–3552, 2005.

[121] A. Kausar, H. Nagano, T. Ogata, T. Nonaka, and S. Kurihara, “Photocontrolled translational motion of a microscale solid object on azobenzene-doped liquid-crystalline films,” *Angew. Chem. Int. Ed.*, vol. 48, no. 12, pp. 2144–2147, 2009.

[122] T. Yamamoto and M. Yoshida, “Photoinduced directional motions of microparticles at air-liquid-crystal interfaces of azobenzene-doped liquid-crystal films with homeotropic or homogeneous alignment structures,” *Applied Physics Express*, vol. 5, no. 10, pp. 101701–3, 2012.

[123] A. Martinez, H. C. Mireles, and I. I. Smalyukh, “Large-area optoelastic manipulation of colloidal particles in liquid crystals using photoresponsive molecular surface monolayers,” *Proc. Natl. Acad. Sci. U.S.A.*, vol. 108, no. 52, pp. 20891–20896, 2011.

[124] J.-P. Abid, M. Frigoli, R. Pansu, J. Szeftel, J. Zyss, C. Larpent, and S. Brasselet, “Light-driven directed motion of azobenzene-coated polymer nanoparticles in an aqueous medium,” *Langmuir*, vol. 27, no. 13, pp. 7967–7971, 2011.

[125] E. Chevallier, A. Mamane, H. A. Stone, C. Tribet, F. Lequeux, and C. Monteux, “Pumping-out photo-surfactants from an air-water interface using light,” *Soft Matter*, vol. 7, no. 17, pp. 7866–7874, 2011.

[126] N. Malagnino, G. Pesce, A. Sasso, and E. Arimondo, “Measurements of trapping efficiency and stiffness in optical tweezers,” *Opt. Commun.*, vol. 214, no. 1-6, pp. 15–24, 2002.

[127] J. A. Lock, “Calculation of the radiation trapping force for laser tweezers by use of generalized lorenz-mie theory. i. localized model description of an on-axis tightly focused laser beam with spherical aberration,” *Appl. Opt.*, vol. 43, no. 12, pp. 2532–2544, 2004.

[128] A. Alvaro Ranha Neves, A. Fontes, L. Aurelio Padilha, E. Rodriguez, C. Henrique de Brito Cruz, L. Carlos Barbosa, and C. Lenz Cesar, “Exact partial wave expansion of optical beams with respect to an arbitrary origin,” *Opt. Lett.*, vol. 31, no. 16, pp. 2477–2479, 2006.

[129] M. Goksor, K. Ramser, P. Hagberg, and D. Hanstorp, “Optical tweezers applied to a microfluidic system,” *Lab Chip*, vol. 4, no. 3, pp. 196–200, 2004.

[130] E. Eriksson, J. Enger, B. Nordlander, N. Erjavec, K. Ramser, M. Goksör, S. Hohmann, T. Nyström, and D. Hanstorp, “A microfluidic system in combination with optical tweezers for analyzing rapid and reversible cytological alterations in single cells upon environmental changes,” *Lab on a Chip*, vol. 7, no. 1, pp. 71–76, 2007.

[131] B. S. Schmidt, A. H. Yang, D. Erickson, and M. Lipson, “Optofluidic trapping and transport on solid core waveguides within a microfluidic device,” *Opt. Express*, vol. 15, no. 22, pp. 14322–14334, 2007.

[132] K. Xiao and D. G. Grier, “Sorting colloidal particles into multiple channels with optical forces: Prismatic optical fractionation,” *Phys. Rev. E*, vol. 82, no. 5, pp. 051407–9, 2010.

[133] J. A. van Heiningen and R. J. Hill, “Polymer adsorption onto a micro-sphere from optical tweezers electrophoresis,” *Lab on a Chip*, vol. 11, no. 1, pp. 152–162, 2011.

[134] M. E. J. Friese, T. A. Nieminen, N. R. Heckenberg, and H. Rubinsztein-Dunlop, “Optical alignment and spinning of laser-trapped microscopic particles,” *Nature*, vol. 394, no. 6691, pp. 348–350, 1998.

[135] A. Terray, J. Oakey, and D. W. M. Marr, “Microfluidic control using colloidal devices,” *Science*, vol. 296, no. 5574, pp. 1841–1844, 2002.

[136] J. Leach, H. Mushfique, R. di Leonardo, M. Padgett, and J. Cooper, “An optically driven pump for microfluidics,” *Lab on a Chip*, vol. 6, no. 6, pp. 735–739, 2006.

[137] J. Wu, D. Day, and M. Gu, “Shear stress mapping in microfluidic devices by optical tweezers,” *Opt. Express*, vol. 18, no. 8, pp. 7611–7616, 2010.

[138] B. Landenberger, H. Hofemann, S. Wadle, and A. Rohrbach, “Microfluidic sorting of arbitrary cells with dynamic optical tweezers,” *Lab on a Chip*, vol. 12, no. 17, pp. 3177–3183, 2012.

[139] M. M. Wang, E. Tu, D. E. Raymond, J. M. Yang, H. Zhang, N. Hagen, B. Dees, E. M. Mercer, A. H. Forster, I. Kariv, P. J. Marchand, and W. F. Butler, “Microfluidic sorting of mammalian cells by optical force switching,” *Nat. Biotechnol.*, vol. 23, no. 1, pp. 83–87, 2005.

[140] M. Akbari, D. Sinton, and M. Bahrami, “Pressure drop in rectangular microchannels as compared with theory based on arbitrary cross section,” *J. Fluids Eng.*, vol. 131, no. 4, pp. 041202–8, 2009.

[141] M. Akbari, D. Sinton, and M. Bahrami, “Flow in slowly varying microchannels of rectangular cross-section,” *ASME Conference Proceedings*, vol. 2009, no. 43727, pp. 1335–1346, 2009.

[142] L. Holzer, J. Bammert, R. Rzehak, and W. Zimmermann, “Dynamics of a trapped brownian particle in shear flows,” *Phys. Rev. E*, vol. 81, no. 4, pp. 041124–14, 2010.

[143] P. Saffman, “The lift force on a small sphere in a slow shear flow, corrigendum,” *J. Fluid. Mech.*, vol. 22, p. 385, 1965.

[144] T. Lake, A. Carruthers, M. Taylor, L. Paterson, F. Gunn-Moore, J. Allen, W. Sibbett, and K. Dholakia, “Optical trapping and fluorescence excitation with violet diode lasers and extended cavity surface emitting lasers,” *Opt. Express*, vol. 12, no. 4, pp. 670–678, 2004.

[145] W. M. Lee, *“Optical trapping: Optical interferometric meteorology and nanophotonics”*. Phd thesis, University of St. Andrews, UK, 2010.

[146] K. D. Crawford and K. D. Hughes, “Rapid formation and spectroscopic observation of polystyrene conjugation in individual micron-diameter particles with visible radiation,” *J. Phys. Chem. B*, vol. 101, no. 6, pp. 864–870, 1997.

[147] N. B. Viana, M. S. Rocha, O. N. Mesquita, A. Mazolli, P. A. Maia Neto, and H. M. Nussenzveig, “Towards absolute calibration of optical tweezers,” *Phys. Rev. E*, vol. 75, no. 2, p. 021914, 2007.

[148] T. Tlusty, A. Meller, and R. Bar-Ziv, “Optical gradient forces of strongly localized fields,” *Phys. Rev. Lett.*, vol. 81, no. 8, pp. 1738–1741, 1998.

[149] E. Fällman and O. Axner, “Influence of a glass-water interface on the on-axis trapping of micrometer-sized spherical objects by optical tweezers,” *Appl. Opt.*, vol. 42, no. 19, pp. 3915–3926, 2003.

[150] E. Theofanidou, L. Wilson, W. J. Hossack, and J. Arlt, “Spherical aberration correction for optical tweezers,” *Opt. Commun.*, vol. 236, no. 1-3, pp. 145–150, 2004.

[151] V. Bormuth, A. Jannasch, M. Ander, C. M. van Kats, A. van Blaaderen, J. Howard, and E. Schäffer, “Optical trapping of coated microspheres,” *Opt. Express*, vol. 16, no. 18, pp. 13831–13844, 2008.

[152] K. Svoboda and S. M. Block, “Biological applications of optical forces,” *Annu. Rev. Biophys. Biomol. Struct.*, vol. 23, no. 1, pp. 247–285, 1994.

[153] A. LeGall, K. Perronet, D. Dulin, A. Villing, P. Bouyer, K. Visscher, and N. Westbrook, “Simultaneous calibration of optical tweezers spring constant and position detector response,” *Opt. Express*, vol. 18, no. 25, pp. 26469–26474, 2010.

[154] T. Godazgar, R. Shokri, and S. N. S. Reihani, “Potential mapping of optical tweezers,” *Opt. Lett.*, vol. 36, no. 16, pp. 3284–3286, 2011.

[155] Z. Gong, Z. Wang, Y. Li, L. Lou, and S. Xu, “Axial deviation of an optically trapped particle in trapping force calibration using the drag force method,” *Opt. Commun.*, vol. 273, no. 1, pp. 37–42, 2007.

[156] F. Merenda, G. Boer, J. Rohner, G. Delacrétaz, and R.-P. Salathé, “Escape trajectories of single-beam optically trapped micro-particles in a transverse fluid flow,” *Opt. Express*, vol. 14, no. 4, pp. 1685–1699, 2006.

[157] A. C. Richardson, S. N. S. Reihani, and L. B. Oddershede, “Non-harmonic potential of a single beam optical trap,” *Opt. Express*, vol. 16, no. 20, pp. 15709–15717, 2008.

[158] B. Paul and H. Stuart, “Three-dimensional force calibration of a single-beam optical gradient trap,” *J. Phys. Condens. Matter*, vol. 14, no. 33, pp. 7757–7768, 2002.

[159] N. B. Simpson, D. McGloin, K. Dholakia, L. Allen, and M. J. Padgett, “Optical tweezers with increased axial trapping efficiency,” *J. Mod. Opt.*, vol. 45, no. 9, pp. 1943–1949, 1998.

[160] D. Myers, *“Surfactant Science and Technology”*. John Wiley and Sons, Inc., Hoboken, New Jersey, 2006.

[161] P.-G. d. Gennes, F. Brochard-Wyart, and D. Quere, *“Capillarity and Wetting Phenomena”*. Springer, 233 Spring Street, NY 10013, USA, 2004.

[162] D. Myers, *“Surfaces, Interfaces, and Colloids: Principles and Applications”*. VCH publishers, Inc. 220 East 23rd Street, Suite 909, New York 10010, 1990.

[163] V. S. Ajaev, *“Interfacial Fluid Mechanics: A Mathematical Modeling Approach”*. Springer, 233 Spring Street, NY 10013, USA, 2012.

[164] T. Battal, C. D. Bain, M. Weiß, and R. C. Darton, “Surfactant adsorption and marangoni flow in liquid jets: I. experiments,” *J. Colloid Interface Sci.*, vol. 263, no. 1, pp. 250–260, 2003.

[165] D. Schwabe, U. Moller, J. Schneider, and A. Scharmann, “Instabilities of shallow dynamic thermocapillary liquid layers,” *Phys. Fluids A: Fluid Dynamics*, vol. 4, no. 11, pp. 2368–2381, 1992.

[166] X. Fanton and A. M. Cazabat, “Spreading and instabilities induced by a solutal marangoni effect,” *Langmuir*, vol. 14, no. 9, pp. 2554–2561, 1998.

[167] A. Pereira, P. J. Trevelyan, U. Thiele, and S. Kalliadasis, “Interfacial hydrodynamic waves driven by chemical reactions,” *J. Eng. Math.*, vol. 59, no. 2, pp. 207–220, 2007.

[168] A. Oron and P. Rosenau, “Formation of patterns induced by thermocapillarity and gravity,” *J. Phys. II*, vol. 2, no. 2, pp. 131–146, 1991.

[169] P. Neogi, “Tears-of-wine and related phenomena,” *J. Colloid Interface Sci.*, vol. 105, no. 1, pp. 94–101, 1985.

[170] J. Thomson, “Xlii. on certain curious motions observable at the surfaces of wine and other alcoholic liquors,” *Philosophical Magazine Series 4*, vol. 10, no. 67, pp. 330–333, 1855.

[171] N. M. Arifin, F. M. Ali, R. Nazar, and I. Pop, “Thermal and solutal marangoni mixed convection boundary layer flow,” *WSEAS Trans. Math.*, vol. 9, no. 5, pp. 376–385, 2010.

[172] B. Cicciarelli, *“Dynamics in a Photoresponsive Surfactant System”*. Phd thesis, Massachusetts Institute of Technology, US, 2007.

[173] K. Arafune, K. Yamamoto, and A. Hirata, “Interactive thermal and solutal marangoni convection during compound semiconductor growth in a rectangular open boat,” *Int. J. Heat Mass Transfer*, vol. 44, no. 13, pp. 2405–2411, 2001.

[174] M. J. Rosen, *“Surfactants and Interfacial phenomena”*. John Wiley and Sons, Inc., Hoboken, New Jersey, 2004.

[175] L. L. Schramm, E. N. Stasiuk, and D. G. Marangoni, “Surfactants and their applications,” *Annual Reports Section "C" (Physical Chemistry)*, vol. 99, pp. 3–48, 2003.

[176] J. Eastoe and J. S. Dalton, “Dynamic surface tension and adsorption mechanisms of surfactants at the air-water interface,” *Adv. Colloid Interface Sci.*, vol. 85, no. 2-3, pp. 103–144, 2000.

[177] B. A. Cicciarelli, T. A. Hatton, and K. A. Smith, “Dynamic surface tension behavior in a photoresponsive surfactant system,” *Langmuir*, vol. 23, no. 9, pp. 4753–4764, 2007.

[178] X. Cui, S. Mao, M. Liu, H. Yuan, and Y. Du, “Mechanism of surfactant micelle formation,” *Langmuir*, vol. 24, no. 19, pp. 10771–10775, 2008.

[179] P. Dimitrakopoulos, “Interfacial dynamics in stokes flow via a three-dimensional fully-implicit interfacial spectral boundary element algorithm,” *J. Comput. Phys.*, vol. 225, no. 1, pp. 408–426, 2007.

[180] C. Brieke, F. Rohrbach, A. Gottschalk, G. Mayer, and A. Heckel, “Light-controlled tools,” *Angew. Chem. Int. Ed.*, vol. 51, no. 34, pp. 8446–8476, 2012.

[181] T. Shang, K. A. Smith, and T. A. Hatton, “Photoresponsive surfactants exhibiting unusually large, reversible surface tension changes under varying illumination conditions,” *Langmuir*, vol. 19, no. 26, pp. 10764–10773, 2003.

[182] H. Sakai, H. Ebana, K. Sakai, K. Tsuchiya, T. Ohkubo, and M. Abe, “Photo-isomerization of spiropyran-modified cationic surfactants,” *J. Colloid Interface Sci.*, vol. 316, no. 2, pp. 1027–1030, 2007.

[183] L. Brzozowski and E. H. Sargent, “Azobenzenes for photonic network applications: Third-order nonlinear optical properties,” *J. Mater. Sci. - Mater. Electron.*, vol. 12, no. 9, pp. 483–489, 2001.

[184] T. Naito, K. Horie, and I. Mita, “Photochemistry in polymer solids. 11. the effects of the size of reaction groups and the mode of photoisomerization on photochromic reactions in polycarbonate film,” *Macromolecules*, vol. 24, no. 10, pp. 2907–2911, 1991.

[185] I. Mita, K. Horie, and K. Hirao, “Photochemistry in polymer solids. 9. photoisomerization of azobenzene in a polycarbonate film,” *Macromolecules*, vol. 22, no. 2, pp. 558–563, 1989.

[186] R. T. Buwalda, J. M. Jonker, and J. B. F. N. Engberts, “Aggregation of azo dyes with cationic amphiphiles at low concentrations in aqueous solution,” *Langmuir*, vol. 15, no. 4, pp. 1083–1089, 1999.

[187] H.-C. Kang, B. M. Lee, J. Yoon, and M. Yoon, “Synthesis and surface-active properties of new photosensitive surfactants containing the azobenzene group,” *J. Colloid Interface Sci.*, vol. 231, no. 2, pp. 255–264, 2000.

[188] M. Bonini, D. Berti, J. M. Di Meglio, M. Almgren, J. Teixeira, and P. Baglioni, “Surfactant aggregates hosting a photoresponsive amphiphile: structure and photoinduced conformational changes,” *Soft Matter*, vol. 1, no. 6, pp. 444–454, 2005.

[189] B. Kumar and K. A. Suresh, “Kinetics of trans-cis isomerization in azobenzene dimers at an air-water interface,” *Phys. Rev. E*, vol. 80, no. 2, pp. 021601–5, 2009.

[190] K. Wang, E. Schonbrun, P. Steinvurzel, and K. B. Crozier, “Trapping and rotating nanoparticles using a plasmonic nano-tweezer with an integrated heat sink,” *Nat. Commun.*, vol. 2, p. 469, 2011.

[191] M. D. Carl and S. T. Wereley, “The theory of diffraction-limited resolution in microparticle image velocimetry,” *Meas. Sci. Technol.*, vol. 14, no. 7, p. 1047, 2003.

[192] C. P. Wang, “Laser doppler velocimetry,” *J. Quant. Spectrosc. Radiat. Transfer*, vol. 40, no. 3, pp. 309–319, 1988.

[193] D. Sinton, “Microscale flow visualization,” *Microfluid. Nanofluid.*, vol. 1, no. 1, pp. 2–21, 2004.

[194] P. E. Dimotakis, F. D. Debussy, and M. M. Koochesfahani, “Particle streak velocity field measurements in a two-dimensional mixing layer,” *Phys. Fluids*, vol. 24, no. 6, pp. 995–999, 1981.

[195] R. J. Adrian and J. Westerweel, *“Particle Image Velocimetry”*. Cambridge University Press, NY, USA, 2011.

[196] W. Merzkirch, *“Flow Visualization”*. Academic Press, NC. (London) LTD, 1974.

[197] R. J. Adrian, “Twenty years of particle image velocimetry,” *Exp. Fluids*, vol. 39, no. 2, pp. 159–169, 2005.

[198] E. Hatta, “Sequential collapse transitions in a langmuir monolayer,” *Langmuir*, vol. 20, no. 10, pp. 4059–4063, 2004.

[199] S. Baoukina, L. Monticelli, H. J. Risselada, S. J. Marrink, and D. P. Tieleman, “The molecular mechanism of lipid monolayer collapse,” *Proc. Natl. Acad. Sci. U.S.A.*, vol. 105, no. 31, pp. 10803–10808, 2008.

[200] L. E. Scriven, “Dynamics of a fluid interface equation of motion for newtonian surface fluids,” *Chem. Eng. Sci.*, vol. 12, no. 2, pp. 98–108, 1960.

[201] L. Gao and T. J. McCarthy, “Contact angle hysteresis explained,” *Langmuir*, vol. 22, no. 14, pp. 6234–6237, 2006.

[202] H. Kawaguchi and K. Fujimoto, “Smart latexes for bioseparation,” *Bioseparation*, vol. 7, no. 4, pp. 253–258, 1998.

[203] M. A. C. Stuart, W. T. S. Huck, J. Genzer, M. Muller, C. Ober, M. Stamm, G. B. Sukhorukov, I. Szleifer, V. V. Tsukruk, M. Urban, F. Winnik, S. Zauscher, I. Luzinov, and S. Minko, “Emerging applications of stimuli-responsive polymer materials,” *Nat. Mater.*, vol. 9, no. 2, pp. 101–113, 2010.

[204] B. Ziólkowski, M. Czugala, and D. Diamond, "Integrating stimulus responsive materials and microfluidics: The key to next-generation chemical sensors," *J. Intell. Mater. Syst. Struct.*, vol. 0, no. 0, pp. 1–18, 2012.

[205] B. Jeong, Y. H. Bae, D. S. Lee, and S. W. Kim, "Biodegradable block copolymers as injectable drug-delivery systems," *Nature*, vol. 388, no. 6645, pp. 860–862, 1997.

[206] D. Schmaljohann, "Thermo- and ph-responsive polymers in drug delivery," *Adv. Drug Delivery Rev.*, vol. 58, no. 15, pp. 1655–1670, 2006.

[207] M. Heskins and J. E. Guillet, "Solution properties of poly(n-isopropylacrylamide)," *J. Macromol. Sci. Part A Pure Appl. Chem.*, vol. 2, no. 8, pp. 1441–1455, 1968.

[208] S. Schmidt, M. Zeiser, T. Hellweg, C. Duschl, A. Fery, and H. Möhwald, "Adhesion and mechanical properties of pnipam microgel films and their potential use as switchable cell culture substrates," *Adv. Funct. Mater.*, vol. 20, no. 19, pp. 3235–3243, 2010.

[209] T. Sun, G. Wang, L. Feng, B. Liu, Y. Ma, L. Jiang, and D. Zhu, "Reversible switching between superhydrophilicity and superhydrophobicity," *Angew. Chem. Int. Ed.*, vol. 43, no. 3, pp. 357–360, 2004.

[210] N. Verplanck, Y. Coffinier, V. Thomy, and R. Boukherroub, "Wettability switching techniques on superhydrophobic surfaces," *Nanoscale Res. Lett.*, vol. 2, no. 12, pp. 577–596, 2007.

[211] H. Tu, C. E. Heitzman, and P. V. Braun, "Patterned poly(n-isopropylacrylamide) brushes on silica surfaces by microcontact printing followed by surface-initiated polymerization," *Langmuir*, vol. 20, no. 19, pp. 8313–8320, 2004.

[212] R. Pelton, "Poly(n-isopropylacrylamide) (pnipam) is never hydrophobic," *J. Colloid Interface Sci.*, vol. 348, no. 2, pp. 673–674, 2010.

[213] F. J. Schmitt, C. Park, J. Simon, H. Ringsdorf, and J. Israelachvili, "Direct surface force and contact angle measurements of an adsorbed polymer with a lower critical solution temperature," *Langmuir*, vol. 14, no. 10, pp. 2838–2845, 1998.

[214] G. Liu and G. Zhang, "Collapse and swelling of thermally sensitive poly(n-isopropylacrylamide) brushes monitored with a quartz crystal microbalance," *J. Phys. Chem. B*, vol. 109, no. 2, pp. 743–747, 2004.

[215] J. K. Simons, J. M. Chen, J. W. Taylor, and R. A. Rosenberg, “Fluorescence studies of the vacuum ultraviolet, synchrotron radiation-induced photochemistry of polystyrene,” *Macromolecules*, vol. 26, no. 13, pp. 3262–3266, 1993.

[216] C. Y. Soong, W. K. Li, C. H. Liu, and P. Y. Tzeng, “Theoretical analysis for photophoresis of a microscale hydrophobic particle in liquids,” *Opt. Express*, vol. 18, no. 3, pp. 2168–2182, 2010.

[217] N. Grassie and N. A. Weir, “The photooxidation of polymers. ii. photolysis of polystyrene,” *J. Appl. Polym. Sci.*, vol. 9, no. 3, pp. 975–986, 1965.

[218] K. M. Dyumayev, N. P. Kuzmina, V. V. Lobko, G. A. Matyushin, V. S. Nechitailo, and A. V. Chadov, “The mechanisms of polystyrene destruction under influence of powerful uv-radiation: Initial stages,” *Int. J. Polym. Mater.*, vol. 17, no. 3-4, pp. 121–130, 1992.

[219] J. W. Martin, J. W. Chin, and T. Nguyen, “Reciprocity law experiments in polymeric photodegradation: a critical review,” *Prog. Org. Coat.*, vol. 47, no. 3-4, pp. 292–311, 2003.

Resume

Personal

Name	SUBRAMANYAN NAMBOODIRI VARANAKKOTTU
Date of birth	26.06.1983
Place of birth	Mandur, India
Family status	Married
Nationality	Indian

Academic

Since 9.2009	Ph.D. student at Nano and Microfluidics, Center of smart Interfaces, TU Darmstadt. Research area: Optofluidics
10.2008 - 8.2009	Research student at Department of Physics, Cochin University of Science and Technology, India. Research area: Fabrication of holographic optical elements
9.2006 - 6.2008	M.Phil. Physics, Department of Physics, Cochin University of Science and Technology, India. Thesis: Studies on holographic multiplexing, fabrication of HOEs and hologram recording using photopolymer
7.2004 - 5.2006	MSc Physics, Sir Syed College affiliated to Kannur University, India. Specialization: Microprocessors, Electronic instrumentation
7.2001 - 4.2004	BSc Physics, Sir Syed College affiliated to Kannur University, India.
8.1999 - 3.2001	Higher secondary education, G.H.S.S. Kunhimangalam, India .
1999	10^{th} level (SSLC), G.H.S.S. Kunhimangalam, India .

Awards

Rank holder in BSc examination from Kannur University, India in 2004.

Publications

Publications related to the Ph.D. thesis

Journal papers

[1] Subramanyan Namboodiri Varanakkottu, Sajan Daniel George, Tobias Baier, Steffen Hardt, Martina Ewald and Markus Biesalski, *"Particle Manipulation based on Optically Controlled Free Surface Hydrodynamics"* , Angew Chem Intl Ed (2013). DOI: 10.1002/anie.201302111. (Selected under hot topics by Wiley VCH publishers).

[2] Subramanyan Namboodiri Varanakkottu, Sajan Daniel George and Steffen Hardt, *"Optical trapping in a microfluidic channel"* , (submitted, May 2013).

[3] Subramanyan Namboodiri Varanakkottu, Sajan Daniel George, Tobias Baier, Steffen Hardt, Martina Ewald and Markus Biesalski, *"Manipulation of biological cells using light induced Marangoni flow"* , (submitted, April 2013).

In Conferences

[1] Steffen Hardt, Subramanyan Namboodiri Varanakkottu, Sajan George, Tobias Baier, Martina Ewald and Markus Biesalski, *"Optically controlled Marangoni Tweezers"*, Bulletin of the American Physical Society 65th Annual Meeting of the APS Division of Fluid Dynamics, vol. 57, no. 17, November 18 - 20, 2012; San Diego, California.

[2] Subramanyan Namboodiri Varanakkottu, Sajan Daniel George, Tobias Baier, Steffen Hardt, and Markus Biesalski, *"Marangoni trap at a smart liquid surface"*, 19th International Symposium on Surfactants in Solution (SIS 2012), June 24 - 28, 2012; University of Alberta, Edmonton, Canada.

[3] Subramanyan Namboodiri V, Sajan D George, Steffen Hardt, *"Photodegradation of optically trapped polystyrene beads at 442 nm"*, In: Proc., ICMN 2012: International Conference on Microelectronics and Nanotechnology, September 28 - 30, 2010; Amsterdam.

[4] Sajan D George, Subramanyan Namboodiri V, Steffen Hardt, *"Laser induced photoswitching of azobenzene incorporated in PDMS films"*. In: SPIE Proc., Linear and Nonlinear Optics of Organic Materials X, August 01 - 05, 2010; San Diego.

Publications before joining at TU Darmstadt

In Journals

[1] Pramitha V, Nimmi K P, Subramanyan N V, Rani Joseph, Sreekumar K, and Sudha Kartha C, *"Silver-doped photopolymer media for holographic recording"* , Appl. Opt. 48(12), pp 2255-2261, 2009.

In Conferences

[1] Subramanyan N V, Rajesh C S, Pramitha V, SreeRoop S S, Rani Joseph, Sreekumar K and Sudha Kartha C, *"Holographic Lens Recorded in Eosin Sensitized Acrylamide Based Photopolymer"*, In Proc., International Conference on Trends in Optics and Photonics (ICONTOP 2009), March 1 - 4, 2009; University of Calcutta, Calcutta, India.

[2] Pramitha V, Subramanyan N V, Rani Joseph, K Sreekumar, C Sudha Kartha, *"Holographic multiplexing in a silver doped Acrylamide Photopolymer"*, ICOICT 2009, Feb 26-27, 2009; Trivandrum, India.

[3] Pramitha V, Nimmi K P, Subramanyan N V, Rani Joseph, Sreekumar K, Sudha Kartha C, *"Peristrophic Multiplexing In A Methylene Blue Doped Acrylamide Polymer"*, In Proc., PHOTONICS 2008, Dec 15-17, 2008; IIT Delhi, New Delhi.